Tobacco Mosaic Virus (TMV) as a nanoscaffold for inorganic assemblies

Thesis

Submitted in Fulfillment of the Requirements for the Degree of

Doctor of Philosophy

To

University of Basque Country (Euskal Herriko Unibertsitatea)

By

ABID ALI KHAN

2012

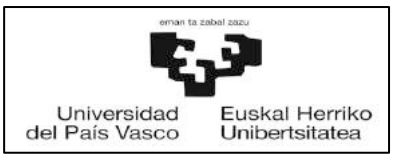

Thesis Director
Dr. Alexander Michael Bittner (Ikerbasque Research Professor)
Group Leader (Self Assembly)
CIC nanoGUNE

Thesis Co-Tutor
Prof. Dr. Felix Maria Urcelay Goñi
Head of Biophysics Unit
Universidad del País Vasco/Euskal Herriko Unibertsitatea

Dedicated to my son

ACKNOWLEDGEMENTS

It would have not been possible to complete this doctoral thesis without the continuous help, support and guidance of the kind people around me. It is a pity that not all of them could be mentioned here.

Above all, I am highly grateful to my thesis director, Alexander Bittner. I would have never made it this far without his continuous help, support and patience. He with his fruitful advices and unsurpassed knowledge was always there for me whenever I was caught in deep waters. I must say that this thesis without my co-tutor, Felix Goñi would have been an uphill task. His kind support, advice and expertise were really essential for the successful completion of the task.

I am especially thankful to Dr. Christina Wege and her Plant Biology group at Stuttgart University (Germany) for the plentiful supply of Tobacco Mosaic Virus (TMV) so that our research work never stopped and kept on going. Not to mention their continuous technical and academic support regarding TMV whenever we needed. I am also highly thankful to Dr. Dermot Brougham (Group Leader) and Eoin Fox of City University, Dublin (Ireland) for providing us iron oxide nanoparticles for coupling to TMV. This thesis has a deep relationship with electron microscopy.. Electron microscopy has been the technique most extensively used in this (work) thesis. Therefore, I am really indebted to the electron microscopy group here at nanoGUNE, i.e. Andrey Chuvulin (Group Leader), Elizaveta Nikulina (Postdoc) and Christopher Tollan (Postdoc/Technician). They have always helped me a lot with imaging and technical issues in electron microscopy. I would like to mention and thank yet another microscopy expert, Marco Möller (CIC biomaGUNE) who from time to time did TEM imaging for my samples.

A Ph.D student is always dependent on postdocs at his/her labs. I was really lucky to have worked with really skilled, learned and helpful postdocs. I am really thankful to Sachin Shah (postdoc), Marcin Gorzny (postdoc) and José Maria Alonso (postdoc) for their friendship, help and support. Amaia Rebollo the technician of our group was always an important person during my Ph.D work. She was always kind to help me in purchasing consumables. I am also grateful to her for the help and support outside work where she always translated Spanish (to English) for me and even at times talked on phones for me to people whom I did not understand or whom did not understand me.

In the end I would like to thank all my colleague Ph.D students either from my group (Self Assembly) or other groups at nanoGUNE. I have passed the best time of my life with my friends and co-workers during my Ph.D studies here. I am really grateful to Thales Oliveira, Wiwat Nuansing, Sven Degenhard, Simon Poly, Johannes Stiegler, Txema Porro and a number of others.

Last but not the least I would say special thanks to my family who agreed to see me once a year but always stood by me to achieve my goals. I am really thankful to my wife and my son to sacrifice to stay away from me for a cause they deemed as very important.

Table of Contents

RESUMEN

Las plantillas artificiales pueden ser sintetizadas por un buen número de técnicas tales como litografía (UV o de haz de electrones), formación de micelas, deposición de haz de iones, síntesis química en disolución, etc. Sin embargo las nanoestructuras artificiales no poseen al 100% la misma distribución de tamaños y formas, y a menudo presentan defectos. En nanofabricación las bioplantillas son preferidas a los materiales compuestos artificiales, ya que las moléculas biológicas mantienen de manera perfecta su tamaño, forma y composición química. Esto nos llevó a buscar bioplantillas que pudieran ser usadas para nanofabricación en nanotecnología. El virus del mosaico del tabaco (VMT) es un virus ARN de forma cilíndrica que provoca enfermedades en el tabaco y en otras plantas. Posee una longitud de 300 nm y un diámetro de 18 nm. Se trata de un tubo de proteínas muy estable que posee un canal interno de 4 nm de diámetro. El VMT se alinea a menudo en oligómeros de 600 nm, 900 nm ó 1200 nm de longitud. Su superficie externa es altamente polar y contiene grupos OH y COOH, estos últimos mayoritariamente deprotonados. Una partícula única de VMT contiene 2130 proteínas de cubierta idénticas. Las subunidades de proteína de cubierta se autoensamblan en una estructura helicoidal de tubo, de tal forma que el ARN se encuentra alojado en su interior. El VMT es estable en un amplio rango de valores de pH (<3 a >8.5) y de temperaturas (>80ºC). Todas estas propiedades físicas del VMT hacen de él un fantástico andamio biológico/proteico en un gran número de estrategias y técnicas de nanoescala. Nosotros usamos el VMT como nanoandamio (bioplantilla) para la deposición de materiales inorgánicos como metales (Ni y Au) y óxidos metálicos (óxido de hierro) en el exterior del tubo de proteína y complejos metálicos (cisplatino y oxaliplatino) dentro del canal de 4 nm.

En primer lugar demostramos que el VMT puede ser empleado para la deposición metálica. El níquel metal ha sido depositado en el exterior del tubo de proteína del VMT. A temperatura ambiente el Ni se comporta como un ferroimán. El objetivo había sido la metalización de los tubos de VMT al completo o sólo en los extremos. Los tubos de VMT metalizados con Ni serían capaces de inducir hipertermia y podrían ser también usados como ferrofluidos. El VMT ha sido metalizado en suspensiones acuosas formando depósitos únicos en forma de mancuernas, de varillas

o de tubos, con diámetros de hasta 3 nm y longitudes de varios micrómetros. El proceso de recubrimiento está basado en la adsorción de cationes de metales nobles seguido de una deposición autocatalítica no electrolítica (ELD). El proceso ELD de Ni en el VMT progresa a través del crecimiento de relativamente pocos núcleos aislados localizados en clusters de Pd. Añadiendo el surfactante aniónico Re610/E se produce la deposición de puntos de Ni, sólo en los extremos del VMT. De manera similar el uso de un surfactante no iónico, Igepal, resulta en el crecimiento de de partículas de Ni densamente espaciadas sobre el VMT. Las medidas de magnetometría realizadas en estas muestras de VMT (metalizadas con Ni) encuentran una magnetización de saturación de aproximadamente 0.004 emu por gramo de depósito sólido (que contiene Ni VMT, pero también sales procedentes del baño). Este valor tan pequeño puede explicarse por la formación de una microestructura cluster consistente en núcleos de Ni bastante pequeños y rodeados por un capazón de NiO, que podría ser indicativo de una oxidación extensiva. Sin embargo, la medida de coercividad de 90 Oe es similar a la del Ni masivo (100 Oe), sugiriendo que los núcleos son suficientemente grandes como para mostrar ferromagnetismo masivo.

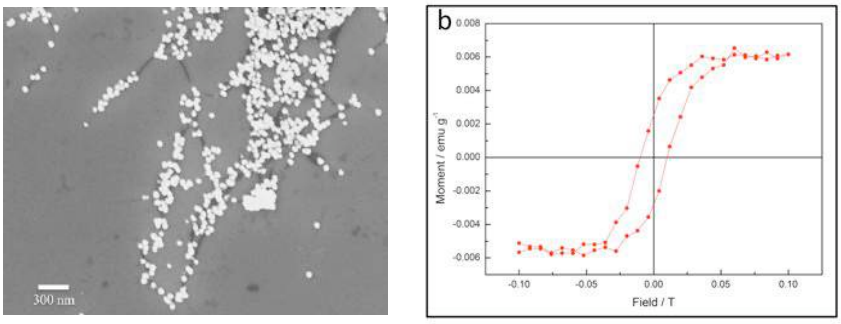

Figura 1. (a) Imagen de SEM de una red de VMT (varillas negras) metalizadas con Ni (esferas blancas) y (b) Magnetización como función del campo aplicado de VMTs metalizados con Ni.

En segundo lugar, empleamos el VMT como bioplantillas para la síntesis de nanotubos de óxido de hierro. Mientras que las síntesis de nanopartículas y nanovarillas de óxidos de hierro se encuentran bien establecidas, los nanotubos son por ahora objetos raros pero con interesantes propiedades magnéticas específicas. Los nanotubos podrían reemplazar a las usuales nanopartículas esféricas en aplicaciones médicas, especialmente imagen por resonancia magnética e hipertermia terapéutica. Los óxidos de hierro son aquí de gran importancia debido a su combinación única de inocuidad (no toxicidad) y magnetismo (ferro-, ferri-, superparamagnetismo). La

síntesis del óxido de hierro sobre VMT supone una química sencilla en disolución y con condiciones suaves. La mezcla de Fe^{2+} acuoso y sales de Fe^{3+} fue empleada para formar óxido de hierro en la superficie externa del VMT cubierta de grupos carboxilato. La visualización por microscopía electrónica de barrido muestra virus de plantas cubiertos por una capa fina de óxido de hierro (5-7nm). La microscopía de transmisión electrónica muestra que la síntesis no destruye el virus, e incluso con el recubrimiento de óxido de hierro se pudo ver intacto. El análisis local de EDX demostró la presencia de hierro en la superficie externa de la proteína, que tiene que estar en la forma de óxido de hierro. Sin embargo, el análisis de difracción de rayos X (XRD) no mostró señales que pudieran corresponder a algún tipo de óxido de hierro.

Por lo tanto se concluyó que el recubrimiento de óxido de hierro en la superficie externa del VMT es predominantemente amorfo. Las partículas mineralizadas de virus de plantas fueron también examinadas en un SQUID-VSM a 300 K debido a sus propiedades magnéticas. El momento magnético del VMT mineralizado posee una saturación de magnetización de 0.00082 emu/g compatible con un óxido de hierro no cristalino. A pesar de ello, el elevado valor de coercitividad de 0.04 T es inusual. Esto es debido a la naturaleza ferrimagnética del óxido y de la estructura tubular de nuestros nanotubos de óxido de hierro. Las estructuras amorfas a menudo se transforman en fases cristalinas tras un tratamiento térmico. Nuestras muestras no mostraron cambios de tamaño o forma tras el calentamiento, per el tratamiento térmico en aire (a 520 K) y en vacío (a 570 K) produjeron la(s) fase(s) cristalina(s) esperada(s) de γ-Fe_2O_3 y Fe_3O_4, independientemente de que fueran analizadas después del calentamiento en aire o en vacío. A parte de estos cambios a escala atómica, observamos un enorme incremento en el momento magnético. La magnetización de saturación se incrementó a >1 emu/g, mientras que la coercividad se redujo a ≈0.001 T. Los valores se ajustan ahora con precisión a típicos γ-Fe_2O_3 y Fe_3O_4 cristalinos y de nanoescala. Nuestros tubos recocidos de VMT mineralizados pudieron ser usados en ferrofluidos, donde su forma induciría mucho mayor viscosidad que las partículas normales.

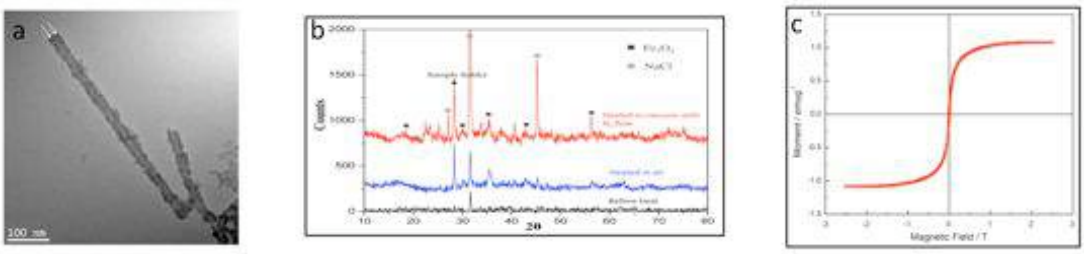

Figura 2: (a) Imagen de TEM de un tubo de VMT mineralizado (con óxido de hierro), (b) Patrones de XRD de VMT mineralizado; tras ser sintetizado (patrón negro), recocido en aire (patrón azul) y recocido en vacío (patron rojo), (c) Magnetización como function del campo aplicado de tubos de VMT mineralizados y recocidos.

En tercer lugar, presentamos la unión de elevado rendimiento de nanopartículas de Au cubiertas con citrato (6 nm) a los residuos de la proteínas externas del VMT de tipo salvaje (natural) a través de un método simple en condiciones ambiente. Las nanopartículas de Au poseen propiedades químicas, ópticas, eléctricas y catalíticas únicas y por lo tanto han sido estudiadas más extensivamente. Se emplean para un gran número de aplicaciones tales como immunoensayos de biosensores, visualización óptica y fototermolisis de células cancerosas. Las nanopartículas de Au se encuentran normalmente cubiertas con agentes como el citrato para estabilizar la superficie. El recubrimiento con citrato puede ser ocupado por un número de grupos químicos que dejan la superficie de Au disponible para la funcionalización con DNA, péptidos, anticuerpos, etc. La unión de Au a varillas de VMT ya ha sido investigada por otros grupos con VMT mutados, conteniendo cisteína, o a través de complejos protocolos de síntesis. Nosotros desarrollamos un método de preparación nuevo, simple y fácil que no requiere mutantes de VMT. Un hecho interesante de esta síntesis es que produce la decoración satisfactoria de VMT con nanopartículas de Au, sólo a valores de pH bajos, i.e. 2.9-3.4, cerca del punto isoeléctrico del VMT de 2.8. Las partículas de VMT fueron incubadas con nanopartículas de Au cubiertas con citrato en una solución acuosa de ácido cítrico. La síntesis condujo a la decoración de VMT a lo largo de toda su longitud con nanopartículas de Au. Las medidas de potencial Z muestran que en el régimen de pH de la decoración de VMT, las varillas virales están cargadas positivamente, mientras que las nanopartículas de Au cubiertas con citrato están cargadas negativamente. Así pues decoramos las varillas de VMT con nanopartículas de Au negativamente cargadas, explotando la protonación de los residuos aminoácido acídicos en el TMV, obteniendo un exterior positivamente cargado. Esta aproximación para la decoración de VMT con nanopartículas recubiertas con citrato no está limitado a las nanopartículas de Au; la misma estrategia

produjo partículas de VMT decoradas con óxido de hierro (magnético) cuando se emplearon nanopartículas de óxido de hierro cubiertas con citrato en lugar de nanopartículas de Au.

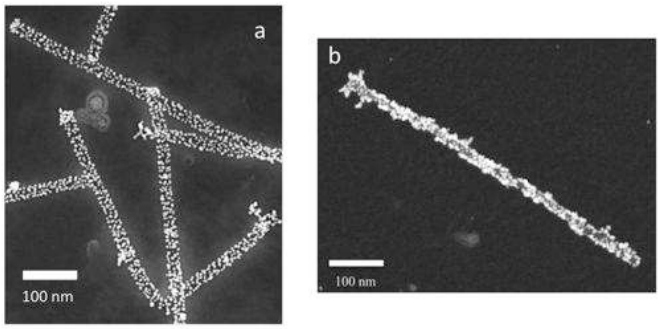

Figura 3. Imagen de STEM de (a) VMT (varillas negras)decorados por nanopartículas de Au recubiertas con citrate (esferas blancas) y (b) nanopartículas de óxido de hierro.

Finalmente encapsulamos fármacos anticancerosos que contenían Pt(II) (cisplatino y oxaliplatino) dentro del canal de 4 nm del VMT. Estos fármacos citotóxicos son dirigidos hoy en día de manera intravenosa. A pesar de que son muy efectivos matando células cancerosas, la toxicidad derivada de su aplicación a células tumorales localmente, significa que células normales/sanas también son destruidas junto con células cancerosas. Actualmente se están dirigiendo muchos esfuerzos al desarrollo de sistemas contenedores pequeños. Están generalmente basados en partículas esféricas huecas, que protegerían a las células sanas. Un buen número de portadores están siendo investigados para dirigir selectivamente estos fármacos a células cancerosas. En estos días, se está poniendo un gran esfuerzo en el desarrollo de sistemas de transporte de fármacos en la nanoescala como liposomas, zeolitas, nanotubos de carbono, polímeros, vesículas celulares y viruses. Combinamos VMT con fármacos anticancerosos aprobados basados en Pt(II). La imbibición de VMT ya había sido estudiada tanto para el análisis clásico de virus (tinción), como para la síntesis de materiales, especialmente hilos metálicos de 3-4 nm de anchura, pero en el caso de disoluciones de fármacos. Hasta ahora se había mostrado que la deposición o el confinamiento de materiales/disoluciones en los canales es posible, pero nosotros también comprobamos la completa eliminación del fármaco tras su eliminación. Hemos optimizado la imbibición y la efusión de fármacos de Pt(II) usando el VMT como nanoandamio para el confinamiento de fármacos. Averiguamos que resulta crucial controlar el pH (aproximadamente 7) y el tiempo (ca. un día) para obtener canales perfectamente llenados, y para permitir vaciarlos (varias horas, liberación

lenta). Nuestro análisis se basó en microscopía electrónica (TEM y STEM), ya que requerimos una resolución espacial muy alta para el canal de 4 nm de anchura. Las partículas de VMT con canales llenos fueron se identificaron y confirmaron por su brillo (en el caso del STEM de campo oscuro) o contraste oscuro (en el caso del TEM de campo claro). También nos esforzamos en cerrar los canales en sus extremos para que los fármacos encapsulados permanezcan en el interior de los canales de VMT. Se estudió el uso de las nanopartículas de Au recubiertas con citrato para bloquear los canales de VMT en ambos extremos después de su llenado con fármacos que contienen Pt(II). Además también investigamos el recubrimiento del VMT con polietilenglicol para producir un nanoandamio no inmunogénico y biocompatible para la distribución de fármacos.

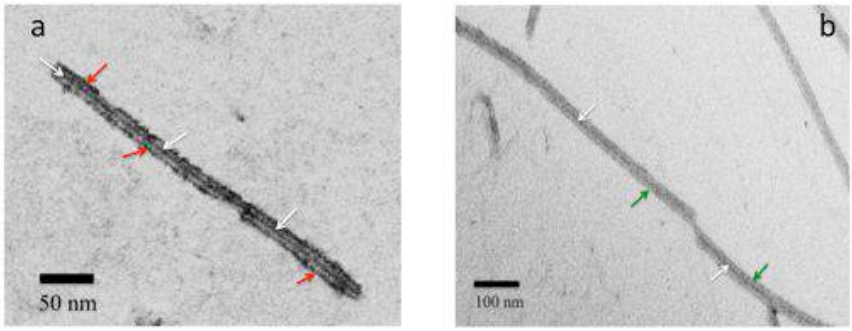

Figura 4. Imagen de STEM invertida de (a) VMT (varillas grises) con cisplatino llenando el canal (línea negra-flechas blancas). El cisplatino también se une al exterior de VMT (fleches rojas). (b) Eliminación del fármaco del exterior del tubo de proteína de VMT (varillas grises), mientras que el canal todavía mantiene el fármaco en su interior (línea negra-flechas blancas). Las líneas verdes indican que el fármaco no está unido al exterior del tubo de proteina del VMT.

Chapter 1

MOTIVATION

We exploit a biological template, a plant virus, *Tobacco Mosaic Virus* (TMV). TMV is a rod-shaped RNA containing virus that causes diseases in tobacco and other plants. It has a length of 300 nm and a diameter of 18 nm. TMV is a highly stable protein tube and has an inner channel of 4 nm in diameter. A single TMV particle contains 2130 identical coat proteins. The protein coat subunits self-assemble into a helical tubular structure in such a way that the RNA is embedded inside it. TMV is stable in a wide range of pH values (<3 - >8.5) and temperatures (up to as high as 85 °C) for several hours [1]. All these properties of TMV make it a fantastic biological/protein scaffold in a large number of nanoscale techniques and strategies.

These properties of TMV motivated us to design a drug delivery strategy to use it as a nanocontainer for drug delivery to treat ovarian carcinomas. The goal was to entrap Pt(II)-containing drugs inside the channel of TMV and subsequently capping the ends by magnetic nanoparticles. This would be tailored to locally inject them at the tumor site. The attachment of monoclonal antibodies (Fab) would specifically direct it to be taken by cancer cells only. Application of an external alternating magnetic field would release the drug and also induce local heating (hyperthermia) due to the presence of magnetic nanoparticles. The most important reasons that made the basis of our motivation are:

a. TMV is non-pathogenic to all humans, i.e. it is not known to cause any diseases in humans. It is though highly immunogenic and the protein tube does provide a number of antigenic determinants to be recognized and neutralized by the highly efficient immune system of the human body [2].

b. TMV protein tube offers a number of functional groups (COOH, OH and NH_2) that can be exploited for covalent linking of organic as well as inorganic molecules [3]. Since it is a protein structure, some new functionalities can also be introduced by genetic engineering. This had already been achieved for instance, exposing Lys (NH_2 groups) [4] and Cys (SH groups) [5] on the

surface to achieve linking of metallic and non-metallic particles to TMV for various purposes.

c. TMV has a 4 nm (in diameter) channel in its 18 nm tube. This channel is indeed accessible for ions to move in (and out). This is how we got motivated to design a drug delivery strategy using the TMV channel for drug encapsulation. Knez *et. al.* have already reported the synthesis of Ni and Co nanowires inside the channel of TMV [6, 7] where the channel was accessed by metal ions and by a reductant to synthesize 3 nm wide metal nanowires (figures 1.1a and 1.1b). Other groups also synthesized CoPt nanowires in TMV channel (figure 1.2) [8]. Based on these findings, we hoped that Pt(II)-containing anticancer drugs could be locally encapsulated in the TMV channel, but without reduction of the Pt(II).

d. TMV can also be capped specifically at the ends. Balci *et. al.* had showed in his previous work that TMV can be capped specifically at their ends by Au nanoparticles (figure 1.3) [9]. Similarly it was shown that TMV can be metallized by Ni particles using electroless deposition specifically at the ends (figure 1.4) [10].

The above four points led us to devise a strategy of encapsulating a Pt(II)-containing anticancer drugs inside the channel and cap/block the channel by magnetic nanoparticles. Magnetic nanoparticles would cap TMV at the ends to keep the drug inside the channel and would then be removed by the application of an external alternating magnetic field or by the pH variations in the cancer cell to release the drug and induce local heating (hyperthermia). Similarly we would link inorganic and organic molecules (such as magnetic nanoparticles, polyethylene glycol (PEG) and antibody fragments for selective delivery) to the exterior protein residues of TMV. Our previous experience with TMV and collaborations with other groups (Christina Wege, Stuttgart University, Germany) motivated us to participate in the MAGNIFYCO project (NMP4-SL-2009-228622) using TMV as an assembly for drug delivery with combined hyperthermia.

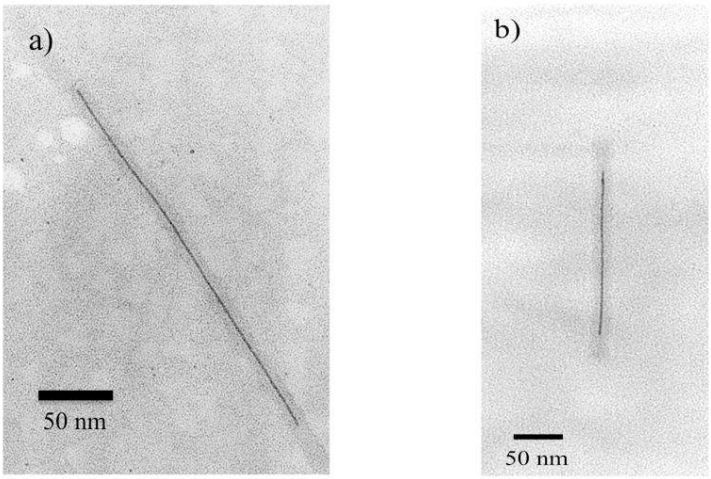

Figure 1.1. Transmission Electron Microscopy (TEM) images of (a) two (end-to-end aggregated) virion particles containing thin metallic nanowires of Ni [6] and (b) a single virion particle containing a Co nanowire synthesized in the central channel of TMV [7]. The wires appear dark inside (grey) TMV.

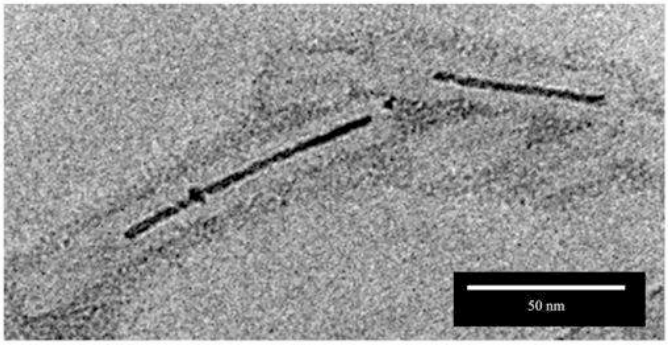

Figure 1.2. TEM image of Co-Pt alloy in the central channel of TMV [8].

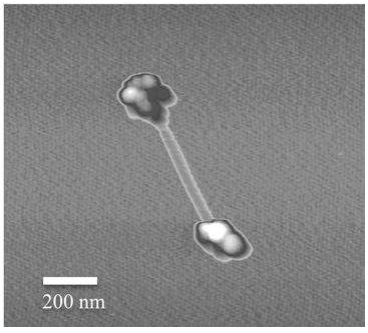

Figure 1.3. Atomic Force Microscopy (AFM) image of TMV particle with Au nanoparticles attached at the ends of TMV are selectively grown via electroless deposition [9].

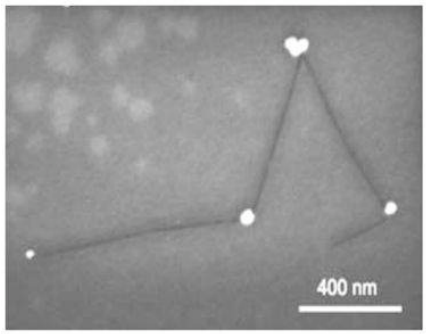

Figure 1.4. Scanning Electron Microscopy of (SEM) image of TMV (black) rods with Ni nanoparticles (white spheres) attached at the ends only [10].

CHAPTER 2

INTRODUCTION

2.1 Tobacco Mosaic Virus

Tobacco Mosaic Virus (TMV) is an RNA-containing plant virus that causes diseases in tobacco, tomato, cucumber and other plants of the *Solanaceae* family [11, 13]. However it is non-pathogenic for humans and other mammals and does not cause any diseases in them, as it is efficiently neutralized by the immune system [2]. TMV is an extremely stable structure that could retain its infectivity even after 50 years [13]. It is the first ever discovered virus in the history of virology [14]. In 1883 Adolf Meyer and his colleague Beijerinck reported that the causative agent of mosaic disease of tobacco plants is a non-bacterial pathogen but it was Ivanovski who showed successfully the existence of TMV in 1892 [15]. In 1946 W.M. Stanely was awarded the Nobel prize for his work regarding the transmission electron microscopy (TEM) of purified TMV particles and for proving that the virus remains active even after crystallization [14, 15]. A. Klug was awarded the Nobel prize in Chemistry in 1982 for the structural elucidation of nucleic acid in TMV.

2.1.1 TMV Structure

TMV is a rigid helical rod which is 300 nm long with an exterior diameter of 18 nm. It also contains a cylindrical inner channel of 4 nm. It is composed of a single stranded RNA and 2132 identical coat proteins. The coat proteins are arranged around RNA in such a way that in an assembled TMV the nucleic acid is compactly coiled in a helix of the protein subunits. The RNA contains 6396 base pairs (in the strain *vulgare*). The RNA and coat proteins of TMV results in 131 turns, 16.33 proteins per turn with a pitch of 2.3 nm per turn [12-15, 16] (figure 2.1). The composition of the particle is approximately 95% protein and 5% RNA. Purified preparations of TMV contain a population of rods with variable lengths, either longer than 300 nm or shorter. Intact

(300 nm) or shorter TMVs, both have the tendency to make end-to-end aggregates under appropriate conditions, resulting in a wide range of lengths. Shorter TMV particles could be partially assembled viruses at the time of isolation, or broken parts of intact viruses during isolation and purification [13].

TMV coat protein has a total number of 158 amino acid residues and a molecular weight of 17.5 kDa. The viral protein consists of a high proportion of secondary structure with 50% of the residues making four α-helices (which are packed together to make a barrel structure) and 10% of the residues make β-sheet structures [13, 17]. The core of the subunit is composed of four antiparallel α-helices (residues 20-32, 38-48, 74-88 and 114-134). The central part of the subunit contains a cluster of aromatic amino acids (Phe^{12}, Trp^{17},Phe^{62}, Tyr^{70}, Tyr^{139}, Phe^{144}) which results in a hydrophobic interior patch in the barrel. The distal ends of the helices are connected transversely by a narrow and twisted strip of β-sheet (figure 2.2). Some of the loops in the protein structure are stabilized by calcium ions by interacting with the carboxylate side chains of the acidic amino acids (Glu, Asp), some main chain carbonyl groups and water molecules. The N and C termini lie distally [13, 18, 19].

2.1.2 Charges In and Out on TMV at Different pH Values

The charges on the TMV protein externally and inside the channel could be very different depending on the pH. The isoelectric point of TMV coat protein is 3.5, while that of the TMV particle is 2.8, and therefore below this pH regime TMV is positively charged on the exterior because the acidic amino acids undergo protonation [15]. At neutral pH values the viral particle is mainly deprotonated and therefore has an overall negative charge stemming partially from the RNA. Lower pH values and protonation of the acidic amino acids can decrease the stability of the protein because the loss of charges of these residues could weaken the interaction with calcium ions and hence leads to the disassembly of TMV [16-19]. (Charges in and out of TMV at different pH values are shown in figure 5.3.9 in chapter 5.3: *TMV Au Binding and Decoration*). Incubating TMV particles at highly basic pH values, i.e 8-9, destroys (disintegrates) them (see section 5.3.2.6, *"Stability of Au decorated TMV rods after synthesis"* in chapter 5.3).

2.1.3 Physical Properties of TMV

TMV is a very stable protein tube. Thermally it can withstand temperatures up to 85 ºC. Similarly the virus remains intact in a wide range of pH values, i.e. 2.8-8.5 [11, 13, 14]. We have also observed intact TMV particles in a number of experiments at pH as low as 2.3. TMV can be dried and stored in dry form at room temperature for a long period of time, i.e. more than 40 years. TMV can also resist solvents such as ethanol. Ethanol is also used in the precipitation of TMV from solutions. It can also resist dimethylsulfoxide (DMSO) dissolved in water up to 70 % (volume). The electron microscopy already proves that TMV remains intact in high vacuum.

2.1.4 TMV as a Biotemplate for Fabrication in Nanotechnology

Biotemplates are preferred over artificial composites for nanofabrication, and the reason is that a sample of artificial nanostructures does not have 100% identical size distribution, but on the other hand biological molecules have perfectly identical size, shape and chemical composition. This led to search for biotemplates that can be used in nanotechnology. An ideal biotemplate should be stable enough to withstand the harsh physical and chemical conditions that it may be exposed to during nanofabrication. As it is already stated, TMV is a stable entity that can remain intact in a wide range of temperatures and pH. Moreover, the presence of specific chemical functional groups on the TMV is an enormous advantage that very few organic or inorganic nanostructures (such as polymers artificially synthesized in labs) would provide. Yet there exist possibilities of the modification of these functionalities by genetic engineering and exposing new side chains to exploit for chemical binding. All these facts make TMV one of the best suited biotemplates in nanotechnology [12]. The use of TMV as a biotemplate dates back to 1940 when Kausche used it for the deposition of Au nanoparticles [20, 12]. But only over the last one or two decades TMV has been extensively used for nanofabrication, e.g. deposition of inorganic/organic materials on the coat protein as well as inside the 4 nm channel. In 1999 Shenton *et. al.* reported the deposition of inorganic nanoparticles on the TMV coat proteins. They successfully

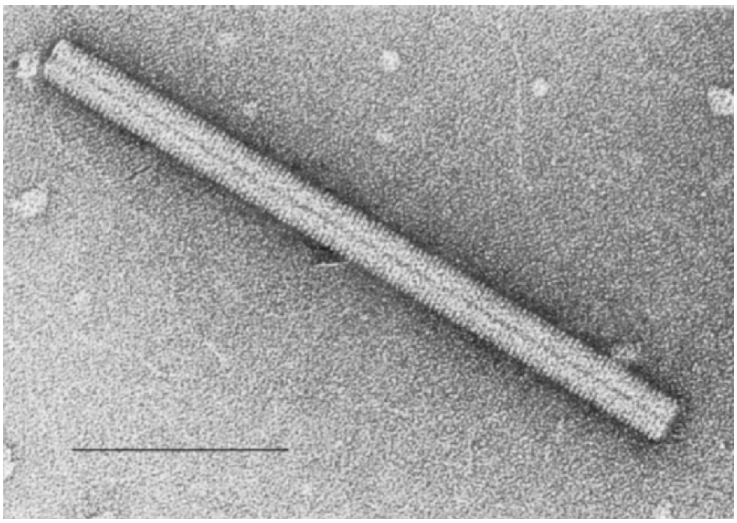

Figure 2.1: TEM image of a TMV. The virus is negatively stained with uranyl acetate. The 4 nm channel is visible as a dark (black) line. The 2.3 nm pitch (helical groove) is evident on the exterior. Scale bar: 100 nm. Image taken from [22].

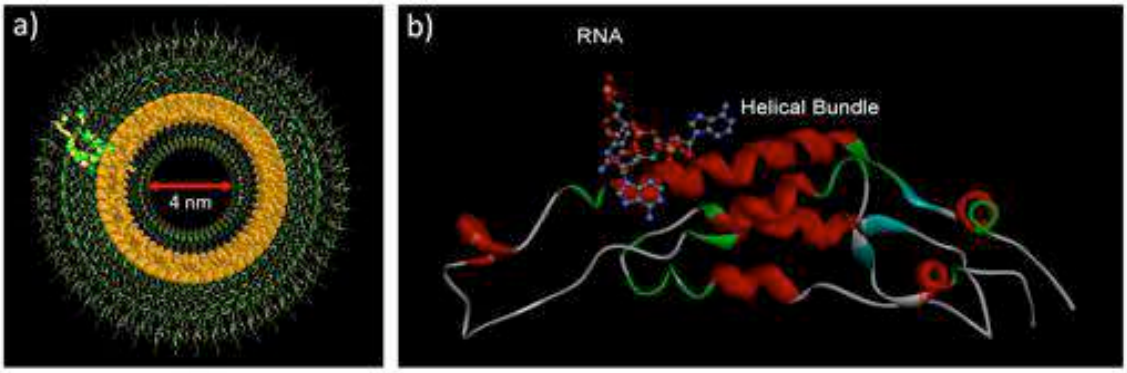

Figure 2.2: (a) TMV graphics generated by RasMol from PDB entry "2TMV" [19]. The image shows front view of 49 coat proteins (three helix turns). A channel of 4 nm and exterior diameter of 18 nm is visible. The protein backbone is shown as ribbons in green and yellow colour while RNA is depicted as spacefilled in orange colour. (b) A single coat protein of TMV shown graphically. Graphics are generated by Discovery Studios Viewer from PDB entry "2TMV" [19]. RNA is shown in a "ball-&-stick" model while the protein backbone is depicted as "solid ribbon". The model shows a four α-helix bundle as red and β-sheets as blue solid ribbons. The model (2TMV) does not contain the last four amino acids 155-158.

assembled and deposited CdS, PbS, SiO_2 and iron oxide on TMV [21]. Similarly a number of metallic depositions have been reported on the TMV coat protein as well inside the channel. Knez *et. al.* successfully deposited Ni, Au and Pd on TMV [6].

The same group also reported the synthesis of (3 nm) Ni, and Co wires inside the channels of TMV [6, 7]. Au nanoparticles have been successfully bound and grown or enlarged, to the TMV ends [9]. Au, Pd, Ag and Co-Pt nanoparticles could also be reduced on the surface of TMV either with wild type viruses or genetically modified ones with new functional groups exposed on its surface or inside the channel to provide more nucleation sites [5, 23 - 25]. ZnO has been precipitated on the TMV surface for making devices and the results show that both, wild type as well as genetically engineered (mutant) TMVs could be used [26]. TMVs are also used as porous electrode scaffold for batteries [27]. TMV has been also coated with a conductive polymer (polyaniline) on its surface to design new devices [28]. A number of other organic and inorganic materials have been successfully deposited on TMV because of its high stability and thorough understanding of its chemical structure. To put in a nutshell TMV is a promising biotemplate for a number of nanoparticles synthesis and/or deposition on its surface and in the channel, too.

2.2 Platinum (Pt) containing Anticancer Drugs

Cisplatin also known as *cis*-diamminedichloroplatinum(II) [*cis*-$PtCl_2(NH_3)_2$] has been known for over 150 years. It is a Pt(II)-containing drug that was discovered by chance by Barnett Rosenberg and his team while working with cultures of the bacteria *Escherichia coli* [29, 30]. But the synthesis of cisplatin is even older and dates to 1844, when it was called Peyrone's Chloride [30]. Since the time of its discovery, over 3000 platinum derivates have been chemically synthesized and tested for effect against cancers, but only 30 of them reached the clinical trials. Amongst these 30 already more than half were rejected soon after initial trials [29-31]. In addition to cisplatin, carboplatin and oxaliplatin are currently used in therapies against human cancers [29, 32, 33]. These three, and also nedaplatin are currently available in the market [30].

2.2.1 Chemical Structure & Reactivity

All four drugs are Pt(II) complexes, but their chemical structures differ from each other as shown in figure 2.3 [31]. Cisplatin, carboplatin and nedaplatin each contain two ammine groups (ammonia molecules) in the *cis* orientation. Cisplatin has two chlorides as the 'leaving' groups; carboplatin has a cyclobutanedicarboxylate while nedaplatin has a glycolate moiety as leaving group [29, 31, 33, 34]. It has been reported by a number of groups that the human metabolism results in the double aquation of these drugs, giving rise to one single potent form of these three drugs, diaquo-diammino-platinum(II) as shown in figure 2.4 (left hand side) [30] . Despite the fact that diaquo-diammino-platinum(II) is the active metabolite of these three drugs, there could also be intermediate derivatives such as monocholoro- or dichloro-diammine species, which means that carboplatin and nedaplatin could be assimilated to precursors of cisplatin [30, 31, 35]. There are always substantial concentrations of Cl^- present in both blood (100 mM) and inside the cell (4 mM) [34]. Oxaliplatin (*trans-R,R*-cyclohexane-1,2-diamine)oxaloplatinum(II) on the other hand contains a 1,2-diaminochyclohexane (DACH) ligand (figure 2.3) having an oxalate as its leaving group [36]. The oxalate group is displaced by water and Cl^-, yielding a monochloro-, dichloro-, and diaquo-diaminocyclohexane-platinum [30] (figure 2.4- right hand side and figure 2.6).

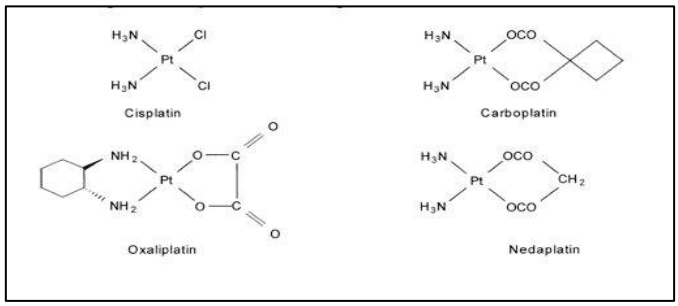

Figure 2.3. Chemical structures of cisplatin, oxaliplatin, carboplatin and nedaplatin.

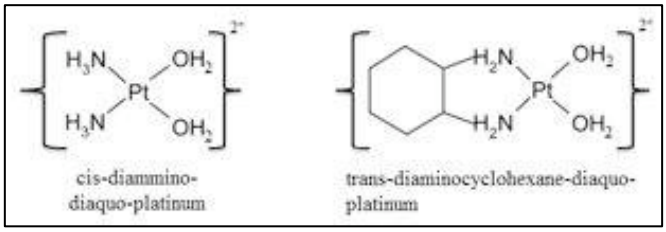

Figure 2.4. Active metabolites of the four Pt drugs.

In summary, the four Pt-containing drugs could be considered as ‘pro-drugs’. The key step in transforming them to become active drugs is their hydrolysis. Hydrolysis of these drugs has different kinetics for each one of them, for example, the hydrolysis of cisplatin is extremely rapid while its slower for oxaliplatin, carboplatin and nedaplatin [29-34, 37]. Hydrolysis of cisplatin and oxaliplatin (used in this thesis) are shown schematically in figures 2.5 and 2.6 [31].

2.2.2 Hydrolysis of Cisplatin and Oxaliplatin

Cisplatin is activated when it enters the cells. In the physiological pH (7.2-7.4) of the cell one of the chloro ligand is replaced by a water molecules and forms the monoaqua complex of the drug. Further substitution of the second chloro ligand by another water molecule is also possible. If both of the Cl^- are replaced by water molecules, it is known as a diaqua complex. This complex can make DNA-Pt adducts. Depending upon the pH of the environment there could be some other transformation from the aquated and even non-aquated complexes of cisplatin. In case of a highly basic environment (pH 8.5 or above), one or both of the water molecules could be deprotonated and result in monoaquahydroxo or dihydroxo complexes. This can render the drug inactive by making dimers and trimers. (There is also a possibility of replacing a chloro ligand by an OH^- instead of water at highly basic pH, i.e. 8 and above). Oxaliplatin unlike cisplatin is less stable with growing chloride concentration. In aqueous/biological media it spontaneously undergoes transformation and yields $Pt(DACH)Cl_2$ as its main product under physiological conditions. The oxalate group can be substituted by nucleophic groups such as HCO_3^- or Cl^- ions, and also by H_2O. Hydrolysis of oxaliplatin is schematically shown in figure 2.6 [31].

2.2.3 Mode of action

The diaquo-platinum species can react with DNA molecules and form DNA-Pt adducts. The mode of action of these drugs to kill cancer cells relies on the fact that they render the cellular machinery incapable of DNA synthesis and saturate their capacity to repair DNA adducts [30]. The covalent interaction (in the form of DNA-Pt adducts) results in crosslinking of the nucleotides which distorts the geometry of the DNA molecule. A number of essential cellular processes such as DNA replication, RNA transcription

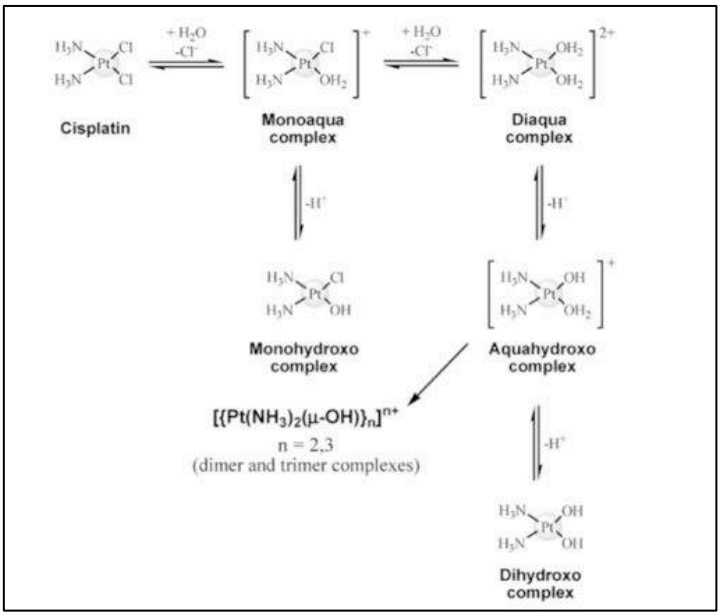

Figure 2.5. Hydrolysis of cisplatin [31]

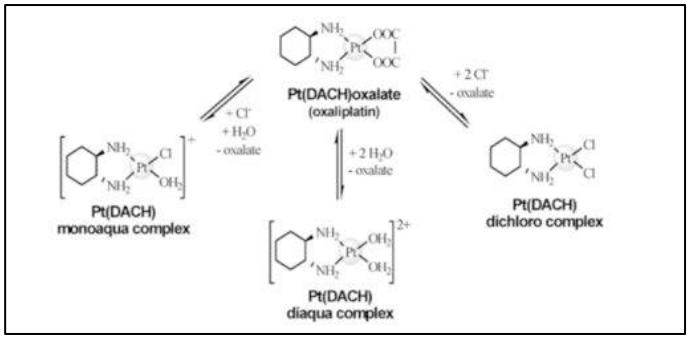

Figure 2.6. Hydrolysis of oxaliplatin [31].

and protein synthesis are inhibited as result of these kinks in the DNA molecule. As a consequence apoptosis is induced and eventually the cells are killed. Some of the reported apoptosis genes that are involved in the (programmed) cell death via Pt(II)-containing drugs are *p53* and the *bcl-2* gene family [29, 30]. Most of adducts formed are intra-strand crosslinks (60-65%) between adjacent guanine bases while there are also inter-strand crosslinks, monofunctional adducts and protein-DNA crosslinks [31, 38]. The mode of action of a Pt(II)-containing drug (cisplatin) is shown in figure 2.7 [31].

The preferred binding site (in case of cisplatin, oxaliplatin and carboplatin) is guanine N7. The Pt(II) of these drugs can also bind, to a lesser extent, to adenine N7, and platination of cytosine N3 and adenine N1 is also possible. The reason why purines are preferred over pyrimidines is attributed to the high nucleophilicity of the imidazole ring in purines [31].

Cell death occurs by triggering apoptosis by the administration of these Pt(II)-containing drugs but in some cases the platinated DNA can also be repaired, providing the cells with resistance to these drugs. Many mechanisms for resistance against cisplatin have been reported and since the active metabolites of other drugs are either identical to cisplatin or they react in an identical manner, the same resistance mechanisms could possibly be activated by cells against other Pt(II)-containing drugs, too. [29-31]. One of the resistance mechanism to Pt(II)-containing drugs is when the NH_3 ligands are lost by the drug. This is done by coordination to S-donor cysteine residues of the cytoplasmic tripeptide glutathione (GSH). GSH reacts with Pt(II)-containing drugs (such as cisplatin) and forms deactivated conjugates that are readily excreted from the body. The reaction with GSH may occur spontaneously or with the help of glutathione-S-transferase. The ultimate result is that the Pt(II)-containing drug loses its NH_3 ligands [39, 40]. A class of low molecular weight metalloproteins have also been elucidated to remove the NH_3 ligands from Pt(II)-containing drugs. Mammalian metallothionein (MT) is one protein known for binding cisplatin. It is a small protein of 62 amino acids with 20 cysteine residues. When cisplatin binds to MT, the drug loses its NH_3 ligands and displaces from MT heavy metal cations (such as Zn^{2+}) [39, 41].

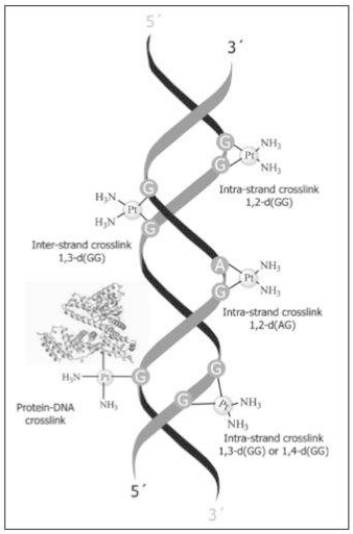

Figure 2.7. Mode of action of cisplatin [31].

2.3 Magnetic Nanoparticles in Medicine

In the last decade, nanotechnology has made huge progress and now it is possible to fabricate, characterize and tailor the functional behavior of nanoparticles for biomedical sciences [42]. Nanoparticles are ideally suited for the construction of structures and materials with adjustable chemical and physical properties [43]. Iron oxide nanoparticles have been used in *in vitro* diagnostics for over 40 years, but extensive research work for the last one or two decades has uncovered several types of iron oxides that could be used for a number of biomedical applications. Iron oxide nanoparticles can be one of the following types with respect to their magnetic properties.

a. Ferromagnetism: Ferromagnetism is a property of a group of atoms or molecules in a solid crystal. Ferromagnetic particles have a spontaneous magnetic moment even in the absence of an applied magnetic field [44]. The spontaneous magnetization results from the atomic magnetic moments due to electronic spin. Furthermore, in ferromagnetic materials coupling interactions cause net spin magnetic moments of adjacent atoms to align, even in the absence of an applied magnetic field (figure 2.8a). This type of magnetism is displayed by transition metals such as iron (Fe), nickel (Ni), cobalt (Co), some of the rare earth metals, e.g. gadolinium (Gd), many alloys, and by many metal complexes such as oxides [45].

b. **Antiferromagnetism:** Antiferromagnetic materials consist of two ferromagnetic sub-lattices with antiparallel magnetizations, i.e. the alignment of the spin moments of neighbouring atoms or ions in exactly opposite directions (therefore no spontaneous magnetization is present). Manganese oxide is one material that exhibits this behaviour (figure 2.8b) [44-46].
c. **Ferrimagnetism:** Ferrimagnetic materials have both parallel and antiparallel ordering of their constituent magnetic moments (figure 2.8c). A net spontaneous magnetization results even in the absence of field because there is an excess of parallel spins over the antiparallel ones. Yet another reason could be that parallel moments are larger than the antiparallel counterparts. Ferrimagnets behave in most applications practically as ferromagnets [45, 46].
d. **Superparamagnetism:** Superparamagnetism can be exhibited by ferromagnetic and ferrimagnetic materials. This phenomenon is displayed by particles of very small sizes (1-10 nm). Superparamagnetic particles are single domain materials and when they are placed in magnetic field, they will magnetize in an analogous manner to multidomain (ferromagnetic) materials. However, after the removal of applied field they retain no net magnetization. The magnetic dipole moments of individual superparamagnetic particles will be randomly oriented owing to thermal agitation [46].

Of the different types of iron oxides, two of the utmost importance are magnetite (Fe_3O_4) and maghemite (γ-Fe_2O_3) [43, 47]. Magnetite is a well-known ferrimagnetic iron oxide that has cubic inverse spinel structure with oxygen making an FCC closed packing while Fe cations occupy the interstitial tetrahedral sites and octahedral sites [43, 48]. Maghemite on the other hand has a similar (crystal spinel) structure and is synthesized as the weathering product (oxidation) of magnetite. It has a similar crystal structure as magnetite but in maghemite all the iron cations are in the trivalent state and the charge neutrality of the cell is guaranteed by the presence of cation vacanices [44]. Another well-known iron oxide is hematite (α-Fe_2O_3). Since hematite is antiferromagnetic, it is not exploited for applications in medical sciences [48].

For superparamagnetic nanoparticles, thermal fluctuation provokes the activation of remagnetization processes, as the energy barrier for the reorientation of magnetic moment of the nanoparticle decreases with the decrease in particle size. Magnetic nanoparticles offer many advantages in biomedical sciences such as they have

controllable sizes from few nanometers to tens or hundreds of nanometers making them comparable to those of a cell (10-100 μm) or a virus (20-450 nm) or even proteins (5-50 nm) [49], and since they are magnetic and therefore would be manipulated by an external magnetic field.

Magnetic nanoparticles are used in biomedical science for the following applications:

2.3.1 Cell labelling and magnetic separation: The use of magnetic nanoparticles for cell labelling and separation is already relatively old and an established technique. They can be used for sample purification for (subsequent) analysis in a two-step process, i.e. (i) tag the desired cells with magnetic nanoparticles and (ii) separate out the tagged cells through a fluid-based magnetic separation device (figures 2.9a and 2.9b) [42, 43].

2.3.2 Drug delivery: Conventional cancer chemotherapies suffer from a disadvantage that they cannot deliver the drug specifically to only cancer cells but to healthy cells too. This led to use magnetic nanoparticles (by tagging drug carriers) to deliver the drug specifically to cancerous cells only. This would reduce the amount of systemic distribution of the drug, (therefore reducing side-effects of the drug), and reduce the dosage because of efficient and localized targetting of the drug. In this method generally an anticancer drug is attached to a biocompatible magnetic nanoparticle carrier in solution and is injected locally to a patient. After the entry of the particle into the blood stream, these particles are concentrated via an external high magnetic field gradient at a specific site. Ultimately the drug is released either by pH change or enzymatic activity etc. (figure 2.9c). [42, 43, 50, 51].

2.3.3 Magnetofection: In magnetofection, DNA is bound to polycation-coated magnetic nanoparticles. The “magnetic DNA molecules” are transfected into cells by an external magnetic field. Magnetofection has proved to be more efficient than conventional vectors of genetic engineering up to several thousand times [43, 24]. HUVEC (Human Umbilical Vein Endothelial Cells) have shown up to 360 fold more efficient expression of luciferase reporter gene in cultures when magnetofection was used, in comparison with conventional gene transfer [52].

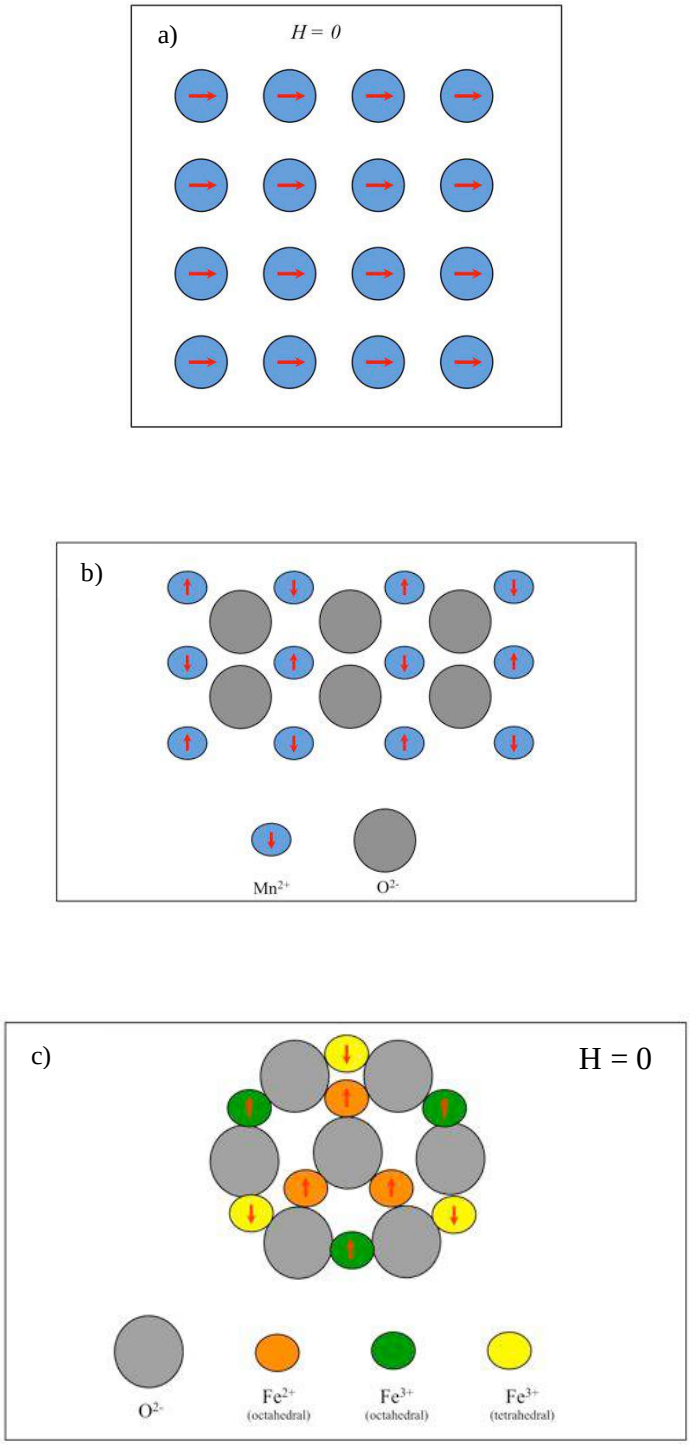

Figure 2.8. Schematic illustration of (a) mutual alignment of atomic dipoles for a ferromagnetic material. It exists even in the absence of an applied magnetic field. (b) Antiparallel alignment of spin magnetic moments for antiferromagnetic manganese oxide. (c) Spin magnetic moment configuration for Fe^{2+} and Fe^{3+} ions in ferrimagnetic Fe_3O_4. All illustrations are adapted and redrawn from reference [45].

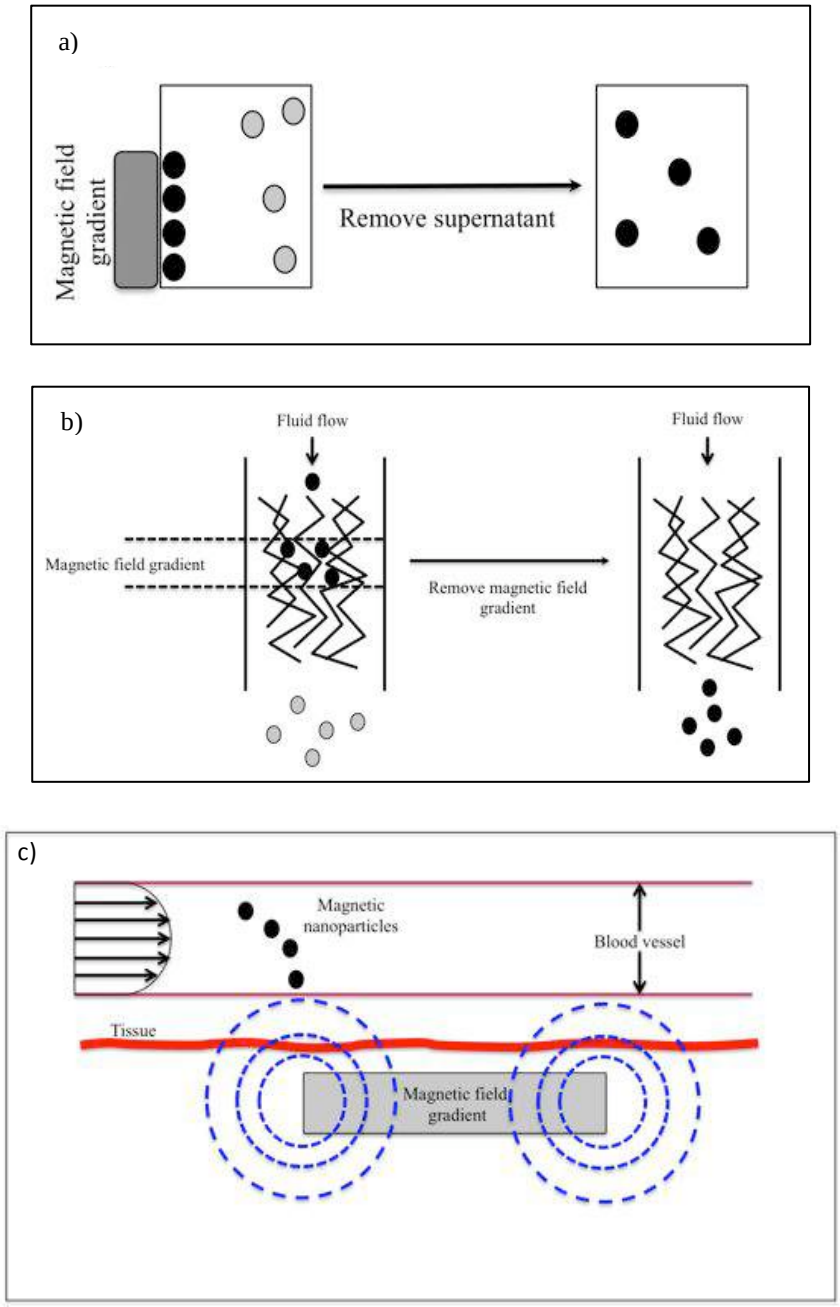

Figure 2.9. Schematic illustrations showing (a) magnetic cell separation: a magnet attached to the container walls retains the magnetically tagged cells (black spheres) while the undesired (white spheres) are removed as supernatant. (b) A solution containing both magnetically tagged and unwanted cells. The flow through a region of high magnetic field gradient retains the magnetically tagged ones (black spheres) while it lets undesired (white spheres) pass through. Removing the magnetic field results in purified cells. (c) Magnetic drug delivery: an external magnetic field gradient is applied to capture magnetic drug carriers flowing in blood vessel for targeted delivery. Illustrations 9a and 9b are adapted and redrawn from reference [49] while 9c from reference [42].

2.3.4 Magnetic Resonance Imaging (MRI): Superparamagnetic iron oxide nanoparticles (SPIONs) are used as MRI contrasting agents in biomedicine to differentiate between healthy and pathological tissues [43]. Recent developments in MRI have made it possible now to image and follow cells, tissues and gene expression products *in vivo* at near microscopic resolution [48-5]. Apoptosis can also be detected via MRI [56].

2.3.5 Hyperthermia: Hyperthermia has been used for the treatment of malignant tumors for over 2000 years. For example, Hippocrates suggested that surface tumors could be cauterized by the application of hot iron [43]. Magnetic hyperthermia refers to one of the therapies for cancer treatment in which magnetic nanoparticles are injected at the site of the tumor and the tumor is then exposed to an external alternating magnetic field [42, 43, 57, 58]. Healthy cells of the body can survive to temperatures up to 42-45 ºC while cancer cells die at/around 42 ºC. Magnetic hyperthermia aims to heat the tumors in the temperature range of 42-45 ºC which would destroy tumor cells and give minimal damage to normal/healthy cells of the body. Living tissues do not absorb magnetic field and therefore it can be applied to deep regions in a living body. When an external variable magnetic field is applied to magnetic nanoparticles inside the tumor, it results in heat generation due to magnetic hysteresis loss [42, 43, 57, 58]. The amount of heat generated depends on a number of factors such as magnetocrystalline anisotropy, size, shape and microstructure of the nanoparticles as well as magnetic field parameters [43, 58, 59].

The heating of magnetic nanoparticles upon exposure to external alternating magnetic field results as a consequence of loss processes during the reorientation of the magnetization. [58, 60]. An external applied magnetic field actually supplies the energy assisting magnetic moments to overcome the energy barrier for remagnetisation. When the moment of the nanoparticles relaxes to equilibrium orientation, the energy dissipates in the form of heat. This way of heat generation is termed Neél relaxation and is used to kill cancer cells via hyperthermia [49, 57, 58]. Usually less important is heating due to frictional loss

when the viscosity of the environment is low enough for the nanoparticles to rotate [58, 60].

Clinical Example of Hyperthermia: One of the partner companies (MagForce, Germany – www.magforce.com) of MAGNIFYCO project has already started clinical trials of hyperthermia with patients of recurrent glioblastoma multiforme. 66 patients (59 with recurrent glioblastoma multiforme) were given the treatment with intratumoral thermotherapy procedure using magnetic (iron oxide) nanoparticles. The hyperthermia treatment leads to longer survival compared to conventional therapies in the treatment of recurrent glioblastoma. Moreover, neither serious complications were observed nor major side effects [61].

2.4 Human Ovarian Cancer & MAGNIFYCO

2.4.1 Human Ovarian Cancer

Ovarian cancer is the fifth leading cause of death amongst women [62]. According to 'Cancer Facts & Figures' 2009, more than 15,000 women die annually because of (epithelial) ovarian cancer while ~22,000 are diagnosed with the cancer [63]. The majority of the women having developed ovarian cancers are diagnosed at the advanced stages because earlier stages are rather asymptomatic. Most common symptoms of ovarian cancer are vague abdominal pain and bloating, abdominal distension and fluid retention, and bowel obstruction. Early detection is essential and the most promising approach to cure the cancer and improve the long-term survival of the patients [62, 63]. Epithelial ovarian cancer is the most common ovarian cancer and its onset is 59 years but it may appear at younger ages in women who have a history of ovarian cancer in their families [62, 64]. Other types of ovarian cancers could be ovarian serous carcinomas (SCA), serous borderline tumors (SBT) and mucinous ovarian cancers (MOCs) [64].

Dysfunction of a number of genetic and molecular processes are reported to be the cause of ovarian cancers. There are at least four noteworthy processes which favour the development of the cancer [63].

a. **Cell Cycle Genes:** A number of human cancers including human ovarian cancer are developed because of the dysfunction of the cell cycle. Malfunctioning of cell cycle genes and their regulatory protein factors are identified in case of ovarian cancer, for example cytoplasmic p27 [65]. In malignant ovarian tumors a relationship between p27 and Jab1 has been found. The overexpression of Jab1 causes the nuclear exportation of p27 to cytoplasm and dissociates it from the complex of Cdk2/Cyclin. This way Jab1 acts as a negative regulator of p27 and is therefore associated with the progression of ovarian tumors [66].
b. **Transcription Factors (TFs):** TFs control the gene expression during cell cycle and other physiologically important cellular processes. Several studies show that TFs play a role in the pathway for the development of ovarian (serous) carcinomas. Transcription factors 'E2F1' and 'E2F3' have been identified to be related with ovarian cancer symptoms development in women [63].
c. **MicroRNAs (miRNAs):** miRNAs are a recently discovered group of RNAs that play a role in the regulation of gene expression. In a number of other cancers, miRNAs are frequently deregulated. They are deemed of playing roles in ovarian cancers too. Recently at least three types of miRNAs were discovered that play a role in the development of ovarian cancer: 'miR-214', 'miR-199' and 'miR-200a' [63].
d. **Histone Deacetylase Inhibitors (HDACIs):** Over the past few years, several results pointed towards the involvement of HDACIs in cancer symptoms. HDACIs can inhibit cell growth, revert oncogene-transformed morphology, induce cell differentiation and apoptosis. HDACIs are found to play an important role in the proliferation of ovarian cancer cells [63].

Detailed description of the involvement of above-stated processes and proteins in human ovarian cancer development is above the scope and subject of this thesis and therefore, interested readers are referred to references [63, 67-72].

Standard treatment of ovarian cancers includes the surgical removal (cytoreduction/debulking) of the tumors plus a chemotherapy with a platinum/taxane combination [73]. The rate of recurrence is unusually high despite initial therapy. Statistically 50-75% of the patients would experience the disease development again. In these patients, the second-line chemotherapy includes palliation of symptoms, surgery, radiation and hormonal therapy [73]. Recurrent ovarian cancers can be treated in

different ways depending upon the bulk of recurrent disease and the time between last treatment with chemotherapy to subsequent relapse, i.e. treatment-free interval. The cure may include a second debulking via surgical removal and chemotherapy with Pt or non-Pt drugs such as liposomal doxorubicin, topotecan or etoposide, but the response rates are as low as 10-15% [70].

2.4.2 MAGNIFYCO

MAGNIFYCO stands for **Mag**netic **N**anocontai**i**ners **F**or Combined H**y**perthermia and **Co**ntrolled Drug Release. It is an EU-FP7 project that has been designed to combine biological and non-biological subunits in novel smart nanotools for drug encapsulation and controlled release, combining it with magnetic hyperthermia for the therapy of human ovarian cancer. It is a collaborative project that involves a number of partners spread all over Europe. Every particular partner is an established expert with innovative teams of scientists. The project is run by a thorough sharing and collaboration of results, facilities and expertise. The strategy applied in MAGNIFYCO is based on the optimal selective delivery of known chemotherapeutics by magnetic nanocontainers. These containers have the capability to perform in concomitance drug delivery and hyperthermia treatment for a multivalent approach to cancer therapy. The main strategy of MAGNIFYCO can be summarized in the following points (figure 2.10).

a. Synthesis of magnetic colloid nanoparticles with control over size, shape, composition and magnetic properties. Magnetic nanoparticles are key to achieve good results for hyperthermia.

b. Preparation of different kinds of nanocontainers for drug encapsulation. In this regard, we have been working on TMV as our drug carrying nanoscaffold (see "Motivation", chapter 1). Other nanocarriers are zeolites, cellular vesicles, peptide nanotubes and solid-lipid nanoparticles.

c. Assembly of magnetic nanoparticles within the nanocarrier drug systems so that these carriers could perform a dual function of drug delivery as well as induction of local heating, i.e. hyperthermia (see section 2.3, *"Magnetic Nanoparticles in Medicine"* in chapter 2).

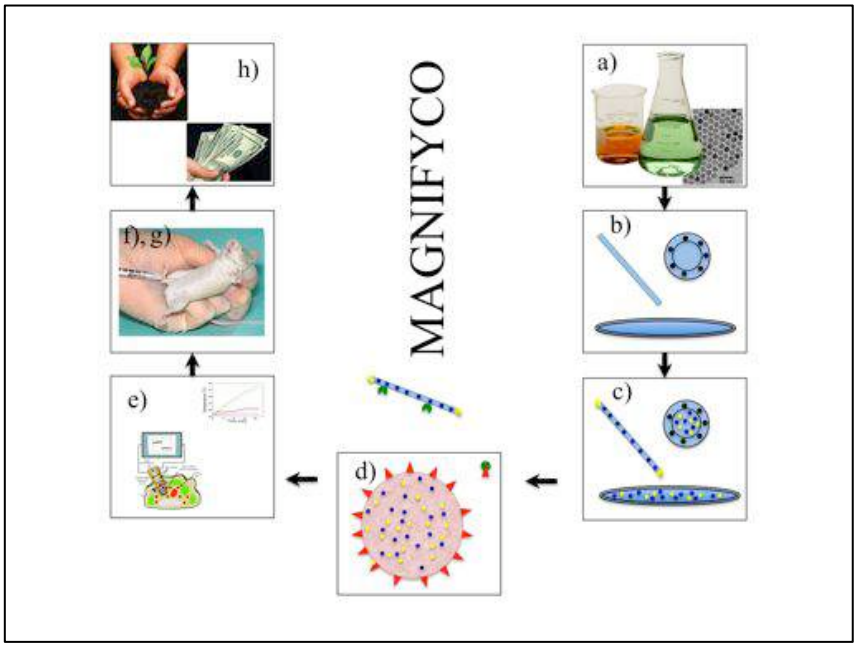

Figure 2.10. Schematic representation of different stages of MAGNIFYCO. A)synthesis of magnetic nanoparticles, b) development of nanoscaffolds to perform as drug carriers, c) drug encapsulation and assembly, d) surface functionalization with monoclonal antibodies, e)characterization and in vitro experiments, f & g) in vivo experiments and h) transition from science to market.

d. Functionalization of the nanocarrier scaffolds with monoclonal antibodies so that they could deliver the packaging only to cancer carcinomas. In this case, a monoclonal antibody fragment ('Fab') recognizes the folic acid receptor overexpressed on the cell membrane of ovarian cancer cells.

e. Characterization of the magnetic performance as well as drug releasing ability of the assembled nanoscaffolds *in vitro*. The results and analysis would indicate the best platforms for further *in vivo* tests.

f. *In vivo* characterization of the assembled nanostructures in model animals with respect to their pharmacokinetic properties, toxicity and immunogenicity.

g. Based on the results of *in vivo* tests in model animals, the best performing platform would be selected for subsequent *in vivo* efficacy testing.

h. The final step would be the transition of the treatment strategies from basic scientific understanding to market where preclinical tests would be developed and the treatment could be available to public.

CHAPTER 3

TECHNIQUES

3.1 Electroless Deposition

Electroless deposition (ELD) is a process well known for a number of years, for fabrication of metallic and non-metallic structures. In ELD a metal is deposited on another metallic or even non-metallic surface without the application of any external electric current, hence it is called “electroless deposition” [74]. Deposition of metals on conductive surfaces via external power source application (where electrons are supplied by the external current) is known as “electrodeposition” or galvanic deposition” (figure 3.1). In this type, it is easy to control the deposition with the applied current or potential [75, 76]. In ELD the electrons actually come from a reductant, which is a chemical reducing agent (figure 3.2), rather than an external power source. [74, 77, 78]. ELD (of metals) is an autocatalytic oxidation/reduction reaction in which metal ions are reduced on the surface of other metallic or non-metallic structures [79-82]. The metal to be deposited must carry out the oxidation of the reductant in such a way that after it reduces the metal ions to metallic state, the metal oxidizes the reductant. Autocatalytic means that the deposited metal can grow on the substrate, but also on its own surface and it catalyzes the oxidation of the reductant. ELD actually consists of two electrochemical reactions, i.e the reduction of the metal ion to its zero valent state and oxidation of the reductant chemical [74, 83]. The deposition process should ideally carry on until there are no more metal ions available in the metallization bath [74, 84].

An advantage of ELD is that non-conductive surfaces could also be metallized such as plastics, glasses and other insulating materials. This extends to nanoscale materials, and it includes biotemplates such as DNA, RNA, proteins, whole bacterial cells and viruses etc. [6, 10, 85-88]. The non-conducting surfaces have to “sensitized” or “activated” as the non-metallic surfaces cannot catalyse the reduction of metal ions. Therefore, they must be coated with catalytically active centres as starting nucleation points, e.g. noble

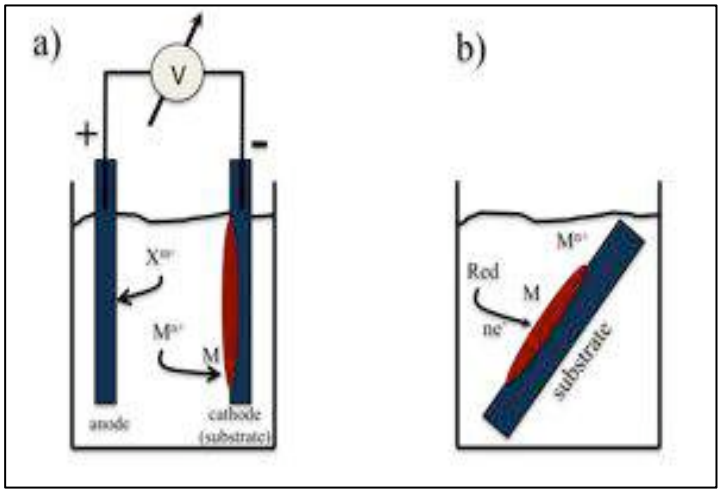

Figure 3.1. Schematic representation of experimental set-up for (a) electrodepositon and (b) electroless deposition. M^{n+}: cation, X^{m-}: anion, M: metal, and Red: reductant. Figure adapted and redrawn from ref. [84].

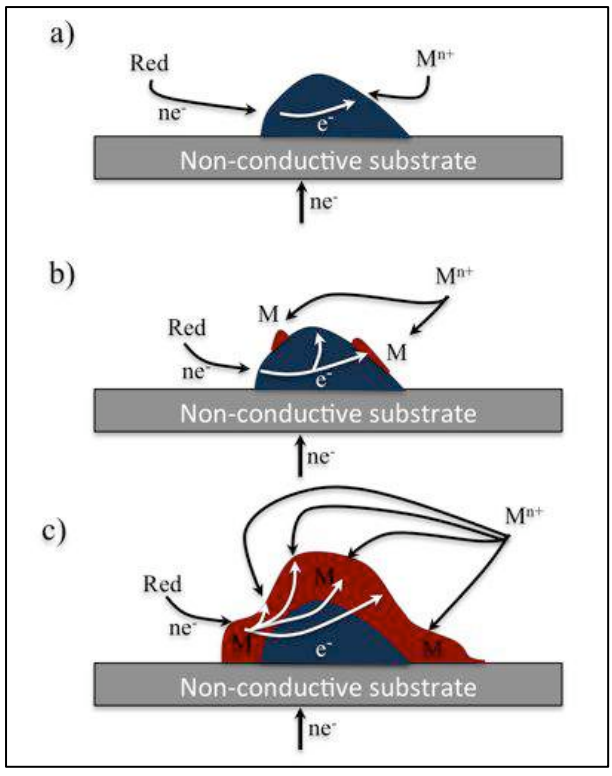

Figure 3.2. Schematic representation of electroless deposition. (a) firstly, the oxidation of the reductant occurs at an active centre (blue) inducing metal deposition, (b) small islands or particles of metal grow and (c) after their coalescence, the reductant has to react with the metal surface and growth proceeds. Figure adapted and redrawn from ref. [84].

metals such as Pt, Pd and Au. [78]. The surface with active centres (figure 3.2; blue spot) would then be the substrate as shown in figure 3.1b. Sensitization of surfaces could be as simple as dipping the surface to be fabricated in a solution of noble metal ions for a few minutes. The coating or the binding is mostly discontinuous, and this in turn can result in isolated clusters (figure 3.2b) or in a continuous sheath of the reduced metal at the end of the ELD process (figure 3.2c). Therefore, the process of sensitization is very important and depends on the desired structure to be achieved [10, 74]. As a rule of thump (figure 3.3), many small active centres are more likely to produce a continuous sheath of metal, while isolated big centres are merely "overgrown", as in figure 3.2 and figure 3.3(a). An important point to note is the fact that even galvanic deposition sometimes starts with sensitization of the structure(s) to be fabricated [74].

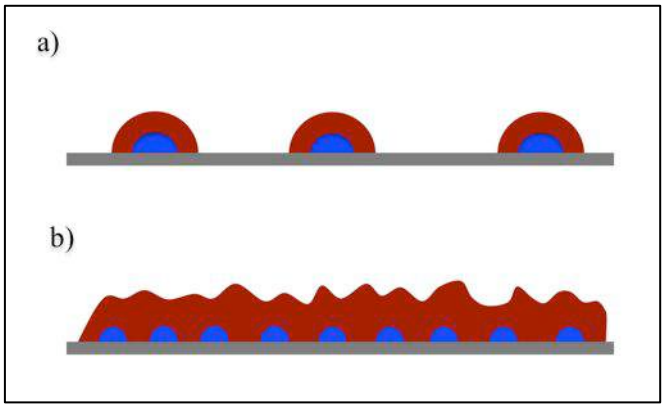

Figure 3.3. (a) Larger view for the case of figure 3.2. (b) Many small active centres closely spaced coalesce from centre to centre.

The metallization bath where the deposition of the metal happens after the surface has been sensitized consists of a metal complex of the metal to be deposited such as Ni, Cu, Pt, Co etc., a reductant as an electron source (DMAB, sodium hypophosphite, $NaBH_4$ etc.; this determines the ideal pH, which is crucial to the ELD), and additives such as complexing agents, stabilizers, inhibitors etc. needed to avoid too rapid deposition of the metal, or to provide solubility at high pH values [74, 75, 89, 90]. DMAB and other amine boranes are extensively used as reducing agents in electroless deposition because they are cheap and have low toxicity compared with other reducing agents. DMAB is also preferred because it functions at low pH values [91, 92]. DMAB is reported to work best at elevated temperatures (50-60 °C) and moderate pH values (6-8). Similarly, the higher the concentration of DMAB, the faster is the rate of metal deposition [91].

The metallization can sometimes be done in a range of pH values but with hugely differing rates. The evolution of hydrogen often takes place as a side reaction and can be seen as bubbles evolving in the bath solution [74].

3.2 SQUID

The Superconducting Quantum Interference Device is one of the best known tool for probing magnetic materials. It is considered as one of the most sensitive magnetic devices to measure low magnetic fluxes with high precision and accuracy. In middle Europe the earth's magnetic flux is in the order of 50 μT, a SQUID magnetometer is more sensitive by a factor of 5×10^5 [93]. The most sensitive SQUIDs are now available that could detect a moment of 10^{-8} emu (such as our MPMS S-VSM). A SQUID basically exploits two physical principles for its operation [94], i.e.

a. Quantization of the magnetic flux in superconducting rings, and
b. The Josephson effect.

For more detailed information about SQUID and its physical principles, the readers are referred to references [95, 96].

A typical SQUID (figure 3.4) set-up has a central coil and two symmetrical end coils. They all are connected in series with the end coils and in opposition to the central coil. The coils are coupled to the ring (of the SQUID itself) by a transformer. When a constant biasing current flows through the SQUID device, the measured voltage will oscillate with changes in the phase at the two junctions marked "x" at the bottom right of figure 3.4. This in turn depends upon the change in the magnetic flux. The flux change (that has happened) can be obtained by counting the oscillations [97, 98].

In this thesis a SQUID-VSM (SQUID-Vibrating Sample Magnetometer) is used for magnetic measurements. The sample is vibrated at a certain frequency (14 Hz) and a changing magnetic flux is not required to generate a signal in SQUID-VSM. The sample is vibrated only to create signal at a known modulation frequency and to aid the separation of sample signals from instrumental artifacts. Measuring the sample in the SQUID-VSM make the samples vibrate at a frequency about the very centre of the detection coils, where the signal peaks as a function of the sample position. It generates

a SQUID signal as a function of time. This technique efficiently removes the sample signal from other noise sources.

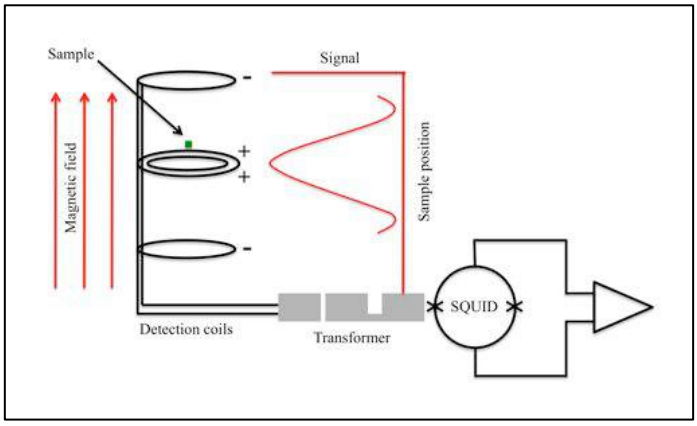

Figure 3.4. Schematic representation of a typical SQUID magnetometer [99].

3.3 Dynamic Light Scattering (DLS)

Light scattering has been used for a number of years to know about the structure and dynamics of the colloidal suspensions. When a colloidal suspension is hit by laser light, an oscillating dipole is generated by the electric field of the light in the particle and the particle scatters the incident light. The techniques which are used to monitor this scattered light fall into two sub-categories. Firstly, static light scattering, which is used for studying the average structural properties and secondly, the one for studying the dynamic properties, i.e. dynamic light scattering [100].

Dynamic Light Scattering (DLS) is often referred to as Quasi-Elastic Light Scattering (QELS) or Photon Correlation Spectroscopy (PCS). It is a method to characterize the size of molecules in solution. It takes only minutes to do a DLS measurement and to distinguish between a monodisperse and an aggregated sample and also measure the average size (diameter) of the particles [101]. DLS detects the temporal fluctuation of the intensity of the backscattered radiation due the effect of Brownian motion to obtain dynamic information of different length scales [100, 102]. In a colloidal system the particles are moving with a speed determined by the Brownian motion. Smaller particles move faster than their larger counterparts. As these colloidal particles move, the

scattered light would make a ‘speckle’ pattern that is fluctuating in time and space (figures 3.5a and 3.5b). These fluctuations are caused by Brownian motion, and can be monitored by a photon correlator and a time-dependent intensity correlation function is obtained [100, 103]. This function decays as a single exponent with a time constant which is directly proportional to the coefficient of diffusion (D) of the particles in the suspension. It is used to determine the average particle radii by using the Stokes-Einstein equation [101, 104];

$$d(H) = \frac{kT}{3\pi\eta D}$$

where;

d(H) = hydrodynamic diameter, D = diffusion coefficient, k = Boltzmann’s constant,

T = temperature, and η = viscosity of the solvent.

D can be determined from the equation of the time constant:

$$\text{time constant} = \frac{16\pi^2 n^2}{\lambda^2}\sin^2\frac{\theta}{2}D$$

where:

λ = laser wavelength (633 nm), n = refractive index of the solvent, θ = scattering angle (173º, in this case).

ZetaSizer ZS Nano (Malevern Instruments) has been used for DLS measurements discussed in this thesis. Its set up consists of six major units (figure 3.6). A laser source is used to illuminate the sample in the sample cell. Most of the light passes through the sample but some of it is also scattered (depending on the concentration of the sample, this scattering could have smaller or larger intensity) in all angles. An attenuator is used to keep the intensity of the scattered light within the desired range. It can increase or decrease the intensity of the laser by allowing less or more light to pass through the sample depending upon the concentration of the sample. A detector at 173º is used to measure the intensity of the scattered light.

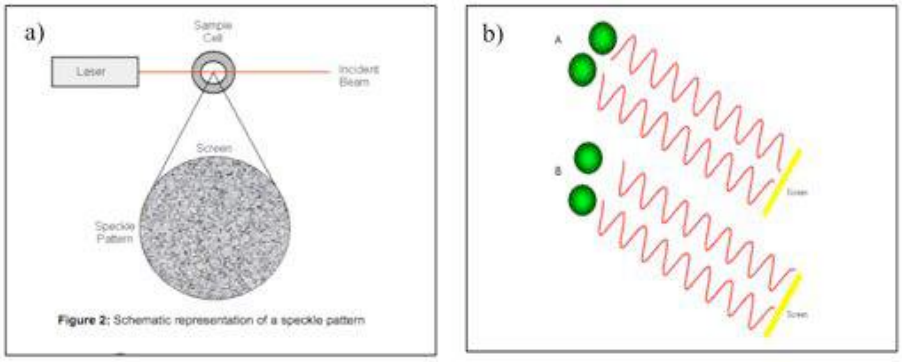

Figure 3.5. (a) Schematic representation of a speckle pattern. The speckle pattern has intensity (greyscale) spaces or pixels. The dark spaces occur when the scattered light constitutes destructive interference, and the white in case of constructive interference. In case of particles moving with Brownian motion the speckle pattern will fluctuate. (b) constructive and destructive interference patterns form particles moving with Brownian motion. In example A, two beams cancel out.While in B they interfere and enhance. In the previous case a decreased intensity signal is detected, while in the latter an increased intensity signal. Images adapted from ref. [104]

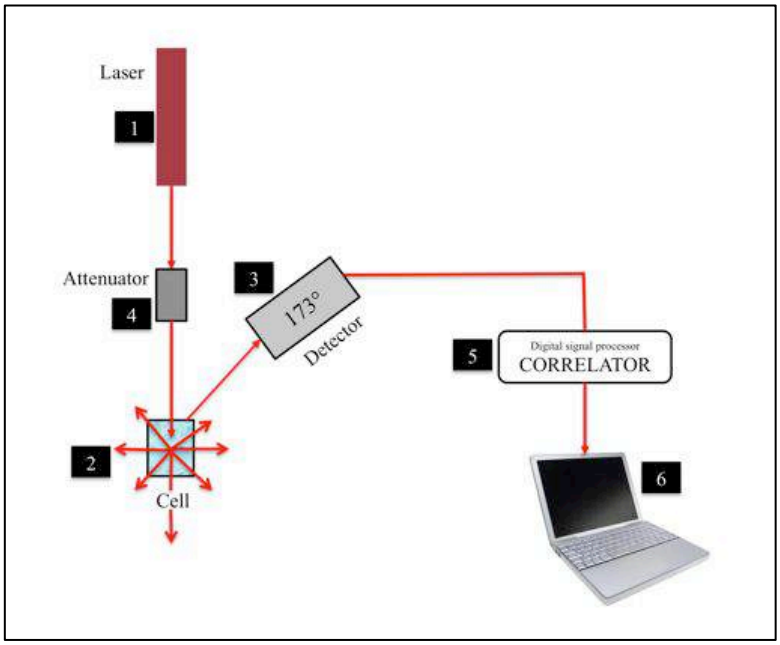

Figure 3.6. Optical configuration system setup for Dynamic Light Scattering in Zetasizer ZS Nano series (Malvern Instruments). Image adapted from ref. [104].

The signal then passes from the detector to a digital processing board called a correlator. It compares the scattering intensity at successive time intervals to derive the rate at which the intensity is varying. After the correlelator the signal is transferred to the computer where the software Nano analyze the data and measure the size etc. [104] employing the equation mentioned above.

Size deduction is performed from the correlation function, i.e. fitting time constants. The size distribution is a plot of the relative intensity of light scattered by particles in a range of different sizes and is called “intensity size distribution”. In this case there could be two scenarios. If the distribution by intensity is a single peak then it is considered to be showing the realistic view of the sample. However, if there is a tail in the peak or more than one peak in the intensity distribution, then, using the input parameter of the refractive index of the sample, the intensity distribution can be converted to volume distribution via Mie theory. This will give a clearer picture of the sample and details of the tail or second peak in the intensity distribution [104].

3.4 Zeta Potential

Zeta Potential is a physical property that any particle in a suspension would exhibit. It is a potential at the solid-liquid interfaces of particles in colloidal suspensions [105]. A charged particle in a suspension would affect the distribution of ions in the surrounding interfacial region. It results in the increased concentration of counterions close to the surface and therefore gives rise to an electrical double layer around each particle [106, 107].

One physical mechanism used to stabilize particles in an aqueous colloidal system is electrostatic repulsion. The colloidal particles carry (similar) charges to repel each other at extended distances. Ideally, these repulsive forces are strong enough to prevent the particles from close approach and so to avoid short-range interactions such as van der Waals forces that lead to aggregation. The particles usually carry specific chemical groups (covalently) bound to their surfaces. They may carry a net positive or negative charge but could also be neutral, depending on the pH of the surrounding aqueous solvent. The extent and sign of the surface charge depends also on the pK_a values of the ionizable groups bound to the surface of the particles. Zero zeta potential would mean

that the particle carries no net charge on its surface, i.e. it is neutral. This point is known as the "isoelectric point" which is very important from practical consideration. It is known to be the point where the particles are least stable and strongly tend to aggregate if only electrostatic mechanisms operate.

The zeta potential is also known as electro kinetic potential because actually it is defined as the value of the electrical potential at the "slipping plane" of the particle (figure 3.7). The slipping plane refers to the movement of the particle in an applied electric field, i.e. electrophoresis.

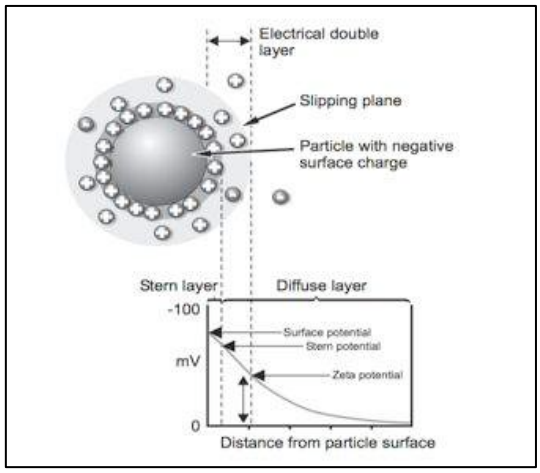

Figure 3.7. Schematic representation of the double layer and distribution of positive and negative ions around the charged colloid.

We measure the zeta potential of our samples by ZetaSizer ZS Nano (Malvern Instrument, UK). This machine calculates zeta potentials by electrophoresis with the help of sophisticated optics. It consists of six main components. A laser source, to illuminate the particles within the sample. This light source is split into an incident and reference beam. The incident beam is passed through the same cell and the scattered light at angle of 17º is detected. The Zeta Sizer ZS Nano system set up is schematically illustrated in figure 3.8.

Zeta potential is measured directly from electrophoretic mobility of the particles of sample by a technique known as "Laser Doppler Velocimetry (LDV)". It was first described by Yeh and Cummins in 1964 [108] and involves measuring the Doppler shift of the laser radiation that is scattered by the moving particles. The laser beam splits into two parts; one (the measurement beam) is focused into the sample and the second (the

reference beam) passes outside the flow. The two beams are intersected at a point via combining optics. Moving particles inside the sample will scatter light from the measurement beam with a Doppler shift; the light is collected and transferred to the detector. The reference beam is also sent to the detector where optical heterodyne detection produces an electrical signal proportional to the Doppler shift, by which the particle velocity can be determined by the following equation [109];

$$\Delta f = 2v\sin\left(\frac{\theta}{2}\right)/\lambda$$

where;

v is the particle velocity, λ is laser wavelength and θ is the scattering angle.

The speed of the particles in a suspension can be due to the Brownian motion. In case of charged particles the speed can be due to the movement of the particles in applied electric field. The average speed in the former case is negligible, i.e zero while in the latter case it not zero but slightly more than zero. The particles gain a small net velocity called drift velocity. The random motions of the particles due to diffusion also give rise to fluctuating Doppler shifts in the frequency of the light waves scattered by each particle. These random shifts are superimposed on the constant shift Δν associated with the drift velocity, ν, caused by the applied electric field.

The sample is added to a special vial with two Au electrodes at either ends to measure the electrophoretic mobility of the particles (figure 3.9). The application of applied field makes the charged particles move towards the electrodes of the opposite charges. An applied field of 150 V is applied across the roughly 50 mm length folded capillary cell. The voltage oscillates with a frequency shift of around 50 Hz to avoid net movement of particles and electrochemical reactions. As it is already explained that the electrophoretic mobility of particles is determined by LDV, the zeta potential is then calculated by using Henry's equation, i.e.

$$U_e = \frac{2\varepsilon\xi f(\kappa a)}{3\eta}$$

where;

U_e is the electrophoretic mobility, ε is the dielectric constant of the solvent, η is the

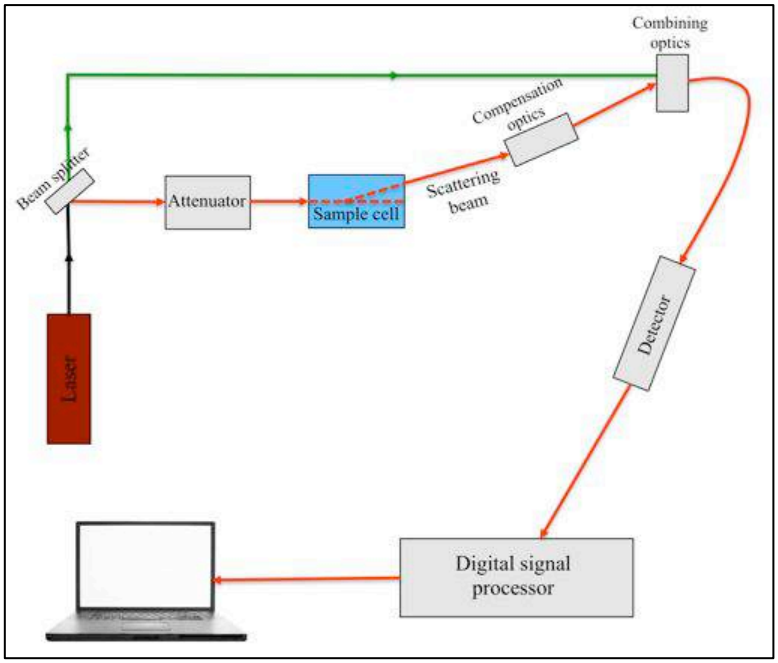

Figure 3.8. Schematic representation of Zeta Sizer (ZS Nano) zeta potential measurement set-up.

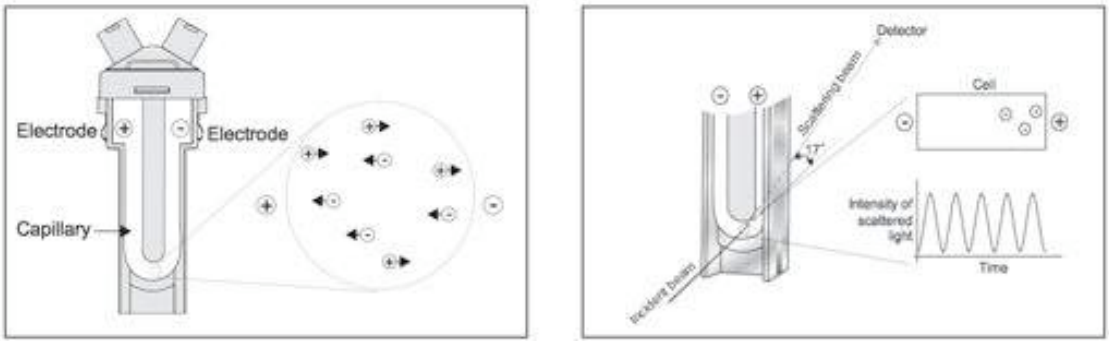

Figure 3.9. Schematic representation of Zeta Sizer (ZS Nano) zeta potential measurement. The special vial with Au electrodes is used for Laser Doppler Velocimtery to measure the electropheritc mobility of particles in a (sample) suspension.

viscosity of the solvent, $f(\kappa a)$ is the Henry function and κa is a measure of the ratio of the particle radius to the Debye length (i.e. the distance over which significant charge separation can occur).

3.5 Transmission Electron Microscopy (TEM)

The first ever TEM was constructed in 1931 by Max Knoll and Ernst Ruska. Ernst Ruska was awarded the Nobel prize in 1986 for his work in electron optics. In just a span of two more years the same group of scientists modified it and built a TEM with three lenses producing a magnification of 12,000X jumping over the optical microscopy magnification limits. The real development of TEM came in the beginning of World War II in Germany and Japan [110, 111].

Nowadays TEM is the one of the most important techniques for resolving the shape, structure and crystallinity of nanomaterials including cells. Generally, in a TEM a high speed electron beam is used to hit a thin sample. The electrons pass through the thin sample and are captured by a screen or by a CCD camera [41]. The setup is similar to a transmission optical microscope but in this case electrons are used rather than photons [110]. A typical TEM is shown in figure 3.10. Figure 3.11 shows signals generated by a high-energy beam of electrons in an electron microscope.

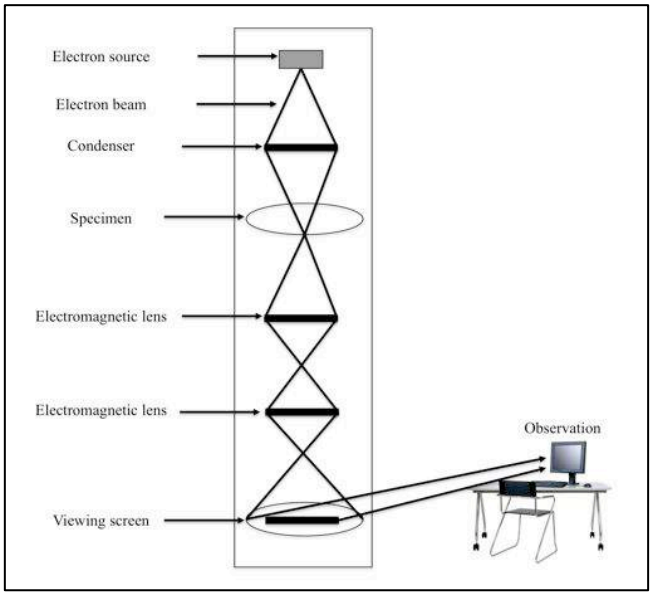

Figure 3.10. Schematic representation of a typical TEM.

,

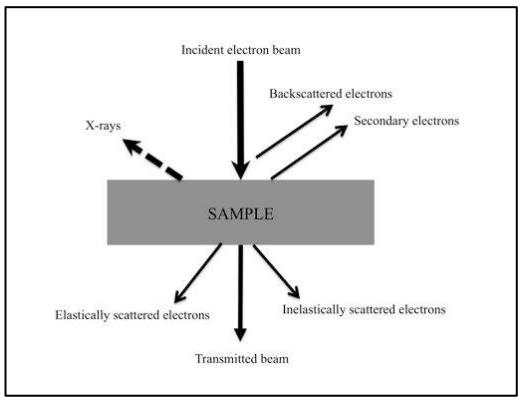

Figure 3.11. Schematic representation of signals generated when a high-energy beam of electrons interacts with a thin specimen. All of these signals can be detected in TEM.

TEMs are most commonly operated in Bright-Field (BF) imaging mode. In BF mode the transmitted beam contributes to the image and the contrast of the image arises from the occlusion and absorption of electrons in the sample. Another mode of operation is imaging in Dark Field (DF). In DF, the objective aperture is horizontally displaced so that it admits diffracted electrons. Strongly diffracted regions will appear bright relative to their surroundings and result in a DF image because any part of the field of view that contains no specimen would be dark [113]. Generally, DF mode is used for low-resolution purposes or for heavier elements in the sample and BF is high-resolution imaging [112].

The TEMs used in this thesis (JEOL, JEM-2100F and Titan, FEI) have electron guns that work on the principle of field emission. It is also known as cold cathode emitter. It provides a beam with very few deviations in electron energy via application of high electric current to a finely pointed tip [114].

TEM has been used equally in life sciences, e.g. for examining tissues and/or cells of plants, animals, prokaryotic/eukaryotic microorganisms and viruses [113].

3.6 Scanning Electron Microscopy (SEM)

TEM has a general disadvantage that it always needs very thin samples, and if they are not thin enough, electrons are strongly scattered or even absorbed rather than transmitted. Scientists exploited this constraint for developing Scanning Electron Microscopes (SEM) (figure 3.12) that are capable of characterization of relatively thick/bulky samples. Electrons are reflected (or backscattered) from bulky samples, but can be also released as secondary electrons (but all “opposite” to the beam direction) when the incoming electrons supply energy to the atomic electrons in the solid sample. These electrons are released with a wide range of energies making it difficult to focus into an image by electron lenses. But alternatively an image can be produced via the scanning principle. The primary electrons are focused into an electron probe (with a small diameter), which is scanned across the sample. Electrostatic and/or magnetic fields, applied at right angles to the beam with scan coils can be used to change its direction of travel. The sample area can be scanned line-by-line to generate images of the specimen by collecting backscattered or secondary electrons from each point [113]. The SEM (Quanta 250 FEG, FEI) used in this thesis has a field emission electron gun.

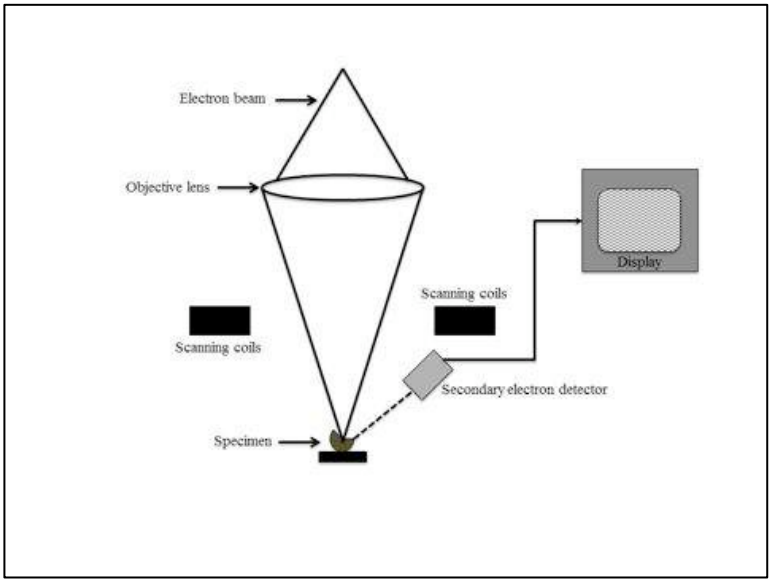

Figure 3.12. Schematic representation of a typical SEM.

SEM offers a few advantages over TEM such as it normally permits less destructive evaluation of the samples than a TEM, samples with diameters and thicknesses of

hundreds of millimeters could be characterized in SEM, and the sample preparation is much easier and faster than that for TEM [114].

3.7 Scanning Transmission Electron Microscopy (STEM)

Scanning Transmission Electron Microscopy (STEM) is an invaluable tool for characterization of structures at nanoscale with providing different imaging modes to obtain information about elemental composition and electronic structure at the ultimate sensitivity. A STEM essentially works like an SEM by scanning the sample via a focused beam of electrons and generating an image from the acquired signal. In STEM the samples are required to be thin just like in case of TEM [115], but the backscattered electrons (in beam direction) are used for generating an image with higher spatial resolution than in SEM. The electrons that emerge from the opposite side of the specimen are recorded. In STEM the beam is dynamic and it scans the sample line-by-line. The transmitted electrons are captured by a detector and produce an image. A bright field detector keeps the transmitted beam and shows holes as bright while a dark field detector discards the transmitted beam and the holes appear dark [115]. A general STEM is shown in the figure 3.13.

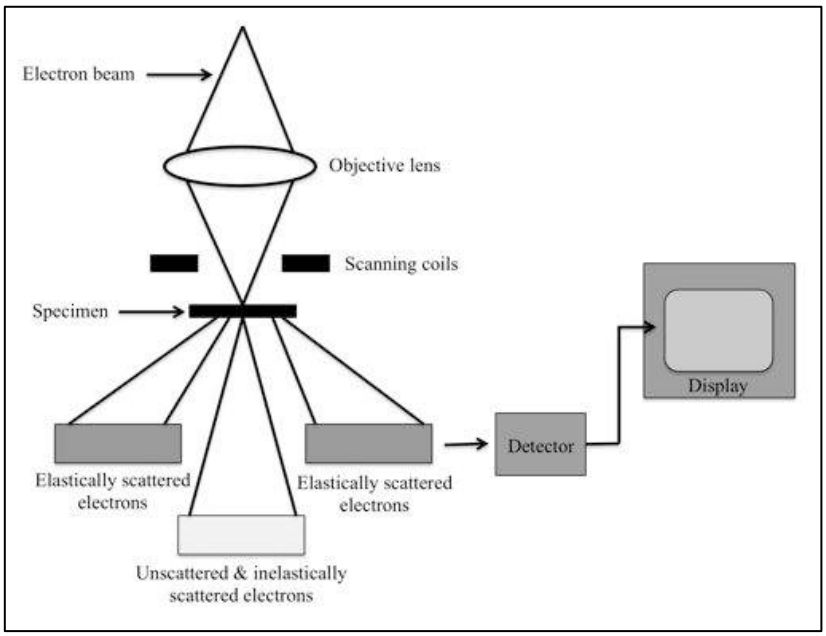

Figure 3.13. Schematic representation of a typical STEM [51].

3.8 Energy-Dispersive X-Ray Spectroscopy (EDX)

If the microscope (SEM or TEM or STEM) is equipped with the capability, EDX analysis of the samples could also be performed (as in our case all our microscopes are capable of EDX). EDX is a method that is used to determine the energy spectrum of the x-ray radiation which is produced when the electron beam hits the sample. It is commonly performed to do elemental analysis of the sample in electron microscopy. The emitted x-rays are passed to the detector where they are assigned to a particular element of the periodic table. The incident beam excites an electron of the sample in an inner shell and will eject it from its shell generating a hole. An electron from another shell with higher energy state comes to fill the hole created by the ejected electron. The energy difference between the higher and lower energy shell would be released in the form of an x-ray. The wavelength of the energy of the released x-rays can be measured and therefore the identity of the atoms of the specimen can be analyzed. This is how elemental assignments are obtained [116].

A practical disadvantage of the EDX analysis is the fact the electron beam penetrates deeply into the sample and x-rays escape from all sampling depths, therefore the elemental analysis is obtained from a large volume, rather than a particular spot on a particle. An important point to note before doing EDX is to find out about the exact nature of the detector, stage and substrate as they will also appear in the EDX spectra and this knowledge is important for correct analysis of the sample composition.

Chapter 4

EXPERIMENTAL METHODS

All solutions and dilutions were prepared using ultra pure water purified with a Millipore Gradient A10 upto 18 MΩcm (total organic content <5 ppb). The term of "water" refers to (this) ultra pure water in this thesis. Similarly all glassware was cleaned by emersion in nochromix (Sigma) (oxidizer in 96% sulfuric acid) for at least 24 h to remove organic contaminants, followed by rinsing with water.

4.1 Preparation of Tobacco Mosaic Virus Particles

TMV particles were purified from systemically infected tobacco plants (*Nicotiana tabacum* cv Samsun nn) (by our partners at Stuttgart University) as described in [117]. For isolation the leaves were chopped with cold EDTA solution (0.1 M) at pH 8 and later on were filtered. The filtrate was centrifuged at 5300 g for 15 minutes to sediment the particles. The supernatant was harvested and filtered through a 1 cm thick celite layer to remove the phenolic components and plant dyes from the suspension. The suspension was then incubated at 50 °C for 1.5 h to denature the dissolved proteins (TMV particles withstand this temperature and remain stable). Another centrifugation step was performed at 5300 g for 15 minutes to remove the denatured proteins. The supernatant was spun at 11700 g for 1.5 h at 4 °C. TMV particles sedimented and were collected from the pellet and resuspended in sodium potassium phosphate buffer while the supernatant was discarded. An additional centrifugation step at 4800 g for 10 minutes was performed to remove the undissolved material after homogenization and the pellet was discarded. The supernatant contained single particles, shortened and destroyed TMV particles as well as aggregates. They were purified by a CsCl density gradient method. The density of the suspension was adjusted by adding CsCl. The suspension was spun at 100000 g overnight. A milky disc containing the TMV particles could be removed from the tubes. The virion concentration was determined by UV spectrophotometry and by

SDS-polyacrylamide gel electrophoresis, according to standard procedures. Aliquots containing 10, 20, 30, 45, or 90 μg TMV in sodium potassium phosphate buffer (10 mM, pH 7.2) were dialyzed against H_2O using Slide-a-Lyzer MINI dialysis units (Pierce) for 2 h at room temperature. Subsequently, the suspensions were frozen in liquid nitrogen and stored at 4 °C.

4.2 Chemicals

All chemical (reagents) were p.a. or better grade. Sodium tetrachloropalladate (Na_2PdCl_4), dimethlyamine borane (DMAB) [$(CH_3)_2NHBH_3$], Igepal CO-520 or polyoxythylene-(5)-nonylphenylether [$(C_2H_4O)_n{\cdot}C_{15}H_{24}O$], ammonium iron(II) sulfate hexahydrate [$(NH_4)_2Fe(SO_4)_2.6H_2O$], iron chloride ($FeCl_3$), cetyltrimethylammonium bromide (CTAB) [$CH_3(CH_2)_{15}N(CH_3)_3Br$], ascorbic acid ($C_6H_8O_6$), gold chloride trihydrate ($HAuCl_4.3H_2O$), citric acid ($C_6H_8O_7$), Cisplatin (a.k.a. cis-diammineplatinum(II) dichloride) [$PtCl_2(NH_3)_2$], and nochromix were purchased from SIGMA; sodium chloride (NaCl), sodium hydroxide (NaOH), nickel acetate [$Ni(CH_3COO)_24H_2O$), lactic acid ($C_3H_6O_3$), and hydrochloric acid (HCl) from PANREAC; Rhodafac Re/610-E or nonyl phenoxy(polyethyleneoxy)ethanol from Rhodia; Au-sol from Aurion (Netherlands) and oxaliplatin ($C_8H_{14}N_2O_4Pt$) from TCI, Belgium.

4.3 Substrates

All SEM imaging and magnetometry analysis was performed on Si wafers (unless stated otherwise). The Si wafers (111 orientation, thickness 0.525 mm, doped with Boron, resistivity 0.002-0.004 Ωcm) (Wacker Siltronic, AG) were cut in 4x4 mm size by a wafer dicing saw (Disco DAD321). These Si:B wafers were sonicated in an ultrasonicator (VWR Ultrasonic Cleaner) for 15 minutes each in acetone, isopropanol and water. The cleaned wafers were then dried in a nitrogen stream and treated with an ambient pressure air plasma, Plasma Pen (PVA TePla), for making them hydrophilic.

All TEM and STEM imaging was performed on Carbon film 400 Mesh Copper grids (S160-4) (Agar Scientific). The grids were treated with the Plasma Pen for a few

seconds and then 5 µL of the sample volume was applied. The grids were left to dry in air for 1-2 h. The dried grids were finally treated in a vacuum chamber (LabLine, Thermo Scientific) at 4 kPa for 45-60 minutes before installing it into an electron microscope for imaging.

4.4 Imaging and EDX Spectroscopy

All SEM imaging was performed on dried droplets of the samples on a clean Si wafer in Quanta 250 FEG, FEI at 2-5 kV under high vacuum mode. Similarly STEM and TEM imaging was done by drop casting the samples on the carbon coated Cu grid in Helios NanoLab Dual Beam^{TM}, FEI at 30 kV and JEOL, JEM-2100F (Japan) at 200 kV. EDX spectra were also obtained during the imaging in the above stated microscopes.

4.5 Nickel Deposition on TMV surface

Wild type TMV suspension (10 mg/mL) in 10 mM Na-K buffer solution was obtained from University of Stuttgart, Germany. TMV suspension was serially diluted to 0.10 mg/mL. The concentration of TMV particles was determined by UV-Vis spectroscopy (Jasco V-630_{BIO} Spectrophotometer) of 1mL TMV suspension in a quartz cuvette. The measurement was perfomed for absorbance from 240 to 340 nm wavelength. The diluted TMV suspension was then partially dialyzed against water in Slide-A-Lyzer® mini dialysis units 10,000 MWCO (Thermo Scientific) for 15 minutes, in two sessions of 7.5 minutes each, with water replacement for the second dialysis. To find out about any loss of TMV particles via dialysis, UV-Vis spectroscopy of the partially dialyzed TMV particles was again performed.

4.5.1 Activation of TMV Particles with Palladium Ions

The TMV particles were sensitized (activated) with Palladium (Pd^{2+}) ions for electroless deposition (ELD) of Nickel (Ni). A suspension of partially dialyzed TMV (0.10 mg/ml, 50 µL) was mixed with an equal volume of freshly prepared sodium tetrachloropalladate (Na_2PdCl_4) (0.7 mM) in 0.5 M sodium chloride (NaCl) at pH 5.5 (by addition of 0.1 M HCl). The mixture was incubated at 25 °C for 10-15 minutes. The surplus (unbound) Pd^{2+} ions were removed by dialysis against water in Slide-A-

Lyzer® mini dialysis units 10,000 MWCO for 1 h. The dialysis was divided into three sessions of 20 minutes each, with replacement of fresh water at the beginning of every dialysis session.

4.5.2 Metallization of Activated TMV Particles

The activated TMV particles (50 μL) were mixed with an equal volume of freshly prepared Ni bath. Ni bath contained nickel acetate [$Ni(CH_3COO)_2 \cdot 4H_2O$](180 mM), lactic acid ($C_3H_6O_3$) (230 mM) and dimethylamine borane [$(CH_3)_2NH \cdot BH_3$] (35 mM). The pH of Ni bath was adjusted to 7.0 by adding 0.1 M NaOH solution and confirmed by a pH meter (827 pH Lab, Metrohm) specifically designed for microliter range pH measurement.

Metallization of activated TMV particles was also performed with the addition of surfactants in the Ni bath. Metallization bath contained either 4.75% Re610-E surfactant with an attempt to restrict Ni metallization to the TMV ends only. 10 μM or 10 mM Igepal CO-520 in the Ni bath was used to test for a continuous Ni coating on TMV surface.

Metallization reaction started as soon as activated TMV particles were mixed with Ni bath and a blackening of the solution was observed in seconds. Aliquots were taken for Scanning Electron Microscopy and magnetic characterization at various time periods ranging from 1 minute to 20 minutes. The aliquots taken from Ni bath were purified in Amicon Ultra Centrifugal Units 0.5 mL 100 K (Millipore) to remove salts and unreacted materials and rinsed twice in water.

Aliquots were taken in the form of small droplets of 0.5-1.5 μL and placed on Si wafers. The wafers had been cleaned by two times sequential rinsing in acetone, isopropanol and water. The wafers were dried using a nitrogen gun and later on treated with a plasma pen before adding the droplets. The droplets of metallized TMV were placed carefully in the middle of the wafer and left to dry for 1-2 h. After drying they were rinsed with a droplet of water to remove any salts still left. The samples were then imaged in an SEM (RAITH 150^{TWO}) and magnetically characterized in a MPMS SQUID-VSM (Quantum Design).

4.5.3 Dynamic Light Scattering of TMV Particles

Dynamic Light Scattering (see section 3.3, *"Dynamic Light Scattering"* in chapter 3) of TMV particles was detected with a Zeta Sizer ZS Nano (Malvern Instruments). The TMV particles were measured for their diameter and dispersity before activation with Palladium ions, after activation with Palladium ions and finally during metallization.
A TMV suspension of 40 µL was poured into a clean cuvette specially designed for Zeta Sizer ZS Nano under the standard measurement conditions. DLS was used for wild type TMV particles, activated TMV particles (that were dialyzed after activation) and finally during metallization (to obtain a real-time analysis) of the ELD reaction.

4.5.4 Magnetic Characterization in SQUID-VSM

The magnetic behaviour of metallized TMV particles was characterized in a Magnetic Properties Measurement System (MPMS) Superconducting Quantum Interference Device-Vibrating Sample Magnetometer (SQUID-VSM) (Quantum Design) at 300K. The wafer containing a dried sample of metallized TMV was immobilized with diamagnetic glue (Duco Cement, ITW Performance Polymers, USA) to the MPMS SQUID-VSM quartz sample holder. The sample requires careful centering, depending on its shape and size. Usually, it was attempted to locate the center of the sample at 66 mm on the mounting station scale. The holder was then joined to the long sample probestick to lower it into the tool. However, correct measurement requires finer centering. If a sample has a magnetic moment above $\approx 10^{-7}$ emu, the detection coils can detect the magnetic moment and center it automatically. In case of weakly magnetic samples it is advised to apply a small field (100-500 Oe), and then start the automatic centering. For extremely weakly magnetic samples, manual centering can also be performed by adjusting the distance to 63-69 mm, which depends on location, size and shape of the sample. For manual centering it is very important to confirm the location of the sample and on the probestick, and to use manual entering in the software of SQUID-VSM.

4.6 Mineralization of TMV

Wild type TMV stored in Na-K buffer were extensively dialyzed for the removal of salts against water in Slide-A-Lyzer® mini dialysis units for 1 h with water change after 30 minutes.

4.6.1 TMV Mineralization with Iron Oxide

TMV was coated as in [21] with some modifications. 25 μL of 1 mM ammonium iron(II) sulfate hexahydrate [$(NH_4)_2Fe(SO_4)_2.6H_2O$] were mixed with an equal volume of 2 mM iron chloride ($FeCl_3$). The mixed solution was then added to an equal volume of dialyzed TMV suspension (0.05 mg/mL) and was incubated at room temperature for 2-3 minutes. The pH of this solution was measured with a pH meter (Metrohm). To this acidic solution 0.1 M NaOH was added slowly drop-by-drop with proper mixing by sucking up a part of the suspension with a pipette and then releasing it while the pipette tip is still in the suspension, and repeated 4-5 times. The pH was measured after every NaOH addition. The basic solution was being added until the pH reached 9.0 and precipitates appeared in the solution. At this point no more NaOH was added.

The mineralized TMV was purified (to remove unreacted salts) in Amicon Ultra Centrifugal Units at 14,000 g (Eppendorf 5417-C) for 20 minutes. It was rinsed with 500 μL water twice. Finally the purified mineralized TMV particles were recovered from the centrifugal filter units by placing the filter units in inverted position into a clean 2.0 mL Millipore tube and centrifuging at 5,000 g for 5 minutes.

4.6.2 X-Ray Diffraction of Mineralized TMV Particles

Mineralized TMV particles were synthesized (as 4.6.1) with a relatively high concentration of TMV (i.e. 0.5 mg/ml – 1.0 mg/ml) for XRD analysis. The TMV iron oxide particles were dried on a clean glass slide and scraped off onto a zero background Silicon holder. The phases were identified by XRD in an x-ray diffractometer (X'Pert, PANlytic, Netherlands) with CuKα radiation (45 kV, 40 mA) and soller slit 0.04 radians in reflection mode.

4.6.3 SEM Imaging and EDX Spectroscopy

A small droplet (0.5 uL) of the mineralized TMV was placed in the centre of a clean Si:B wafer and dried in air. It was then imaged by SEM (Quanta 250 FEG, FEI) at 2-5 kV in High Vacuum. Energy Dispersive X-Ray (EDX) spectrocopy spectra were obtained for a network of a number of mineralized TMV particles as well as for individual TMV iron oxide tubes ("EDX Spot Test").

4.6.4 Magnetic Characterization of TMV Iron Oxide Particles

Sample preparation for TMV iron oxide particles for magnetic characterization was similar to that for SEM imaging. A droplet of 3-10 uL was placed on a clean Si wafer and dried in air. It was made sure to use only Si wafers that were doped with Boron (Si:B) for magnetic analysis, they were cut to 4x4 mm so that they can fit in our SQUID-VSM (Quantum Design).

In order to normalize the magnetic moment of the sample, Si:B wafers were weighed in a highly sensitive physical balance (XS105 Dual Range, Mettler Toledo) after cleaning. They were reweighed after the added sample was totally dried, the difference being the mass of the TMV iron oxide particles.

Typical M-vs-H analysis was performed for TMV iron oxide particles at 300 K and 5 K.

We also measured TMV iron oxide particles for the magnetic behaviour in suspensions. Briefly, a clean (diamagnetic) plastic container was filled with TMV iron oxide nanoparticle suspension, sealed with the diamagnetic glue and closed with a (paraffin) parafilm to avoid leakage during the vibratory movements of the VSM.

4.6.5 Annealing of (Amorphous) Iron Oxide Nanoparticles

TMV iron oxide particles were heated to attempt phase transformation from amorphous to crystalline. The samples were synthesized in exactly the same way as already described in 4.6.1 and heated in air or nitrogen.

TMV iron oxide particles were air dried on a clean glass slide. The glass slide was placed in an electric oven (Hereaus, Thermo Scientific), and the sample was heated at 250 °C in air for 3 h. Similarly, iron oxide nanoparticles were heated in vacuum with continuous nitrogen flowing an oven (UniTemp GmbH). For SEM, the samples were

diluted (1:1000), and deposited on a clean Si wafer, air dried, heat treated in the same way and imaged at 2-5 kV.

For magnetometry, a precleaned and weighed 4x4 mm Si wafer was loaded with 3-5 μL of mineralized TMV suspension, air dried and thermally treated like the other samples, and subsequently characterized for their magnetic behaviour by SQUID-VSM.

For XRD the heated iron oxide nanoparticles were scraped off the glass slide on the zero background Si sample holder of the x-ray diffractometer, as discussed for samples that were not heated (section 4.6.2).

4.6.6 XANES (X-Ray Absorption Near Edge Spectroscopy)

XANES measurements at the Fe K-edge were performed at 300 K at the BM25 Spanish CRG Beamline (SpLine) of the ESRF (European Synchrotron Radiation Facility). A gas ionization chamber, filled with nitrogen and argon, was used to measure the incident beam intensity. The sample, deposited on a silicon substrate as detailed above, was placed in the beam path at 45º incidence. X-ray absorption was detected in fluorescence mode, measuring the emitted photons following X-ray absorption, using a 13 elements detector. Bulk metallic Fe, FeO, α-Fe_2O_3, γ-Fe_2O_3 and Fe_3O_4 powders were also measured for comparison, but in transmission mode. As the sample amount available was very small, sample spectra are free of self-absorption effects, while the larger mass of the reference substances would modify the spectral profile in fluorescence. The proper procedure is thus to compare reference transmission spectra with the sample fluorescence spectrum.

4.7 Gold (Au) Deposition on TMV

Commercial Au sol nanoparticles of 6nm diameter with citrate surface stabilization were used for Au deposition on TMV. The Au-sol was purchased from Aurion, Wageningen, Netherlands. It is practically free of salts and the particles are coated with citrate.

4.7.1 Au-TMV-Au Dumbbells

Au-TMV-Au dumbbells were synthesized as described in [9]. Briefly, 95 μL of Au-sol (Aurion Wageningen, NL) was mixed with 0.5 μL of TMV suspension (0.05 mg/mL). It was incubated overnight. The solution was then dialyzed using Slide-A-Lyzer® mini dialysis to remove the surplus/unbound Au nanoparticles for 1.5 h against water. Fresh water was added (and the already used was discarded) after every 30 minutes.

4.7.2 Selective Enhancement of Au-TMV-Au Dumbbells at TMV Ends

TMV with attached Au nanoparticles at both ends were selectively grown via electroless deposition with the aim to block the channel.

The TMV-Au-TMV dumbbells were treated with an electroless deposition bath containing 30 μL (0.06 M) of cetyltrimethylammonium bromide (CTAB), 40 μL (0.25 mM) gold chloride trihydrate ($HAuCl_4 \cdot 3H_2O$) and 2 μL (0.1 M) ascorbic acid ($C_6H_8O_6$). The pH of the ELD bath was adjusted to 4.0 with 0.05 M NaOH solution.

Samples were taken after 30, 45 and 60 minutes. 1.0 μL of the selectively enhanced Au-TMV-Au particles were placed in the middle of a clean Si wafer and dried in air. The dried Si wafers were then imaged by SEM.

4.7.3 Decoration of TMV with Au nanoparticles

Au TMV nanorods were synthesized from a concentrated solution of citric acid mixed with a TMV suspension and Au sol.

75 μL of Au-sol (6 nm, Aurion) was mixed with 25 μL of citric acid (0.025 M). 5 μL of dialyzed TMV suspension (0.05 mg/mL) was added to the premixed solution of gold nanoparticles and citric acid. The pH of this mix was measured to be 2.6-2.8 It was mixed thoroughly via vortexing for a few seconds and incubated overnight.

The overnight-incubated mixture was vortexed for a few seconds, and dialyzed against water with a Slide-A-Lyzer® mini dialysis unit.

4.7.4 Citrate Replacement by 2-MEA (2-Mercaptoethanol) of Citrate Coated Au Nanoparticles

The 6 nm Au nanoparticles surface stabilizing agent citrate was exchanged by 2-MEA as per [118] with some modifications . Briefly, Au-sol was mixed with 14.3 mM 2-MEA in 1:1000 ratio and incubated for 6 hours on a shaker at 175 rpm. It was purified by centrifuging in an Amicon Ultra Centrifugal Units (100,000 MWCO) at 5,000 g (Eppendorf 5417-C) for 5 minutes. The pellet was resuspended in water twice and respun at the same speed.

4.7.5 Zeta Potential

Zeta potential (see section 3.4, *"Zeta Potential"* in chapter 3) of the suspensions was determined by electrophoresis by adding 1 mL of suspension into polystyrene disposable capillary cell with two gold electrodes in a zetasizer (ZS Nano, Malvern, UK).

4.8 TMV Drug Encapsulation

TMV drug encapsulation was performed with cisplatin and oxaliplatin.

a. CISPLATIN

4.8.1 Cisplatin Encapsulation in TMV Central Channel

95 µL of concentrated solution (1mg/mL) of cis-diammineplatinum(II) dichloride (commonly known as cisplatin) was prepared in ultra pure water. A dialyzed suspension of TMV of 5 µL (0.1 mg/ml) was added to 95 µL of cisplatin solution. The drug encapsulation was performed at a number of different pH values, i.e. pH 4.0, 5.0, 6.0, 7.0, 7.5, 8.0 and 8.5. The pH of cisplatin solutions was adjusted using NaOH or HCl. The TMV suspension was incubated overnight with cisplatin solution in the absence of light at room temperature.

After the incubation, TMV particles were dialyzed against water for a range of time periods, i.e. 2, 5, 10, 15, 20, 30, 45 and 60 minutes.

4.8.2 TMV Cisplatin Encapsulation with Au Capping at the Ends

In these experiments TMV was first treated for drug encapsulation in the 4 nm channel and then capped at its ends using Au nanoparticles of 6 nm. The experimental set up was the same as it would be a combination for Au-TMV-Au synthesis and TMV cisplatin encapsulation (with slight modifications). Briefly, 5 μL of TMV (0.1 mg/ml) was incubated with 95 μL of cisplatin (1 mg/ml) at pH 7.0 in the dark. After 24 h, 25 μL of Au-sol was added and vortexed for a few seconds. Finally the drug-TMV- Au-sol mixture was incubated in the dark for 24 h.

After incubation, the sample was dialyzed against water for 1 h in two sessions of 30 minutes each. The water was replaced in between the two sessions.

4.8.3 TMV Cisplatin Encapsulation with Decoration via Au Nanoparticles

TMV cisplatin encapsulation was also attempted with Au decoration. The synthesis was performed that TMV particles were encapsulated with drug first and then Au decoration was attempted, i.e. 5 μL (0.1 mg/ml) of dialyzed TMV suspension was added to 95 μL of Cisplatin solution (0.5 mg/ml) at pH 7.0. It was allowed to incubate overnight. After appropriate incubation the sample was dialyzed against water for 1 h in two sessions of 30 minutes each. To the purified sample was then added 50 μL of Au-sol and 25 μL of citric acid (0.1 M). This mixture was allowed to incubate at room temperature for 24 h. It was purified via Amicon Ultra Centrifugal Units.

B. OXALIPLATIN

4.8.4 Oxaliplatin Encapsulation

95 μL of concentrated solution of oxaliplatin (2 mg/ml, 5 mM) was mixed with 5 μL TMV suspension (0.5 mg/ml) at pH 7.0 and incubated overnight. After proper incubation TMV particles were dialyzed in Silde-A-Lyzer mini dialysis units against water for 1 h.

4.8.5 Oxaliplatin Encapsulation with Modified TMV (Lys Mutant) Particles

TMV particles were modified covalently by binding PEG linkers to the TMV with the mutation Thr158Lys [119]. These TMV particles were encapsulated with oxaliplatin. 50 µL of oxaliplatin (2 mg/ml, 2.5 mM) were incubated overnight with 50 µL of modified TMV particles (0.1 mg/ml).

The oxaliplatin-(modified) TMV particles were dialyzed for 1h against water in Slide-A-Lyzer mini dialysis units in two sessions of 30 minutes each. The water was replaced after 30 minutes.

4.8.6 Cisplatin and Oxaliplatin Effusion

The drug encapsulated TMV were used in these experiments. 100 µL of TMV encapsulated drug were dialyzed against 1mL of water for 10, 30 and 60 minutes and 6 h. The water was changed after every 30 minutes.

CHAPTER 5

RESULTS & DISCUSSION

5.1 Nickel Deposition on TMV

TMV is an excellent biological scaffold for a number of fabrication techniques. In this chapter we show that TMV can be used for metallic deposition on the exterior protein surface. Nickel metal has been deposited on the exterior of the TMV protein tube because Ni is ferromagnetic at room temperature. The aim was the metallization of TMV rods as a whole and only at the ends. The metallized viral tubes would be able to induce hyperthermia via the (ferromagnetic) Ni nanoparticles [120, 121] attached to the TMV by applying an external alternating magnetic field. Alternatively, such a nanotube could be a drug container that can be moved by a magnetic field gradient towards a tumor. Ni deposition was performed in the presence or absence of surfactants to restrict the metallization on the whole TMV or only at the ends.

5.1.1 Activation of TMV with Palladium ions

Electroless deposition requires a sensitization (also known as activation) of the TMV (since it is rather a non-metallic protein rod/tube) surface by noble metal clusters or particles because they are active catalysts in a redox reaction between the reductant and a metal ion to be deposited. The noble metal is quickly encapsulated in the deposited metal, which is also a good catalyst for the reaction. Thus, wherever a noble metal or a deposited metal cluster is present, it can grow from nanometers to micrometers in size and eventually coalesce with the neighbouring particles to form a closed layer.

Undialysed TMV particles (containing buffer) were used for activation with Pd^{2+} ions because deposition of Ni was aimed on the exterior of TMV. It has been already reported that in case of dialyzed TMV particles the Ni metal deposition confines to the inner channel of TMV [6]. TMV particles were incubated with a solution of Na_2PdCl_4 for 15 minutes to activate them with Pd^{2+} ions at pH 5.5. An acidic pH is

preferred for the activation of TMV particles to avoid huge clusters of Pd (due to palladate hydrolysis). At low pH values these polyoxo-hydroxo-palladate nodules do not form. The presence of Cl^- ions also helps to avoid this. It is why the activation solution was prepared in 0.5 M NaCl [6, 122].

At acidic pH value the external protein surface of TMV is (slightly) positively charged while the $[PdCl_4]^{2-}$ complex is negatively charged. Therefore, Pd ions can bind to the protein surface. The channel at this pH is predominantly negatively charged and thus Pd ions would not bind in there [6]. This binding of the metallic ions to the virion particles depends otherwise upon unknown factors such as the availability of certain amino acids to $[PdCl_4]^{2-}$.

5.1.2 Electroless Deposition of Nickel on TMV

The already activated TMV particles were placed in a Ni bath. It contained a Ni salt, nickel acetate $[Ni(CH_3COO)_2 \cdot 4H_2O]$, a complexing agent, lactic acid ($C_3H_6O_3$), and a reductant, dimethylamine borane (DMAB) $[(CH_3)_2NHBH_3]$ at pH 7. The Pd ions attached to TMV exterior protein surface are reduced by the reductant DMAB. After reduction the metal atoms coalesce to clusters [123].

The Pd^0 cluster serves as nucleation centre for Ni growth. Ni metal is rapidly deposited over the Pd clusters and coalesces to spheres. A continuous Ni layer is not observed and rather isolated regions are seen with Ni spheres deposition on TMV (figure 5.1.1). It would point out to the fact that activation of TMV is not ideal and Pd ions either do not bind everywhere on the TMV or they are not stable enough and some of them detach from TMV particles. This supports the hypothesis that ELD progresses via the growth of relatively few, isolated nuclei located at Pd clusters; on the other hand, the finding demonstrates that deliberate interruption of growth can yield products with a well-defined morphology. Longer growth times quickly lead to coalescence of the growing clusters. Despite extensive efforts to optimize the parameters of the ELD process, we found in all cases that Ni layers having thicknesses in the true nanoscale range (<20 nm) were dominated by grain boundaries formed by the coalescence of neighboring Ni clusters; moreover, the metal layer thickness was always found to be inhomogeneous, apparently because the Ni clusters grow at different rates. Incorporation of the surfactant Igepal into the metallization bath resulted in complete suppression of cluster coalescence and growth of densely

spaced Ni particles; instead, isolated Ni clusters always formed (figure 5.1.2). The Ni deposition with Pd sensitization on TMV can be represented in terms of reactions as follows [124];

The adsorbed Pd ions are first reduced by DMAB [$(CH_3)_2NH_3 \cdot BH_3$] (represented as BH_3 in the following equations) to Pd zero-valent metal state, i.e.

$$H_2O + Pd^{2+}_{adsorbed} + BH_3 \rightarrow Pd^0_{adsorbed}\ BH_2(OH) + 2H^+$$

In the second reaction the Ni ions are reduced at the Pd already adsorbed to the TMV surface. Pd^0 in this case serves as a nucleation centre for the autocatalytic deposition of Ni metal.

$$3Ni^{2+} + BH_3 + 3H_2O \rightarrow 3Ni^0 + B(OH)_3 + 6H^+$$

Important anodic and cathodic reactions can be expressed as;

Anodic Reactions:

$$BH_3 + H_2O \rightarrow BH_2(OH) + 2H^+ + 2e^-$$

$$BH_2(OH) + H_2O \rightarrow BH(OH)_2 + 2H^+ + 2e^-$$

$$BH(OH)_2 + H_2O \rightarrow B(OH)_3 + 2H^+ + 2e^-$$

Cathodic Reaction:

$$Ni^{2+} + 2e^- \rightarrow Ni^0$$

During ELD bubbles evolve out of the deposition bath as a result of the synthesis of hydrogen from a side reaction.

RE610 is a surfactant that can be used as an additive in ELD baths to improve the smoothness. However, the presence of RE610 promoted the growth of clusters similar to those produced by Igepal (although densely spaced clusters were obtained in some cases, as well). An intriguing observation was the fact that the Ni clusters were usually found to grow at specific ‘‘defects’’ – namely, at the ends of virions (figure 5.1.3) and at locations where two virions meet end-to-end (virions are prone to linear or kinked aggregation). This phenomenon – in some cases also observed in the absence of RE610 (figure 5.1.4) – may be related to the formation of Au-TMV-Au ‘‘dumbbells’’ [9], prepared by mixing Au nanoparticles and TMV, followed by electroless Au deposition to produce Au particles of sufficient size to cover and attach firmly to the TMV tube openings. Ni deposition only at the ends of TMV, which had been achieved with and without the addition of the surfactant RE610 was not reproducible in any form. Thus, this process is neither precisely understood nor controlled and rather had a random occurring. Our Ni clusters were synthesized from ions rather than nanoparticles, and the main assembly step occurs during ELD. While

the Au particles attach to viral RNA exposed at the TMV end points, the mechanism of Ni cluster attachment is unclear.

Ni metal deposition was confined to the exterior protein tube rather than inside the channel. Therefore, the activation of TMV rods was performed in the presence of the phosphate buffer. The phosphate ions at pH 5.5 can bind to the positively charged exterior of the TMV (figure 5.1.5). The sensitization would yield the co-existence of the Pd^{2+} and phosphate ions attached electrostatically on the exterior of TMV rods. The complex formation of Pd^{2+} with phosphate is ruled out here because it would need temperatures as high as 230 °C. Ni^{2+} can however precipitate with the phosphate as $Ni_3(PO_4)_2.xH_2O$. This precipitate formation would presumably occur upon contact of Ni^{2+} with the phosphate-covered protein rod of TMV. The ELD process and/or the Ni deposition then requires Pd^{2+} which is reduced to metallic cluster by the reductant DMAB. The ELD process is autocatalytic and the coalescence of the growing clusters can yield the plant virus totally wrapped in a metallic sheath of Ni [6].

5.1.3 Dynamic Light Scattering

Dynamic light scattering was performed on TMV samples before and during the metallization process, and with naked TMV particles, i.e. before activation with Pd^{2+}, after activation and during the electroless deposition. The Z-average (hydrodynamic diameter) that we obtained for TMV particles is given in the table 5.1.1. The hydrodynamic radius obtained under different conditions for TMV via DLS is neither 18 nm nor 300 nm [125]. This is because of the fact that TMVs are not circular particles. The values we recorded for TMV are not exactly similar but are slightly different which could be due to measurement conditions.

It can be seen that there were no polyoxo-hydroxo-palladate nodules formed in the Pd solution because the Z-average value remains similar to that of pure TMV particles (the same is proved by intensity and correlation function measurements). The hydrodynamic radius jumps up to over micrometers during the metallization process pointing to the rapid increase in the diameter of the particles and/or severe degree of aggregation. We already know that during the metallization TMVs make huge networks. Similarly, in the intensity data we can see single prominent peaks in the pure and activated (dialyzed) TMV while during metallization the rapid increase of diameter of the particles gives rise to more than one peak and at micrometric sizes,

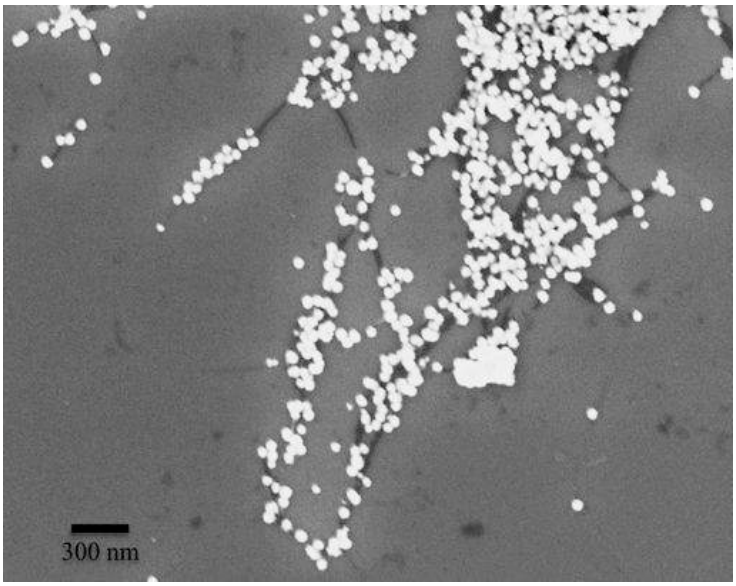

Figure 5.1.1: SEM image of Ni metal deposited (white spheres) on TMV (black rods) without any surfactant. Isolated Ni clusters were formed in the ELD in the absence of surfactant.

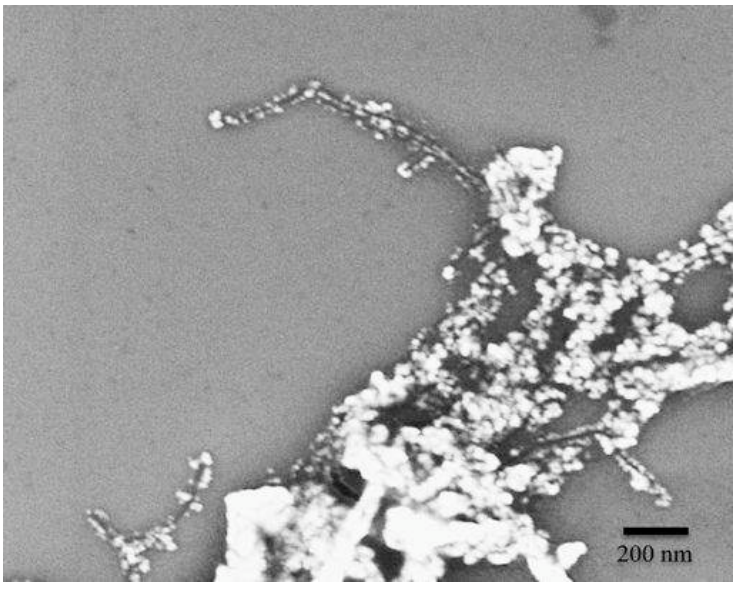

Figure 5.1.2: SEM image of Ni metal deposited (white) on TMV (black rods) with the surfactant Igepal. 10 uM Igepal in the ELD bath resulted in densely spaced particles of deposited metal on TMV [10].

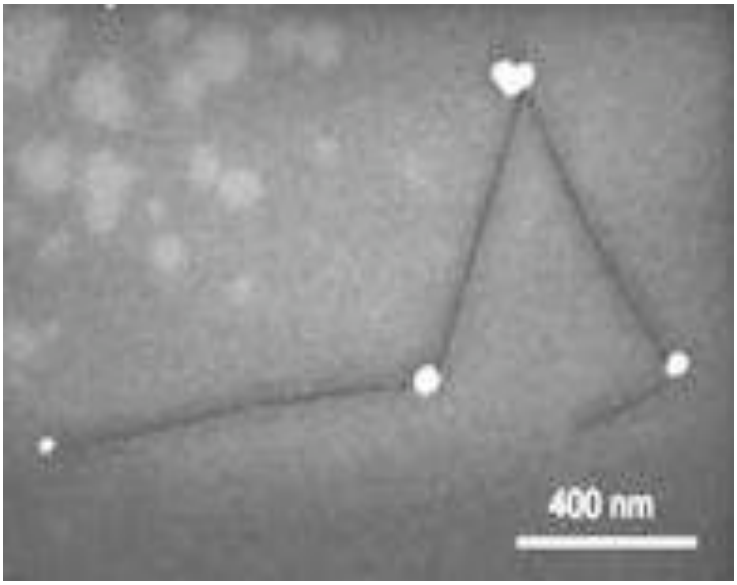

Figure 5.1.3. SEM image of TMV (black rods) with Ni metal (white spheres) deposited at the ends of TMV with the addition of a surfactant (Re 610/E) in the ELD bath [10].

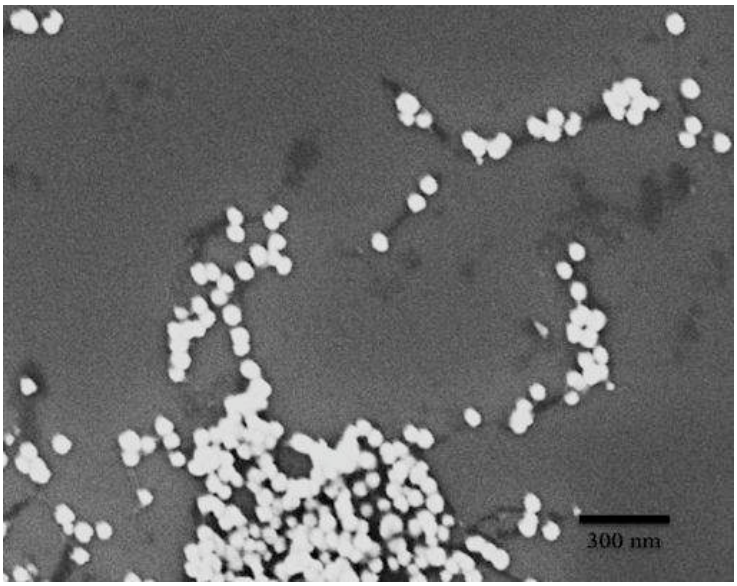

Figure 5.1.4. SEM image of TMV (black rods) with Ni metal (white spheres) deposited at the ends of TMV without the addition of any surfactant in the EDL bath.

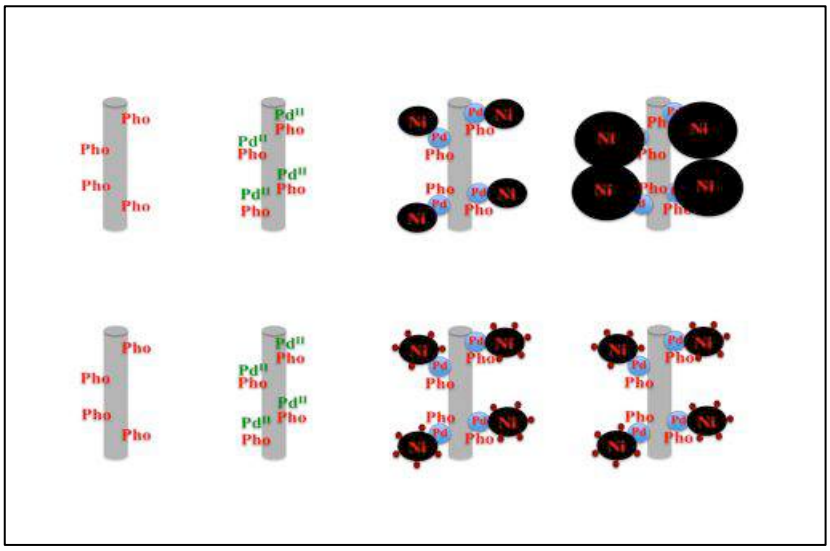

Figure 5.1.5. Electroless deposition of TMV. Upper sequence: binding phosphate followed by binding of Pd^{2+} complexes, reducing it to Pd and growing Ni on Pd, and by continuation of the growth of Ni on Ni. Lower sequence: in the presence of surfactants, growing Ni clusters are encapsulated in micelles consisting of amphiphilic surfactant molecules [10].

Samples	Z-average (d / nm)
Pure TMV	160
TMV after activation with Na_2PdCl_4 and dialysis	179
TMV during the metallization of Ni	1358

Table 5.1.1. Hydrodynamic diameter (Z-average) of TMV particles determined by DLS.

which is very different from pure and activated TMV particles (figure 5.1.6). The same picture is also given by the correlation function. The correlation function is a direct measure of the particle size. The smaller the particle the faster the signal decays and vice versa. Particles of larger sizes would make the signal decay take more time (figure 5.1.7). The correlation function for the pure and activated TMV looks similar. It means that the activation of TMV makes no difference to the diameter, or in other words the binding of Pd^{2+} ions to TMV coat proteins does not contribute significantly to increase the protein tube diameter of TMV particles (which is logical). During metallization we see the signal decay is over 100 times slower than for pure and activated TMV particles. It shows rapid increase in the diameters of the TMV particles. In other words it gives a clear picture that Ni ions are rapidly reduced over the Pd centers and they coalesce to make bigger aggregates.

5.1.4 Magnetic Behaviour of Ni Metallized TMV Particles

Since most of the Ni clusters are more than 20 nm in diameter, we expect them to be ferromagnetic at 300 K (smaller Ni clusters can be superparamagnetic; the reported superparamagnetic limit for Ni is 8 nm [129, 127]). The layer of NiO that grows on the cluster surface after removal from the reducing environment of the ELD bath could help to improve the coercivity and the remanent magnetization in comparison to the values of bulk Ni [128, 129]. Magnetometry measurements performed on these samples (figure 5.1.8) find a saturation magnetization of approximately 0.004 emu per gram of deposited solid (which contains Ni but also salts from the bath). This very low value can be accounted for by a cluster microstructure consisting of rather small Ni cores surrounded by NiO shells, which would be indicative of extensive oxidation. However, the measured coercivity of 90 Oe is similar to that of bulk Ni (100 Oe [128]), suggesting that the cores are large enough to exhibit bulk ferromagnetism. We measured a similar hysteresis loop for Ni-metallized TMV either with or without the addition of surfactant.

5.1.5 Stability of Ni Metallized TMV particles

The metallized TMV particles were let to age (in suspension) at room temperature conditions overnight and were imaged by SEM the other day for their stability. It was found out that no metallized TMVs could be seen. The Ni particles detached of the TMVs proving that fact that these structures are not stable over long time periods in solution. A droplet of the metallized TMVs dried on a Si wafer was also aged for 3 months. It was later on imaged by an SEM. The aged sample showed similar features (as fresh samples showed under SEM) and aging after drying made them stable for longer periods.

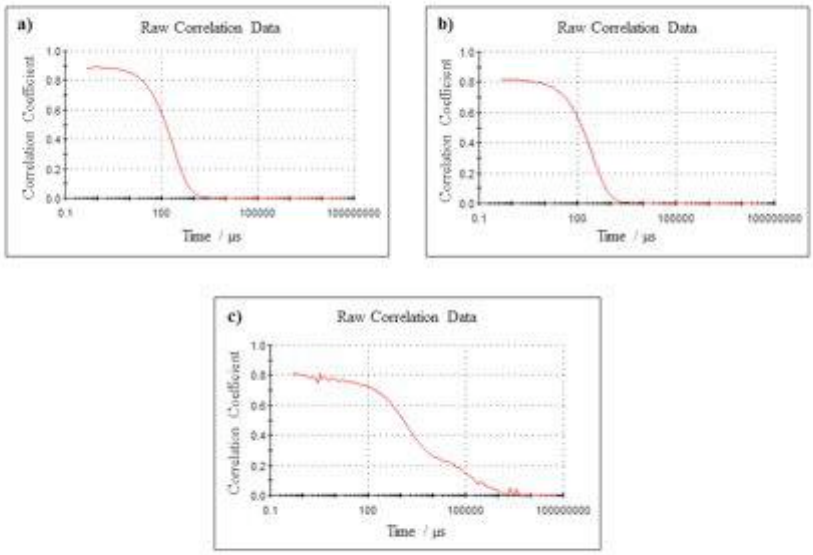

Figure 5.1.6. DLS: Correlation function measurements of DLS of TMV particles (a) before activation; (b) after activation (with Pd ions) and after dialysis; and (c) during the ELD deposition of Ni. The signal is decaying at equal time for both pure and activated TMV showing no increase in the diameter of TMV, whereas during ELD the signal decays >100 times slower than for the other two samples. It shows the rapid deposition of Ni on TMV and increase in the diameters as well as aggregation.

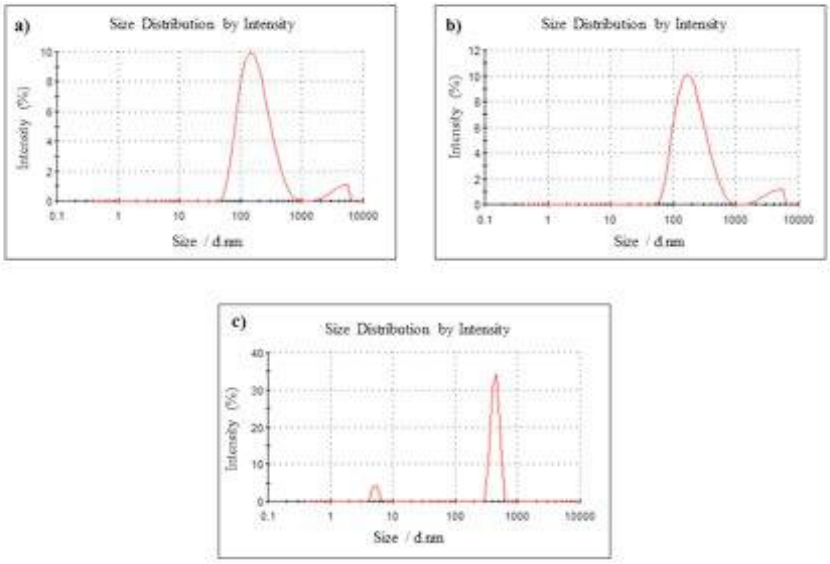

Figure 5.1.7. DLS: Size distribution of TMV particle by intensity. (a) before activation; (b) after activation (with Pd ions) and after dialysis; and (c) during the ELD of Ni. The peaks of untreated TMV particles and after activation (with Pd ions) are similar. The hydrodynamic size and the scattered intensity levels are also similar. It means that the activation with Pd ions did not change the diameter of TMV particles. But during metallization the peak is different from the previous two cases and shows a rapid increase in the size. It shows the deposition of Ni on TMV and increase in the diameters as well as aggregation.

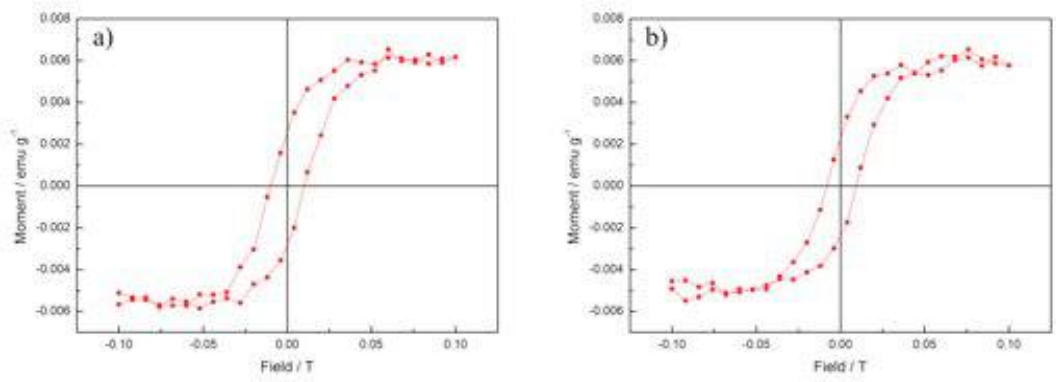

Figure 5.1.8. Magnetization as a function of applied field of metallized TMV (a) without surfactant and (b) with the addition of the surfactant (Igepal).

5.1.6 Conclusions

TMV tubes were used as biotemplates for fabricating magnetic nanoparticles through ELD of Ni externally. With the use of surfactants and metallization times, viruses with desired morphology of deposited Ni (isolated clusters and/or densely space particles) were obtained. Deposited Ni makes the viruses ferromagnetic but the magnetic moment is measured to be lower than expected. Oxidation of Ni at the surface could be a reason for this lower magnetic moment and could have generated Ni/NiO core-shell structures.

5.2 Mineralization of TMV with iron oxide

While syntheses for nanoparticles and nanorods of iron oxides are well established, nanotubes are as yet rare objects [130-136] but with interesting specific magnetic properties [10]. Nanotubes could replace the usual spherical nanoparticles in medical applications [137-139], especially in magnetic resonance imaging and therapeutic hyperthermia [140]. Iron oxides are here of utmost importance due to their unique combination of nontoxicity and magnetism (ferro-, ferri-, superparamagnetism). TMV, a tubular plant virus with only 18 nm diameter fulfills this requirement by multiple COOH, CO, and OH groups, which are suitable for binding a range of particles [5, 6, 9, 10, 141, 142], metal layers [6, 10, 143] and oxides [144, 145]. TMV is stable up to pH 8.5, and, concerning it is built only from RNA and proteins, mechanically surprisingly rigid.

We optimized the synthesis conditions to obtain a very thin, but continuous and smooth coating on TMV. The natural diameter of TMV (18 nm) determines the inner diameter of the iron oxide tube, while the outer diameter depends on the synthesis conditions. The employed 1:2 mixture of aqueous Fe(II) and Fe(III) salts is tailored to produce Fe_3O_4 (=$Fe(II)Fe(III)_2O_4$), but we do not *a priori* exclude the presence of other iron oxides, which can influence many physical properties.

5.2.1 SEM, TEM and EDX

Our synthesis and purification procedure (see section 4.6.1, *"TMV Mineralization with Iron Oxide"* in chapter 4) results in a brown suspension. Upon drying of a droplet of the suspension on a silicon wafer substrate, we acquired SEM images (figure 5.2.1). They show individual coated TMV rods with higher reflectivity (light grey) than the wafer background (dark grey), while pure TMV has a lower reflectivity (at least at low imaging voltages). The rod diameters are 25-40 nm, but mainly just above 30 nm (pure TMV: 18 nm), and the lengths are usually above those of single virus particles (virions) (300 nm), as well known from linear aggregation [146]. Hence TMV is completely coated with a dense and uniform layer of ≈5 nm of material, which should be iron oxide. From our SEM images we cannot deduce meaningful information on a possible mineralization of the internal 4 nm wide

channel of TMV (which can indeed be filled with ferromagnetic metals [6, 25]). TEM image of mineralized TMV (figure 5.2.2) shows an empty channel or at least the amount of iron oxide (if any) inside the channel is too low to be detected by transmission electron microscopy. However, it is obvious that the external coating strictly follows the viral shape (rod-like), hence the virions are still present, and the objects should be tubes, not filled rods. TEM imaging of mineralized plant viral particles shows that during precipitation of iron oxide on the exterior, TMV is not destroyed and rather remains intact. This can be seen in the TEM image (figure 5.2.2) as we see a smooth feature at the iron oxide/TMV interface. We can give a lower limit for the amount of iron oxide present on the external surfaces of a single TMV rod. Assuming an minimum coating thickness of 5 nm, a virion length of 300 nm and diameter of 18 nm, and the bulk density of Fe_3O_4 (5.17 g/cm^3), we obtain $5.6 \cdot 10^{-16}$ g of oxide.

Different from the rather smooth layer on each individual TMV, the aggregation of the rods during the process is less well controlled. The precipitating oxide binds to all available external surfaces of TMV, bare and in the state of mineralization. In this way, two virions that accidently touch, are quickly “cemented” into a stable junction. This finally yields an irregular network or grid of mineralized TMV (figure 5.2.1). This means that also in suspension there is no mobility of individual TMV. However, each single virion remains accessible for the ions, and is completely mineralized (figure 5.2.1). The coating is sufficiently thick to be studied by energy dispersive X-ray spectroscopy (EDX) even on single rods, see figure 5.2.3. Iron that had been in contact with an aqueous phase and with air must be oxidized, so we can infer the presence of iron oxide(s) and/or iron hydroxide(s) from our EDX results. Apart from silicon (sample substrate) and traces of sodium, we found no other elements, and can thus exclude large amounts (% range) of impurities, including precipitated educt salts (which we removed by dialysis).

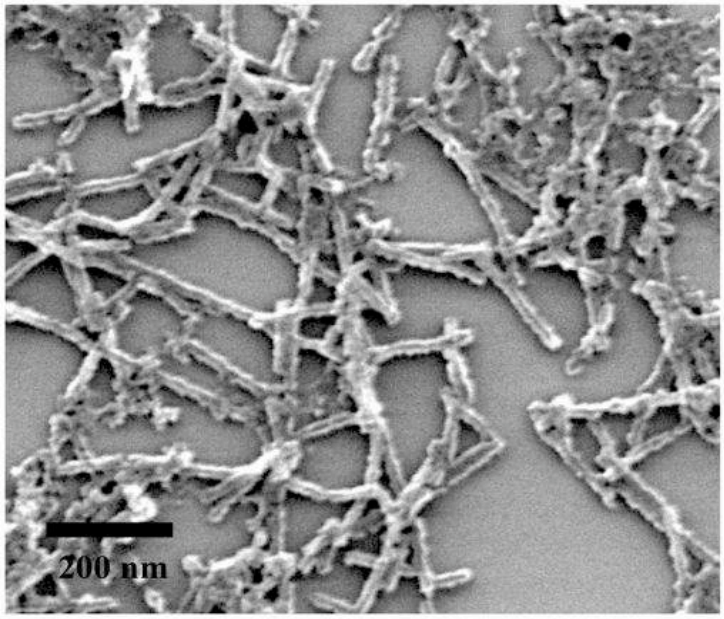

Figure 5.2.1. SEM image of TMV mineralized with a mixture of Fe^{2+} and Fe^{3+} at pH 9. The virions are all homogeneously coated (light grey) and form a grid-like irregular network.

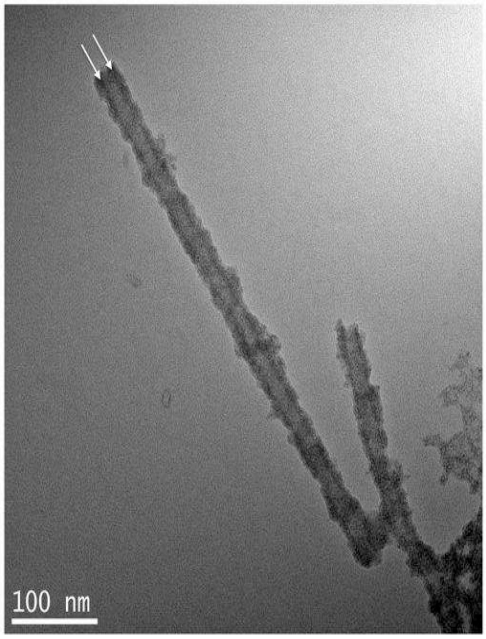

Figure 5.2.2. TEM image of two (end-to-end aggregated) TMVs mineralized with iron oxide layer of about 5 nm. The image shows two parallel black lines (separated by 18 nm) (indicated by two white arrows) at the interface between TMV and iron oxide, defining the diameter of the tube. The virus is still intact.

5.2.2 Magnetometry and Diffraction Studies

We analyzed the magnetic properties of dried droplets of this suspension with a global method, SQUID-VSM (see section 3.2, *"SQUID"* in chapter 3). We made sure that the sample purification had removed all larger objects, such as micrometer-sized iron oxide crystals, which would most likely override the small signals from the nanotubes. Figure 5.2.4 shows a hysteresis of the magnetization at 300 K with a saturation magnetization of 0.00082 emu/g.

From the calculated $5.6 \cdot 10^{-16}$ g of Fe_3O_4 per virion (see page 62), we obtain only $4.6 \cdot 10^{-19}$ emu per tube, which does not suffice to align the tubes in a magnetic field during synthesis. The magnetization at 5 K (figure 5.2.5) is very similar to the result at 300 K; as expected, the low temperature results in a higher value of saturation magnetization. We can conclude that our iron oxide tubes are weakly ferrimagnetic. Since the synthesis of α-Fe_2O_3 (hematite) is not observed under our conditions (300 K), the magnetic behavior is a strong hint for either γ-Fe_2O_3 or Fe_3O_4 [147] (see section 2.3, *"Magnetic Nanoparticles in Medicine"* in chapter 2).

Our saturation magnetization is orders of magnitude below the values reported for the various bulk forms (76 emu/g for γ-Fe_2O_3 and ≈92 emu/g for Fe_3O_4 [148, 149]). Our nanotubes do not compare well with larger iron oxide tubes and rods either [150-154]. Zhou *et. al.* [154] obtained a value of 106 emu/g for γ-Fe_2O_3 nanorods, and Geng *et.al.* [153] report 81.7 emu/g for Fe_3O_4 nanotubes. While the saturation magnetization can reduce for a very small object, our extremely low value points to other sources than mere size reduction. Indeed our coercive field of 0.04 T (400 Oe) is higher than the values reported for bulk iron oxides and nanoparticles, e.g. 0.03 T for bulk γ-Fe_2O_3 [154], 0.008 T for γ-Fe_2O_3 nanorods [155], ≈0.013 T for bulk Fe_3O_4 [156], 0.017 T for Fe_3O_4 nanotubes [153]. However, an extreme value (0.266 T) was found for Fe_3O_4 nanorods [157]. We believe that such values, and indeed ours, are based on the high shape and magnetocrystalline anisotropies of very small 1D structures, when compared to bulk phases [157]. The effect is based on the alignment of the spins parallel to the principal axis. Higher energies are required to reverse them, which translates into increased magnetic coercivities [158]. However, this would require that our rods contain sizeable amounts of Fe_3O_4, without the usual saturation magnetization.

We believe that such a situation can be brought about when the structure is amorphous (or for extremely small crystallites). Indeed we found no XRD signals in our samples (black trace in figure 5.2.6). In order to exclude problems of the experimental setup or of the amount of material, we cross-checked our result with a sample of a similar amount of crystalline Fe_3O_4 nanoparticles (figure 5.2.7). Only the latter gave clear XRD signals that fit to Fe_3O_4 (or γ-Fe_2O_3, which gives quasi identical XRD patterns, but not to α-Fe_2O_3), while our sample yielded no signal above the noise level. Some peaks for NaCl were also seen in the XRD pattern. The NaCl peaks might come from two sources, i.e. they may either be coming from impurities in the chemicals used for the synthesis of mineralized TMV particles or it could be a result of a chemical reaction between $FeCl_3$ and NaOH. Trace amounts of NaCl salt still present in the purified sample give clear signals for crystalline NaCl. For iron oxide, from our SEM and TEM data we can rule out the presence of small particles, which would give extremely broad XRD peaks. Hence we conclude that our iron oxide nanotubes gives no XRD peaks at all, meaning that they are amorphous.

Amorphous structures often transform into crystalline phases upon thermal treatment. Our samples showed no changes in size or shape upon heating (tested by SEM) (figure 5.2.8), but thermal treatment in air (at 520 K) [159] and in vacuum (at 570 K) [160] produced the expected crystalline phase(s). They fit well to γ-Fe_2O_3 or Fe_3O_4, irrespective whether they were tested after heating in air (blue trace in figure 5.2.6) or in vacuum (red trace in figure 5.2.6). Heating in air surely oxidizes all material, and our XRD results show that the product is the expected γ-Fe_2O_3, while vacuum prevents oxidation, and should thus conserve all existing Fe_3O_4. Our results agree with literature reports on thermal treatment of Fe(II) oxides [159-162]. An additional peak, present already in the unheated samples, corresponds to NaCl from the educts in our synthesis. Apart from these changes on the atomic scale, we noted a huge increase in magnetic moment (figure 5.2.9). The saturation magnetization increased to >1 emu/g, while the coercivity reduced to ≈0.001 T. The values now fit nicely to typical crystalline and nanoscale iron oxides (as discussed above).

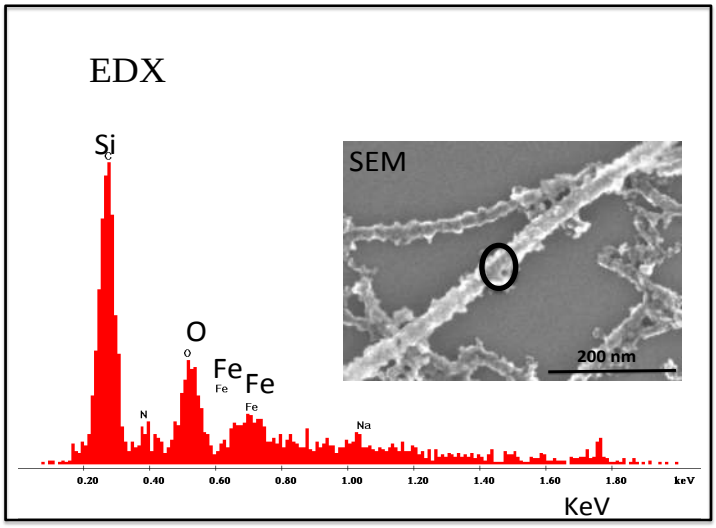

Figure 5.2.3. EDX spectrum showing the presence of iron on mineralized TMV. The silicon and oxygen signals stem mainly from the wafer substrate. Inset: SEM image; the spot from which the EDX spectrum was recorded, is marked.

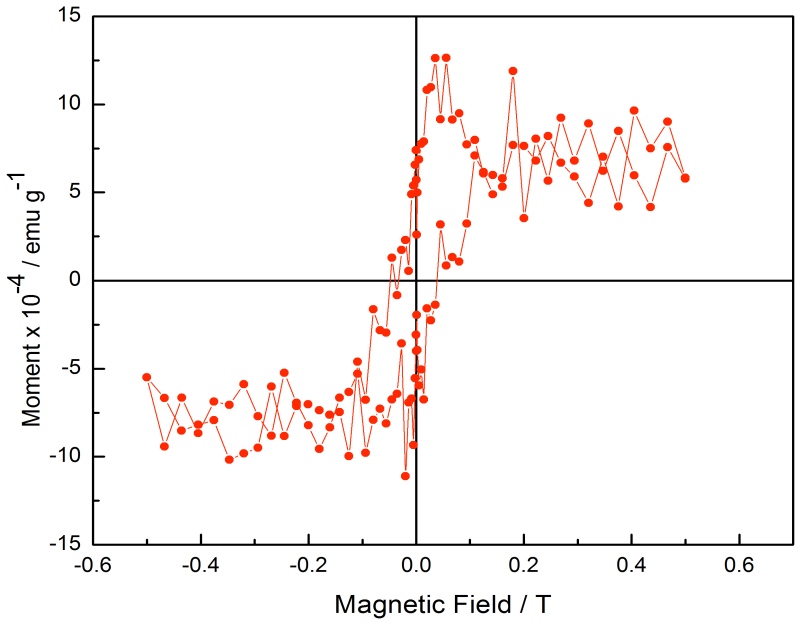

Figure 5.2.4. Magnetization as function of applied field for mineralized TMV at 300 K. The hysteresis points to ferromagnetic material.

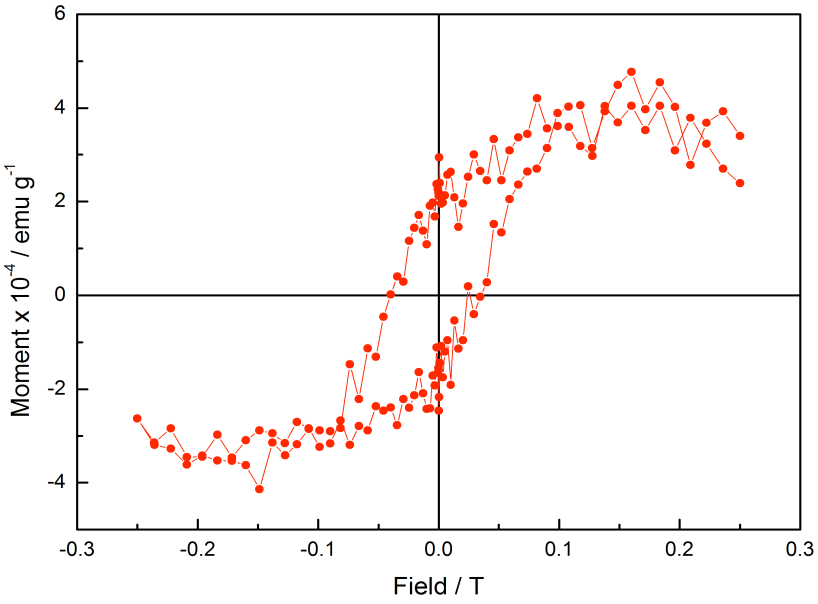

Figure 5.2.5. Magnetization as function of applied field for mineralized TMV at 5 K.

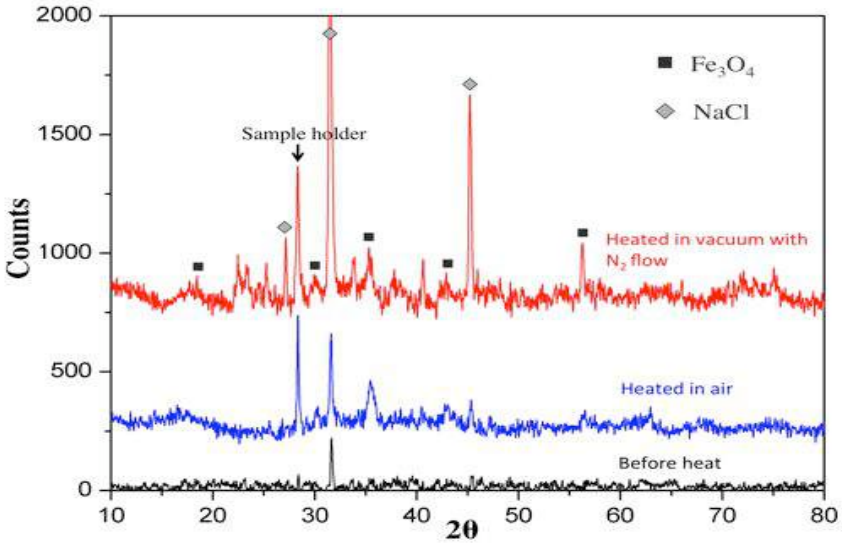

Figure 5.2.6. XRD from powder samples on a zero background holder. Black trace, mineralized TMV with traces of NaCl; blue, mineralized TMV after heating in air to 520 K; red, after heating in vacuum to 570 K.

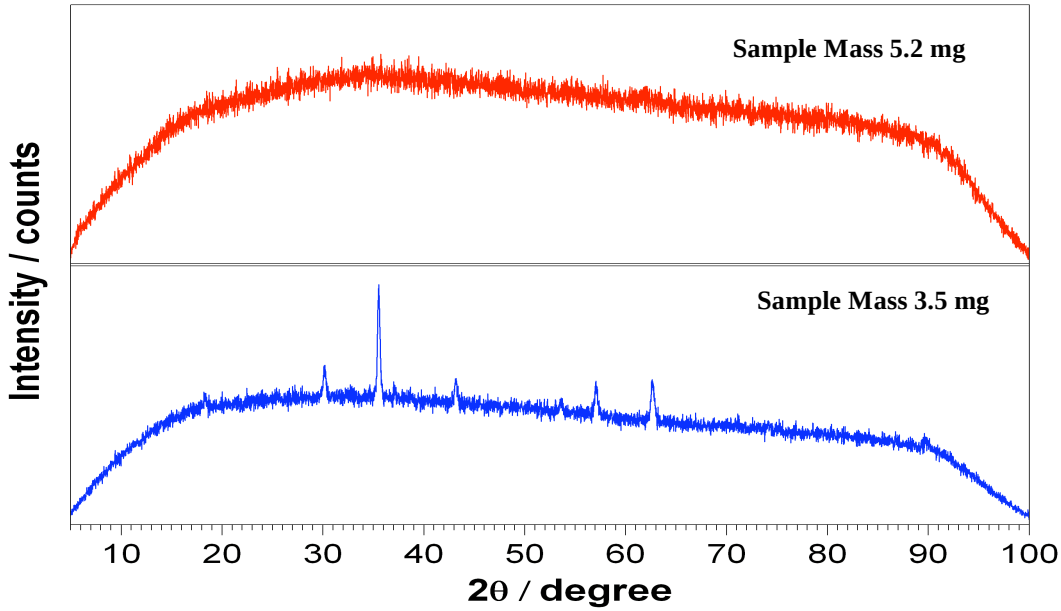

Figure 5.2.7. XRD from powdered samples of a standard Fe_3O_4 powder (blue pattern) and mineralized TMV particles (red pattern) on a zero background holder. The Fe_3O_4 standard sample (of mass 3.5 mg) gave characteristic peaks known for Fe_3O_4 whereas mineralized TMV particles (of mass 5.2 mg) resulted in a flat line. This experiment proved that our mineralized TMV particles are amorphous.

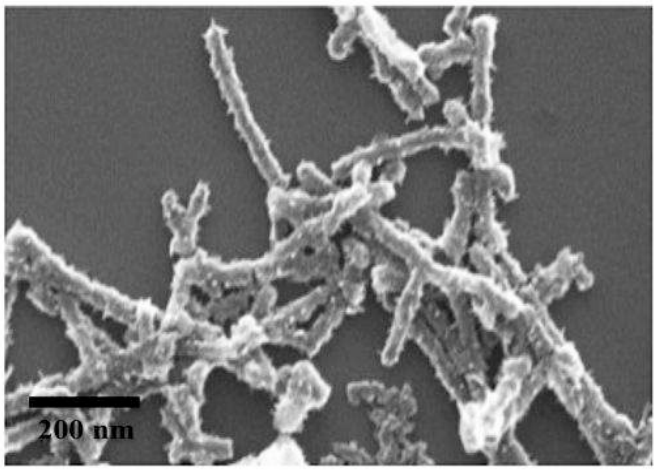

Figures 5.2.8. SEM image iron oxide coated TMV tubes after 3 hours of thermal treatment. It can be seen that they still maintain their tube-shaped structure.

5.2.3 XANES

In order to verify and to expand our chemical analysis, we resorted to X-ray absorption near-edge spectroscopy (XANES), again from samples dried on silicon wafers. Figure 5.2.10 shows spectra for the sample and various references. A detail of the edge region is shown in figure 5.2.11. We found that the spectrum for the mineralized TMV is shifted toward higher energies with respect to the reference compounds. Actually the edge position (defined as the point of maximum slope) for mineralized TMV is the same as for γ-Fe_2O_3 (and for α-Fe_2O_3), suggesting pure Fe(III). However, XRD measurements of the air-annealed sample do not support the presence of α-Fe_2O_3 phase, so we can rule out the existence of a detectable fraction of this oxide. On the other hand, the white line (the first peak above the edge) is much more prominent for TMV iron oxide particles than for the γ-Fe_2O_3 reference, and thus quite similar to that of Fe_3O_4. In the pre-edge region (figure 5.2.12) iron oxides show a peak associated with non-centrosymmetric (tetrahedral) positions. These are occupied by Fe(II) in the case of Fe_3O_4, and by Fe(III) for γ-Fe_2O_3 [163]. Our peak is located between those of Fe(II) and Fe(III), but slightly shifted toward higher energies (Fe_3O_4). This confirms our assumption of a mixture of Fe(II) and Fe(III), and shows that they are indeed linked to oxygen atoms.

We can, however, not rule out small amounts of unreacted precursor salts (on TMV or on the substrate), e.g., $FeCl_3$ with its rather strong white line [147, 164] could account for the observed shift of the edge, but would go undetected in EDX. Air-oxidized Fe(II) species, too, can cause such shifts, and variations in the XAS spectrum [164]. Based on this argument, the (small) difference in the oxidation states evaluated from edge and pre-edge features can be ascribed to the fact that the pre-edge peak is only sensitive to non-centrosymmetric positions. This is compatible with the presence of non-oxidic Fe cations, with centrosymmetric Fe positions [165]. However, we recall that also in this case the iron oxide layer on the TMV should be mainly Fe_3O_4.

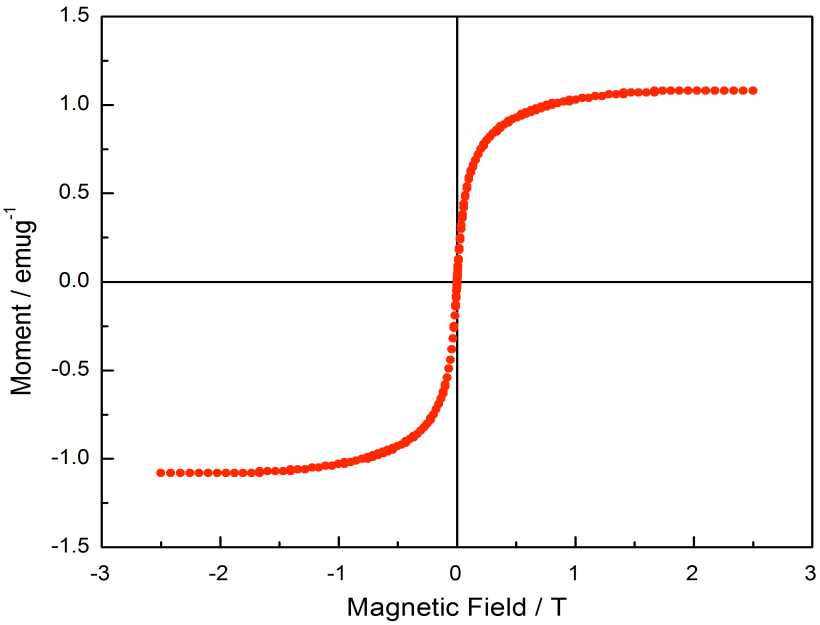

Figures 5.2.9. Magnetization as a function of applied field (at 300 K) for mineralized TMV particles after heating in vacuum at 570 K.

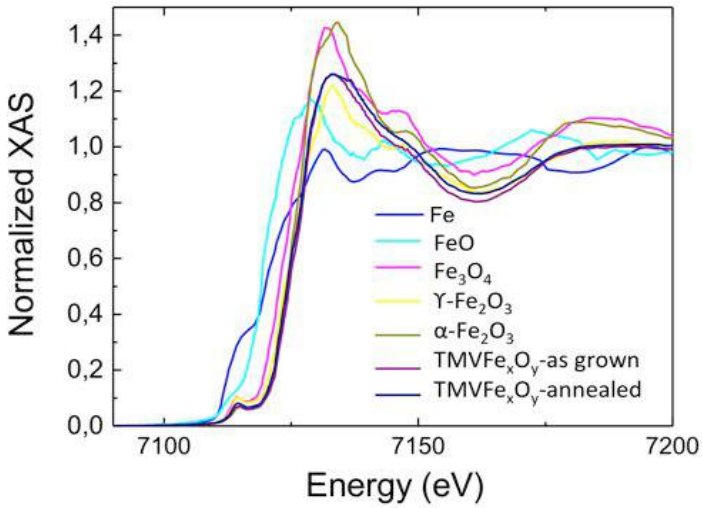

Figure 5.2.10. XANES measured at the Fe K-edge for mineralized TMV and the reference compounds.

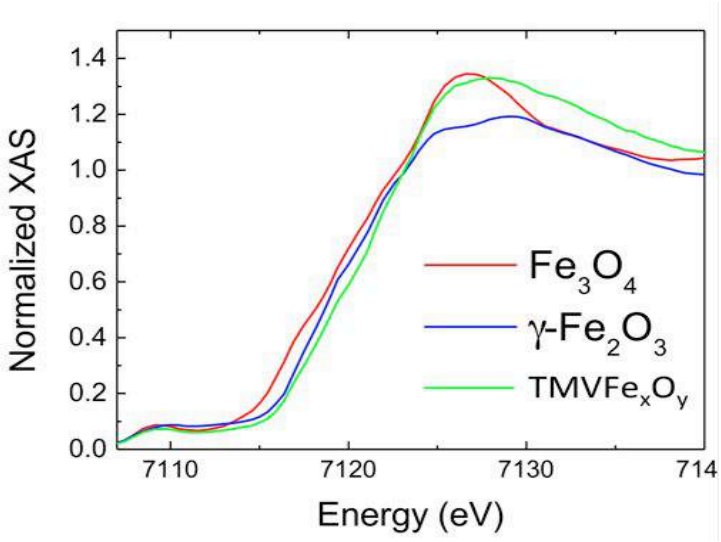

Figure 5.2.11. Detail of the XANES at the Fe K-edge region spectra measured at the. Mineralized TMV compared with bulk Fe_3O_4 and γ-Fe_2O_3 as references.

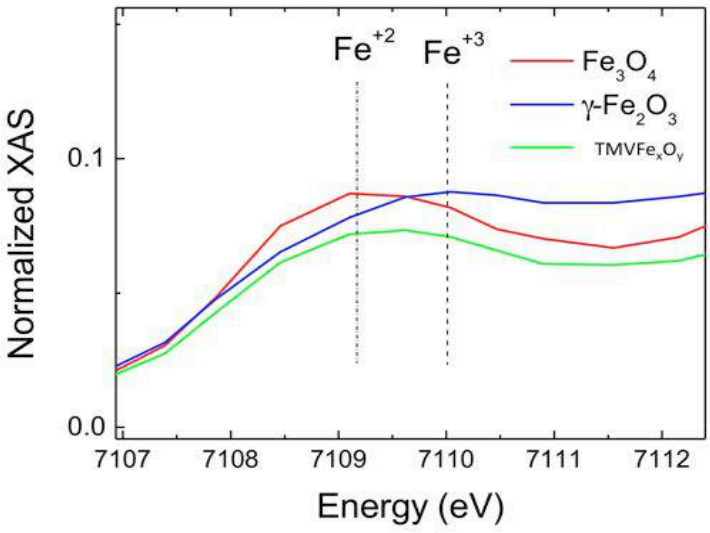

Figure 5.2.12. Detail of the XANES at the Fe K pre-edge region. Mineralized TMV compared with bulk Fe_3O_4 and γ-Fe_2O_3 as references.

5.2.4 Conclusions

Iron oxide can be grown by a simple and mild solution technique on the rod-shaped plant virus TMV from a mixture of aqueous Fe^{2+} and Fe^{3+}, which precipitates iron oxide on the exterior virus surface. SEM and TEM show that we obtained a thin and continuous layer of ≈5 nm thickness. The synthesis does not destroy the TMV and even with the coating of iron oxide it could be seen intact in transmission electron microscopy. Our annealed mineralized TMV tubes are magnetic enough and can be used for ferrofluids, where their shape induces much larger viscosity.

5.3 TMV Au Binding and Decoration

A number of organic biotemplates such as DNA, proteins, lipids and polysaccharides had been exploited for the synthesis of hybrid organic-inorganic structures at the nanoscale [166-169]. It is very important that the selected biotemplate is physically stable enough to withstand different types of treatments that it may come across during the synthesis and/or fabrication. TMV qualifies as an excellent candidate and therefore is one of the most favoured protein biotemplate for nanofabrication. Amongst metallic nanoparticles, Au has been the most promising owing to its chemical stability, easy synthesis, control over size, shape and bioconjugation [170-172]. Generally Au nanospheres can be easily synthesized by reducing auric acid and the size could be controlled by variations in the concentrations of sodium citrate [6, 25] or other organic molecules. Citrate is a special case since it acts as a reducing agent and binds to Au nanoparticles.

Au nanoparticles have unique chemical, optical, electrical and catalytic properties and therefore they have been studied most extensively. They are used for a number of applications such as in biosensors immunoassays, optical imaging and photothermolysis of cancer cells [6, 170, 173]. Au nanoparticles are normally capped with agents such as citrate for surface stabilization in solution, to give "sol". The citrate capping can be occupied by a number of chemical groups leaving the Au surface available for functionalization to DNA, peptides, or antibodies etc.

Au binding to TMV rods has already been reported by other groups [5, 23, 24]. We report a new, simple and facile method of synthesis and we do not require a TMV mutant unlike [5, 24]. An interesting fact about this synthesis is that it results in successful decoration of TMV by Au nanoparticles only at low pH values, i.e. 2.9 – 3.4, close to the isoelectric point (see section 2.1, *"Tobacco Mosaic Virus"* in chapter 2).

5.3.1 TMV-Au-TMV Dumbbells

Citrate-coated Au nanoparticles can bind specifically to TMV ends. When Au sol and TMV suspension are mixed, it results in removing coat proteins at both ends of TMV and therefore the RNA is exposed to the solution. Citrate-coated Au nanoparticles bind to the RNA molecules which protrudes from both ends of TMV particles. The

heterocyclic aromatic bases of the RNA replace citrate on the surface of the Au nanoparticles and bind to it (figure 5.3.1) as reported by Balci *et. al.* when they adsorbed TMV-Au dumbbells on Si wafers and immersed them in an electroless deposition bath [9].

The 6 nm citrate-coated Au nanoparticles attached to the ends of the TMV can be selectively "enchanced" (enlarged) via electroless deposition. It will result in increasing the size of the Au nanoparticles. It is done by mixing a suspension of Au-TMV-Au dumbbells in an ELD bath. The ELD bath containes CTAB (cetyltrimethyammonium bromide), ascorbic acid and $HAuCl_4 \cdot 3H_2O$ at pH 4. The selective enhancement of Au nanoparticles resulted in bulky Au attached to TMV at its ends, i.e. the particles grew as a result of Au deposition on them (figure 5.3.2) [9].

All these results (Au-TMV-Au dumbbells and their selective enhancement via ELD) had been published already [9] and were also reproduced in this work/thesis to carry on further investigations.

5.3.2 TMV Decoration with Citrate-Coated Au Nanoparticles

5.3.2.1 Zeta Potential of Au-Citrate Nanoparticles and TMV Rods

The Au nanoparticles as well as TMV rods, are both pH sensitive because of the presence of carboxyl groups on their surfaces. Zeta potential measurements are performed to investigate the surface charges of the citrate-coated Au nanoparticles and TMV rods. These measurements of Au nanoparticles and TMV rods were performed separately to understand their surface charges. The investigations show that successful Au binding to TMV rods only happens at pH 2.9-3.4. In this pH regime the Au nanoparticles are negatively charged. This is expected because the pK_a values of citric acid are 3.13, 4.76 and 6.4 respectively (figure 5.3.3) [174].

$$H_3Cit \rightarrow H^+ + H_2Cit^- \rightarrow 2H^+ + HCit^{2-} \rightarrow 3H^+ + Cit^{3-}$$

The pK_a values correspond to equal amounts of $H_{3-n}Cit^{-n}$ and $H_{2-n}Cit^{-1-n}$ for each n.

TMV rods, on the other hand carry a positive charge on the surface at low pH values (figure 5.3.4). Zeta potential values recorded for citrate-coated Au nanoparticles and TMV are given in table 5.3.1.

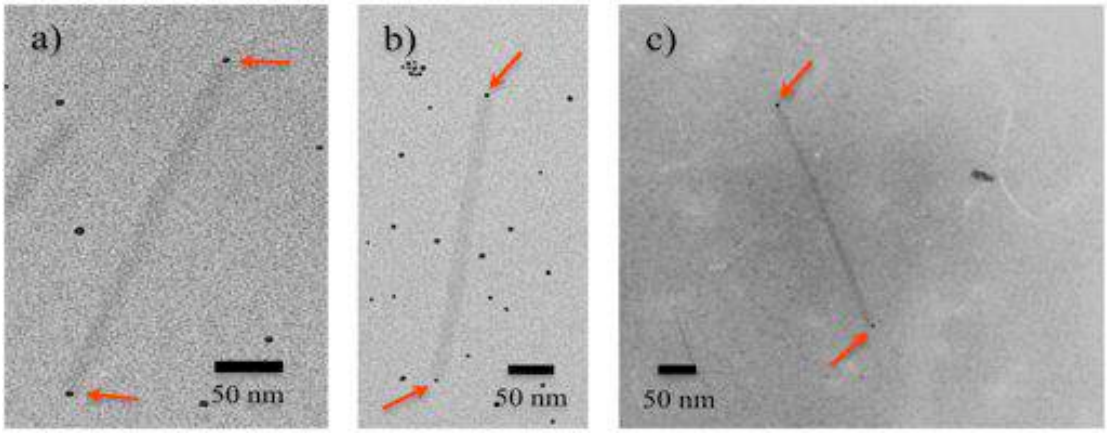

Figure 5.3.1. TEM images of Au-TMV-Au dumbbells synthesized by mixing citrate-coated Au nanoparticles (black spheres) with a suspension of TMV (grey) rods. Au nanoparticles bind to the ends of TMV where RNA molecules protrude. This was reproduced in this thesis (a & b) and was compared with already published results (c) [9]. The arrows indicate Au nanoparticles attached to TMV at ends.

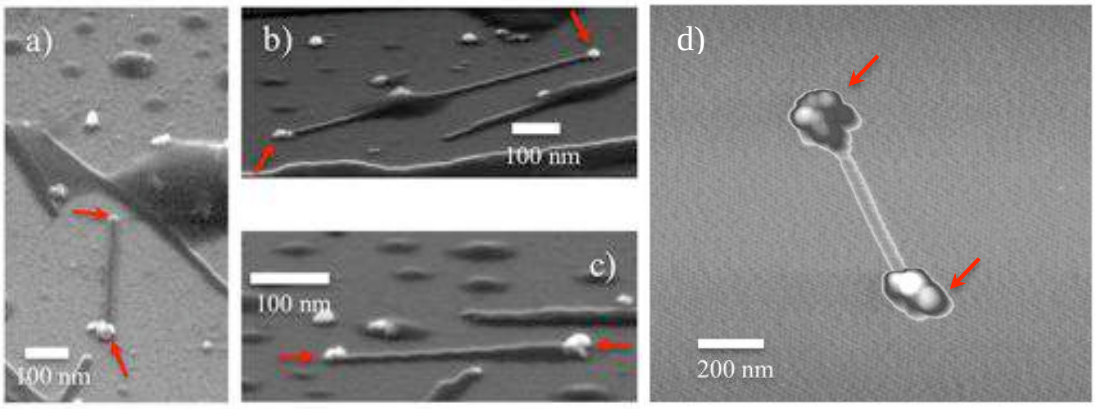

Figure 5.3.2. SEM (a, b & c) and AFM (d) images of selectively enhanced Au nanoparticles TMV ends. The Au-TMV-Au dumbbells were selectively enhanced by electroless deposition. SEM images of enhanced Au clusters (white) at TMV (black rods) ends reproduced in this thesis (a, b and c) with an AFM image of already published results (d) [9].

5.3.2.2 High Yield Binding of Au-Citrate Nanoparticles to TMV Rods

The mixing of Au-sol with TMV rods in the presence of concentrated (25 mM) citric acid results in the decoration of the TMV rods with the Au nanoparticles on the exterior. Since the size of the nanoparticles is more than 4 nm therefore the chances of binding inside the channel of TMV are not considered here. Figure 5.3.5 shows that Au nanoparticles stick to the TMV protein tubes decorating them all along their 300 nm length. Attempts to synthesize at pH 5.0 and 7.0 do not result in decoration of TMV although Au nanoparticles were seen to adhere to the ends of TMV as described in section 5.3.1 [9] (figures 5.3.6 and 5.3.7). The Au decorated TMV particles remain stable for (at least) two weeks upon aging at room temperature or refrigerated.

The assembly of these particles is driven by the electrostatic forces of attraction between negatively charged Au nanoparticles and positively charged TMV rods upon the addition of aqueous citric acid. Citric acid solution protonates Glutamate (Glu) and Aspartate (Asp) residues on TMV surface (figure 5.3.8) while keeping the Au nanoparticle only partially protonated, so they carry a negative charge at low pH values. On the other hand TMV at this pH contains both, negative and positive charges [7].

Note that TMV at pH 2.8 (i.e. the isoelectric point), it does not carry zero charges but equal amounts of positive and negative charges. The positive ones are mainly on TMV protein tube on the exterior [142]. The channel remains negatively charged at this pH (as does the RNA) [7]. At pH 5.0 the citrate-coated Au nanoparticles still carry negative charges while TMV is harbouring mixed charges of positively and negatively charged residues with negative charges in abundance as the deprotonation occurs mainly on the exterior. Au nanoparticles do not bind to the TMV rods because they experience only the negative net charge. At pH 7, TMV is totally deprotonated on the exterior. Hence the negatively charged citrate-coated Au nanoparticles do not bind to TMV rods. The charges (inside/outside) on TMV and citrate-coated Au nanoparticles are shown in figure 5.3.9.

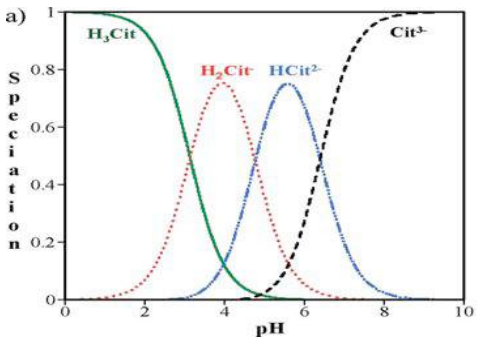

Figure 5.3.3. Citric acid speciation [174].

pH	Zeta Potential of TMV	Zeta Potential of Au
3.0	+3.30 ± 1.2	- 19.1 ± 2.3
5.0	- 41.5 ± 2.5	- 36.7 ± 5.8
7.0	- 47.4 ± 5.1	- 40.8 ± 1.1

Table 5.3.1. Zeta potentials of TMV and Au nanoparticles at pH 3, 5 and 7.

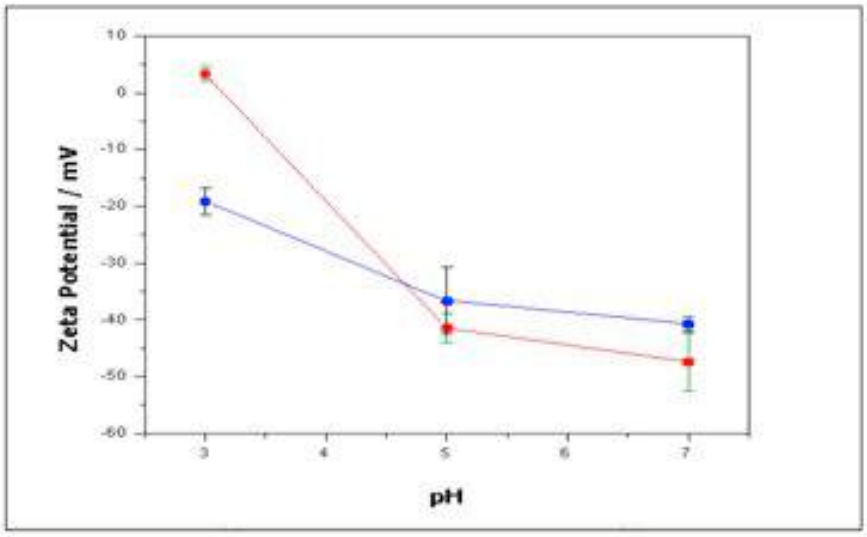

Figure 5.3.4. Zeta potential as a function of pH for TMV rods (red line with error bars in green) and citrate-coated Au nanoparticles (blue line with error bars in black).

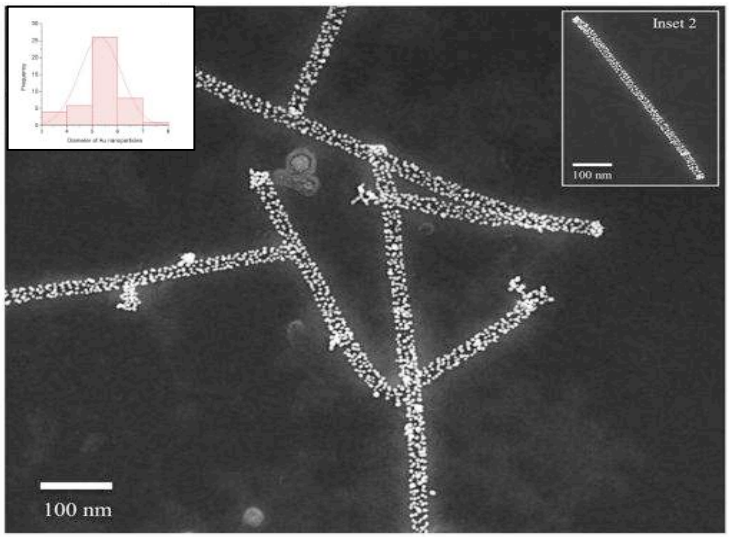

Figure 5.3.5. STEM image of citrate-coated Au decorated TMV particles. Au nanoparticles appear as small bright spheres on TMV rods at low magnification image of a network of TMV particles. Inset 1 is a histogram of the diameter of Au nanoparticles on decorated TMVs. Inset 2 shows two TMV particles (end-to-end aggregated) decorated by Au nanoparticles on its exterior protein rod.

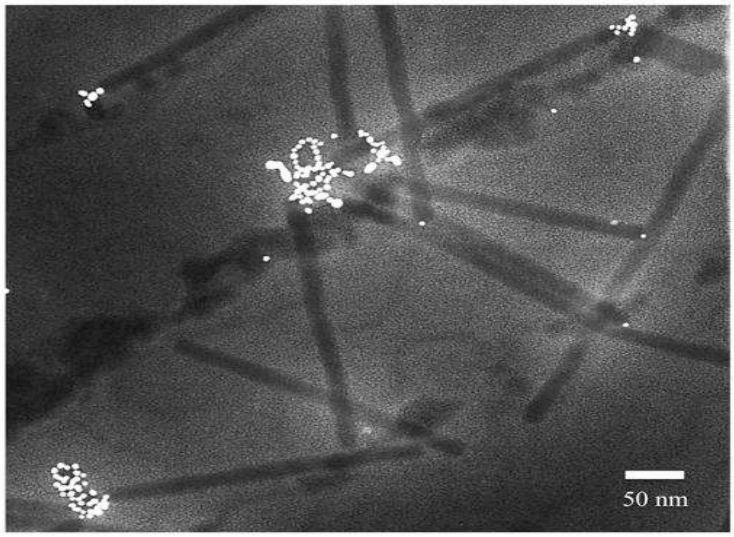

Figure 5.3.6. STEM image of citrate-coated Au nanoparticles (white spheres) do not bind to TMV (grey) rods to decorate them at pH 5. Au nanoparticles aggregated and a few particles also bound to TMV ends.

It has been previously reported that the 6 nm citrate coated nanoparticles bind to the TMV specifically by slicing off the coat proteins at both ends and subsequently exposing RNA. The RNA then replaces a citrate on the Au surface and binds to it [9]. Statistical analysis of the unmodified and decorated (modified) TMV particle lengths is given in table 5.3.2. The distance between two adjacent Au nanoparticles (on decorated TMV rods) has been also been measured and is shown as a histogram in figure 5.3.10.

TMV particles	Length (nm)
Unmodified Single TMV particles	292 ± 9
Unmodified Two (end-to-end aggregated) particles	539 ± 98
Single decorated TMV particles	234 ± 47
Two (end-to-end aggregated) decorated TMV particles	506 ± 65

Table 5.3.2. Length statistics of unmodified and decorated TMV particles from STEM imaging. For both, unmodified and decorated TMV, 70 particles each were measured.

5.3.2.3 Au Mercaptoethanol Nanoparticles and TMV

To test if there is any charge required for citrate-coated Au nanoparticles to bind to TMV rods, we exchanged the citrate shell of Au nanoparticles to 2-mercaptoethanol (2-MEA) [118]. The ligand exchange means that instead of negatively charged Au nanoparticles we have neutral Au nanoparticles. Au nanoparticles with 2-MEA shells do not result in binding to TMV rods but in a severe degree of aggregation under similar experimental conditions (figure 5.3.11). It shows that the negatively charged citrate coating of the Au nanoparticles is playing a pivotal role in the binding to TMV rods.

This result explains why Au nanoparticles with OH-containing shells of 2-MEA do not bind to TMV rods. The mercaptoethanol shell of Au does not deprotonate at the low pH values at which Au nanoparticles decorate TMV particles.

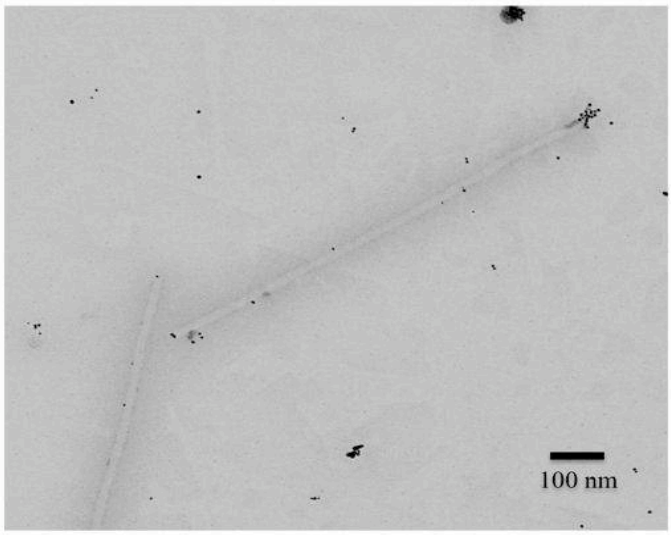

Figure 5.3.7. (Inverted) STEM image citrate-coated Au nanoparticles (black spheres) do not bind to TMV (grey) rods to decorate them at pH 7. Au nanoparticles aggregate and a few particles also bind to TMV ends. Au nanoparticles can also be seen in aggregated form.

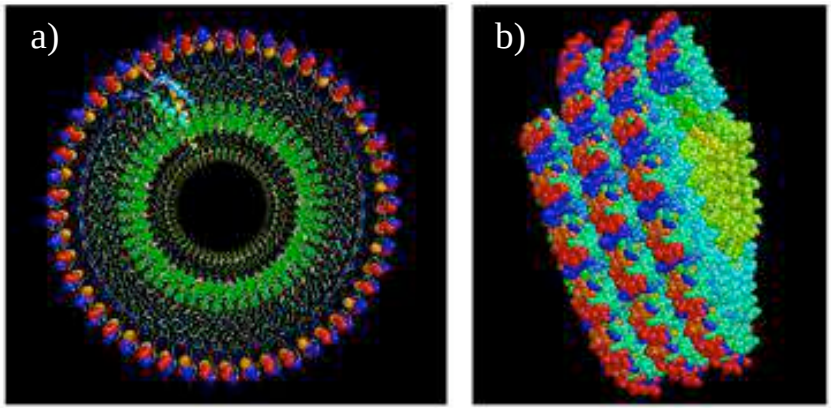

Figure 5.3.8. TMV graphics generated by RasMol from PDB entry "2TMV" [19]. (a) Acidic residues that are accessible are shown in space-filled representation (in front view of 49 coat proteins-three helix turns) in blue (Asp64), orange (Asp66) and red (Glu145). (b) The accessible acidic amino acids are shown in a side-view in space-filled representation to clarify their accessibility on the TMV. Asp64 is shown in orange, Asp66 in blue and Glu145 in red color. In both models the RNA is depicted in scaled ball and stick and in green colour. The model does not contain the last four amino acids, 154-158.

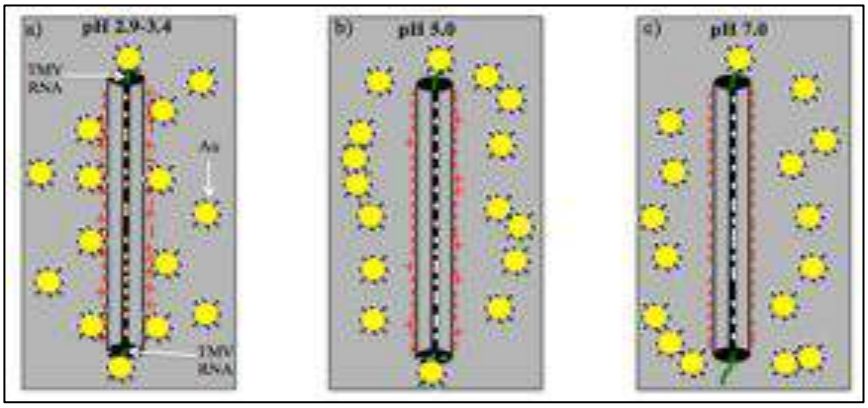

Figure 5.3.9: Charge distribution of TMV (inside the channel & outside, on the protein rod) and Au citrate nanoparticles. (a) At pH 2.9-3.4 TMV carries moieties of positive charge, and negatively charged Au binds to it. (b) at pH 5 TMV carries more negative charges and Au nanoparticles do not bind to it. (c) at pH 7.0 both TMV and Au are predominantly deprotonated and are negatively charged and no binding occurs between them.

5.3.2.4 TMV Decoration by Citrate–Coated Iron Oxide (Fe_xO_y) Nanoparticles

Since we postulate a (nearly) purely electrostatic mechanism, the chemical nature of the nanoparticles should not play an important role. We synthesized iron oxide-decorated TMV rods using the same recipe. TMV rods were mixed with citrate-coated iron oxide nanoparticles at low pH values. STEM imaging proved that 10 nm citrate-coated iron oxide nanoparticles bind to TMV rods at pH 3.0 and decorate them as they do in case of Au nanoparticles (figure 5.3.12). The acidic amino acid residues (Asp and Glu) of TMV are in the protonated state and make the protein rod of the plant virus positively charged. The iron oxide nanoparticles would have similar (negative) terminal charges because the stabilizing agent in both cases, (i.e. Au and iron oxide) is citrate and would therefore be negatively charged. The size of the nanoparticles may also play an important role in decorating TMV rods and above a certain threshold the nanoparticles may not be able to bind because of the lack of (essential) sufficient interaction sites. However, it has been confirmed that (citrate coated iron oxide) nanoparticles up to 10 nm (in diameter) can attach to the protonated carboxylic groups of TMV protein rod decorating it in the similar fashion as they do with 6 nm citrate-coated Au nanoparticles.

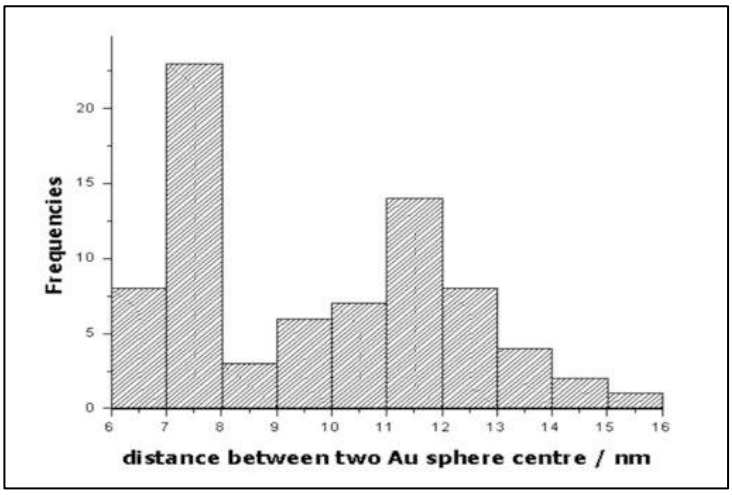

Figure 5.3.10. Histogram of major distances between Au nanoparticles (centre-to-centre) on decorated TMV rods.

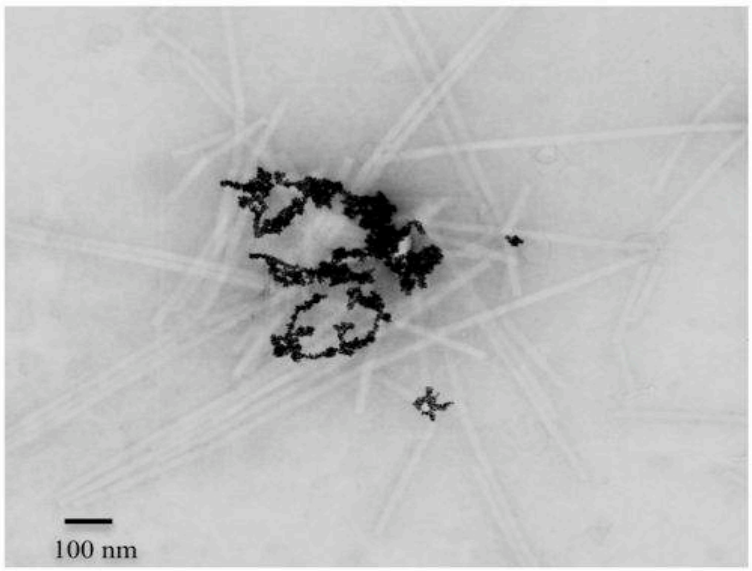

Figure 5.3.11. STEM image of mercaptoethanol-coated Au nanoparticles and TMV. Au nanoparticles appear as big aggregates (black spheres). TMV rods show no Au decoration and appear as naked (grey) rods.

5.3.2.5 Protonation of TMV Acidic Residues with other Acidic Solutions

The required low pH results in protonation of TMV rods and to a much smaller extent of the citrate-coated Au nanoparticles. Indeed this should not be limited to only citric acid and would be possible to achieve with other acids too. So we replaced the addition of aqueous citric acid by HCl solution. Our STEM imaging showed that both, citrate-coated Au and iron oxide nanoparticle bind to and decorate TMV rods at (pH 2.9-3.4) on the exterior as they do in case of citric acid (figure 5.3.13).

5.3.2.6 Stability of Au Decorated TMV Rods after Synthesis

In other additional stability tests Au decorated TMV rods synthesized at acidic pH were incubated at pH 5.0, 7.0 and 8.5 overnight. It was observed in the STEM imaging that no intact TMV particles could be seen after placing Au decorated TMV rods at pH 8.5 while the same decorated plant viral rods were stable enough to

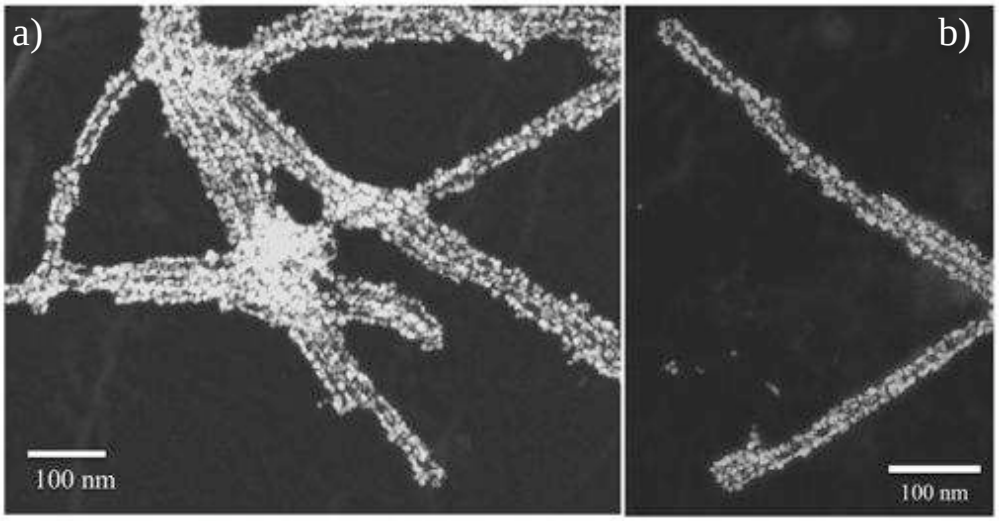

Figure 5.3.12. STEM images of citrate-coated iron oxide decorated TMV rods. (a) TMV network is decorated by bright appearing citrate-coated iron oxide nanoparticles. (b) Individual TMV rods decorated with citrate-coated iron oxide nanoparticles at higher magnification.

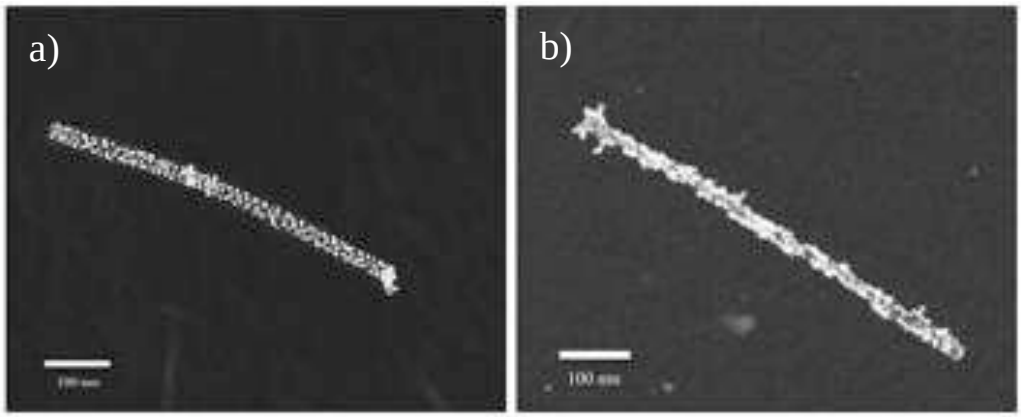

Figure 5.3.13: STEM images: (a) citrate-coated Au nanoparticles (white spheres) were able to bind to and decorate TMV rods when HCl solution (instead of citric acid) was used for the protonation of the acidic residues. (b) similar decoration was achieved by citrate-coated iron oxide nanoparticles decorating TMV rods.

withstand pH 5.0 and 7.0 overnight. At pH 8.5 TMV particles were destroyed which is already known for TMV, i.e at high pH values the coat proteins are deprotonated and Ca^{2+} ions are lost between carboxyl-carboxylate groups. The negatively charged carboxylate groups repel each other and results in viral particle disassembly [17]. Therefore, Au particles detached and aggregated (figures 5.3.14, 5.3.15 & 5.3.16).

5.3.3 Conclusions

The high-yield binding of citrate-coated Au nanoparticles specifically to TMV rods occurs by means of electrostatic forces of attraction. STEM imaging and zeta potential investigations prove the fact that the successful synthesis results due to the protonation of Asp64, Asp66 and Glu145 residues on the TMV protein rod while the whole rod is still not totally positively charged. The exchange of citrate shell to 2-MEA proved that the negative charges on citrate shell are important to Au-TMV decoration. TMV acidic residues can be protonated by other acids as well (like HCl) and similar TMV decorated with Au nanoparticles can be synthesized. This process cannot be limited to Au nanoparticles but any other type of nanoparticles with terminal citrate groups should attach to TMV rods. This is shown and proved for iron oxide nanoparticles under similar experimental conditions.

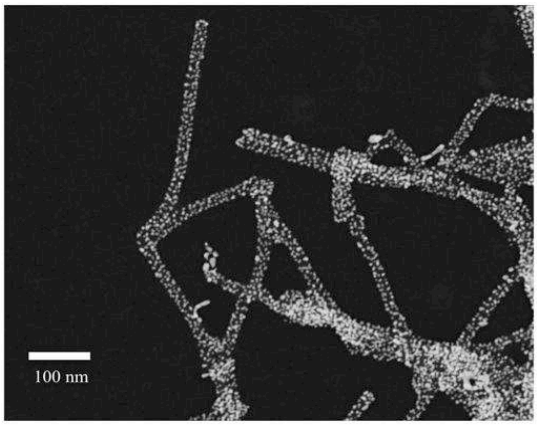

Figure 5.3.14. STEM image of Au decorated TMV with incubation at pH 5 overnight after synthesis at pH 2.9. The citrate coated Au nanoparticles (white spheres) are still attached to the TMV (black) rods.

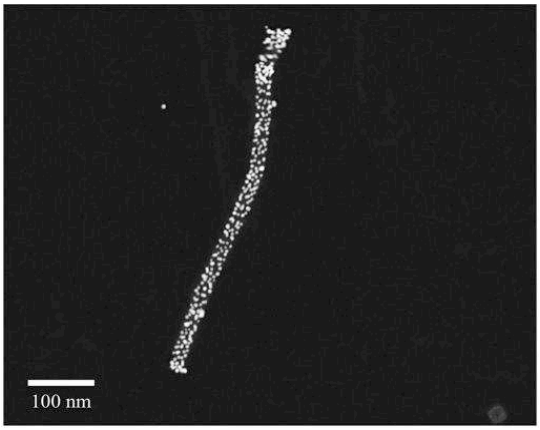

Figure 5.3.15. STEM image of Au decorated TMV with incubation at pH 7 overnight after synthesis at pH 2.9. The citrate coated Au nanoparticles (white spheres) are still decorating the TMV (black) rods.

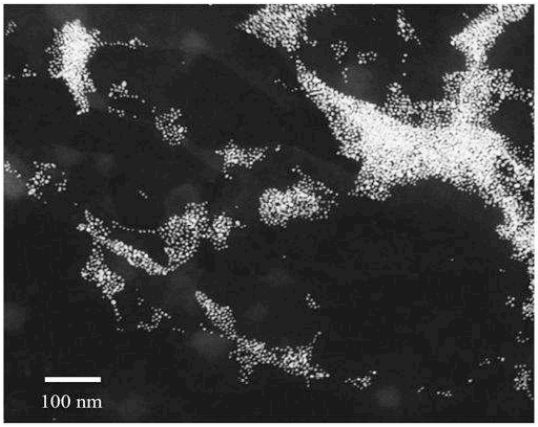

Figure 5.3.16. STEM image of Au decorated TMV with incubation at pH 8.5 overnight after synthesis at pH 2.9. Huge aggregates of Au nanoparticles were (white spheres) were seen all around without any TMV rods. (TMVs might have been destroyed by the high pH of the suspension).

5.4 Drug Encapsulation in TMV Channels

The discovery of cisplatin revolutionized biomedical sciences for the treatment of cancers. It is the first ever inorganic antitumor drug used clinically for over 30 years. It still remains one of the most widely used drugs in cancer therapies against ovarian, lung, testes and bladder cancer. In addition to cisplatin, more Pt(II)-containing drugs made their inroads to the clinical trials for the treatment of different types of cancers. So far three of them have been approved for clinical use for cancer cell therapies and they are oxaliplatin, carboplatin and nedaplatin [29, 32, 33] (see section 2.2, "*Pt-containing Drugs"* in chapter 2.0). Despite the fact these Pt(II)-containing drugs have been so effective in killing cancer cells, there were always reports of toxicity concerned with their application to tumor cells locally, i.e. normal/healthy cells were also destroyed along with the cancer cells. This led to devise strategies to target the delivery to only cancer cells, and to avoid the normal cells and reduce the toxicity issues. Efforts started to synthesize containers for selective delivery of these drugs to tumors only. A number of carriers (platforms) are being investigated by different research groups all around the world to deliver these drugs selectively to cancer cells. For the last decade a lot of effort is being put on nanoscale drug carrier systems such as liposomes [175], zeolites [176], carbon nanotubes [177], polymers [178], cellular vesicles [179] and viruses [180]. Biotemplates are often the preferred carrier systems as it is not easy to produce synthetic carriers with size, shape, composition and functional uniformity. Naturally occurring biotemplates on the other hand are well controlled by processes in nature and do not suffer from these shortcomings.

5.4.1 Encapsulation of Cisplatin and Oxalipatin in the TMV Channels

TMV particles were encapsulated with the classical Pt(II)-containing drug, cisplatin, at neutral pH values. TMV particles that were free of buffer salts were incubated overnight in a concentrated solution of cisplatin. TMV particles were then imaged in an electron microscope for stained channels. In case of Bright Field (BF) microscopy stained channels appear "dark", while they are "bright" in Dark Field (DF) mode. Both show the presence of a heavy metal inside the 4 nm channels of TMV particles. Since the

samples were not stained with uranyl acetate or phosphotungstic acid, the presence of heavy metal inside the channels proved that the Pt-drug could access TMV channels and stay inside. Figure 5.4.1 shows our first successful result of cisplatin drug encapsulation in the 4 nm channels of TMV at pH 7.5. It can be seen that all TMV particles clearly have a heavily stained channel appearing dark in BF mode. EDX spectra showed clear peaks of Pt and Cl (figure 5.4.2), supporting the presence of cisplatin inside the channels. The image also shows two other important features, i.e. the TMV is not only stained inside the channel but also on the exterior. The second feature is the presence of a number of chunks (appearing as black aggregates) of a heavy metal (Pt). This could be cisplatin that has been reduced by the beam of the microscope. The presence of cisplatin outside could be explained by the fact that this sample was not purified (the emphasis was more on the optimization of conditions to successfully encapsulate the drug inside the confined 4 nm channel).

Purification of the samples could be effectively done by dialysis against water. After 1-1.5 h dialysis of the drug-encapsulated TMV particles, most of the dissolved drug that could not enter TMV channels was washed away as seen in figure 5.4.3. It could be noted that even after purification, i.e. dialysis against water, the viral particles did not only contain the drug in the channels, but it adhered also to the exterior coat proteins.

Oxaliplatin has been reported to be more efficient in the destruction of tumor cells [181] therefore we expanded our work and incubated TMV particles with concentrated solutions of oxaliplatin at neutral pH values. The results were similar to the ones that were obtained for cisplatin. Oxaliplatin was encapsulated within the central channels of the plant virus, confirmed by electron microscopy imaging (figure 5.4.4) and supported by EDX spectroscopy (figure 5.4.5). In case of oxaliplatin there were no peaks obtained for Cl (oxaliplatin does not contain Cl). It proved that Pt(II)-containing drugs could be confined in the 4 nm channels of TMV particles under optimum conditions.

5.4.2 Drug-TMV Interactions

Cisplatin and oxaliplatin do not have interactions only with the nucleic acids but they also interact with a variety of proteins [182-186]. They are known to bind to a number of proteins such as hemoglobin, transferrin, ubiquitin, myoglobin, cytochrome *c*, lysozyme and human serum albumin. These proteins have been shown to coordinate

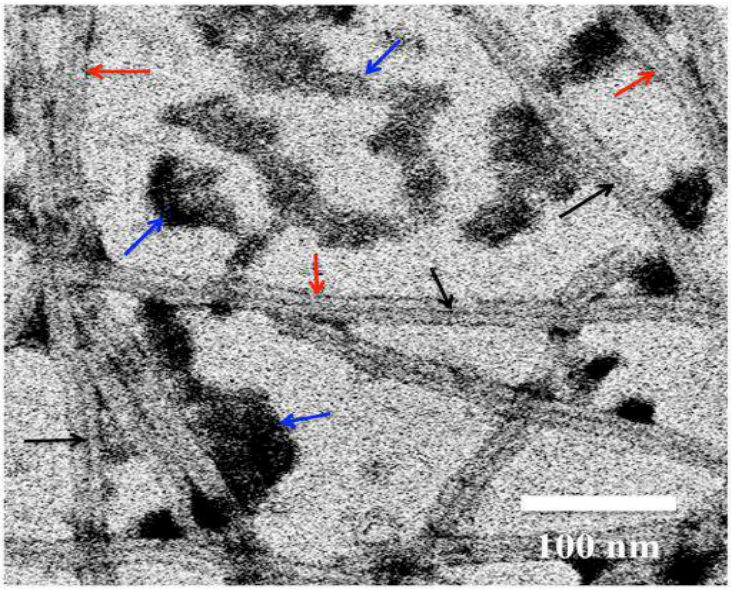

Figure 5.4.1. TEM image of TMV particles encapsulated with cisplatin at pH 7.5. The channel of TMV particles can be seen filled with Pt(II)-drug and appears as a black line (indicated by black arrows). The drug also binds to the exterior coat proteins of TMV (shown by red arrows), again appearing black, while TMV appears grey. The sample contains big chunks of (reduced) surplus Pt shown by blue arrows.

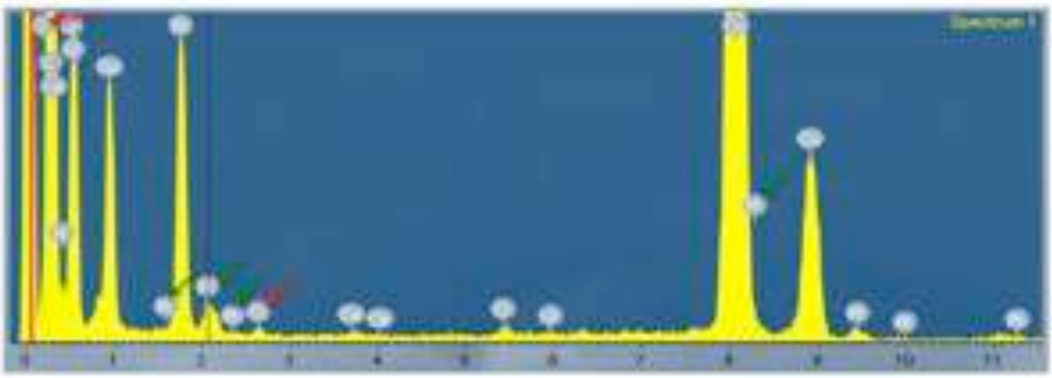

Figure 5.4.2. EDX Spectra of cisplatin-encapsulated TMV particles. Pt peaks are shown by green and Cl by red arrows. Signals of Cu are coming from the TEM grid while Ca from TMV structure. Cr and Si peaks are originating from the TEM sample holder.

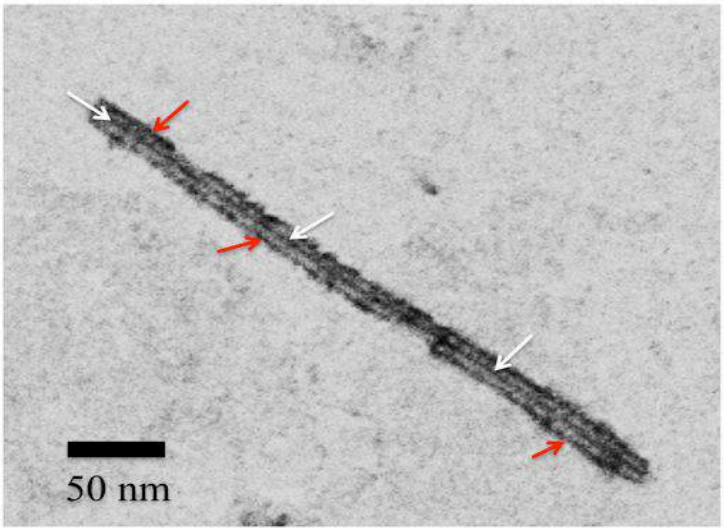

Figure 5.4.3. Inverted STEM image of cisplatin-encapsulated TMV particle. The presence of cisplatin in the channel is proved by a dark contrast in the channel (shown by white arrows). The drug also binds to the exterior coat proteins (shown by red arrows). Dialysis removed most of the unbound/non-encapsulated drug from the solution and no chunks of Pt were found on the TEM grid (unlike the non-purified figure 5.4. 1).

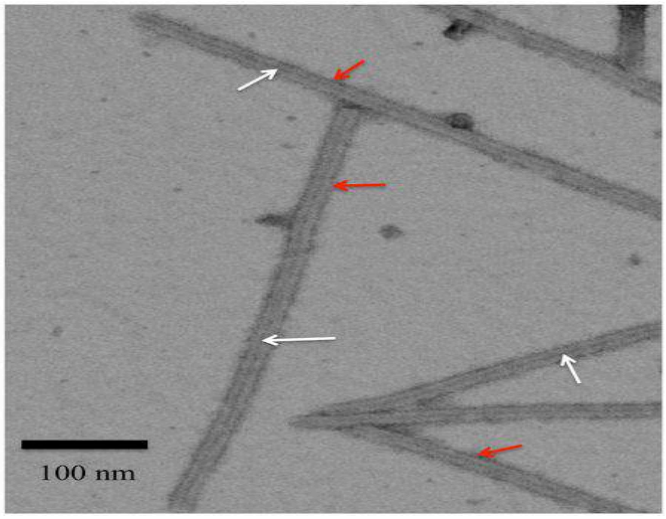

Figure 5.4.4. Inverted STEM image of oxaliplatin-encapsulated TMV particles. The dark channel proves that channels are encapsulated with the drug (shown by white arrows). The drug also binds to the exterior coat proteins (shown by red arrows). Dialysis removed most of the unbound/non-encapsulated drug from the solution and no chunks of Pt are found on the TEM grid.

with cisplatin/oxaliplatin mainly through methionine, cysteine, histidine and in some cases also threonine [182-191]. Tobacco mosaic virus has no methionine and histidine yet there is a cysteine residue located at amino acid position 27. Cys27 is deeply buried in the coat protein and is not accessible [23]. Therefore, the Pt(II) of cisplatin/oxaliplatin does not have suitable functional groups available on or in TMV protein tube where it has a high affinity to bind to. The only chances are with threonine as there are threonine residues present and accessible on the exterior of TMV (figure 5.4.8b) [19]. But already the interaction with threonine is reported to be weaker and found only in some cases [182, 183]. Therefore we could rule out stronger (covalent or complex formation) interactions of our Pt(II)-containing drugs with TMV.

Both of the drugs (cisplatin and oxaliplatin) that we encapsulated in the channels have been described well for their hydrolysis (see section 2.2, *"Pt-containing drugs"* in chapter 1.0). Both drugs undergo hydrolysis and depending upon the pH could undergo aquation and exist in either monoaqua or diaqua complexes. In either case, the drug molecules become positively charged. Therefore we speculate that the interaction between the drug and TMV is (a weak) electrostatic (one). At neutral (or near neutral) pH values TMV is highly negatively charged in the channel as well as on the exterior. The positively charged drug molecules would bind electrostatically to the negatively TMV particles and that is why we see the drug not only binding inside the channel but also on the exterior coat proteins. This electrostatic interaction is rather a weak one as we could wash out/effuse (almost) all the bound drug via dialysis over long period of times. We can exclude stronger interactions between the drug molecules and the protein tube of TMV (since they would not be weak enough to be broken by only dialysis).

5.4.3 Effusion of Drugs from TMV Channels

After successfully optimizing the conditions for drug encapsulation (confinement) in the channels and removing the non-encapsulated drug from the solution, it was necessary to show the confined drug inside the channel could be exploited for the killing of cancer cells. This had been achieved by extending the purification of encapsulated viral particles.

In our experiments we saw that initial dialysis of 1-1.5 h could remove the dissolved and non-encapsulated drug from the incubation bath of TMV and cisplatin or

oxaliplatin. If the dialysis against water was kept on for long periods of time the bound drug on the exterior coat proteins of TMV eventually washed out leaving the channels still filled. Figure 5.4.6 shows a TMV particle that was encapsulated with oxaliplatin and was dialyzed against water for long periods. The drug that was bound to the exterior of the viral particles was eventually washed out. The image clearly shows a dark (oxaliplatin filled) central channel and unstained (grey) TMV protein tube. This actually paved the way to effuse the drug out of channels by longer dialysis against water. Oxaliplatin-encapsulated TMV particles that were dialyzed against water for longer periods (6-7 h) appeared like unstained TMV particles in electron microcopy imaging which showed the drug was leached out of the of the TMV channels too (figure 5.4.7). We found out that somehow the effusion of the drug is slower from the channels than the drug bound to exterior coat proteins of TMV. A possible reason could be the presence of the viral structure itself because the lining of the channel is dense in acidic amino acids [19] (figure 5.4.8a). These residues remain deprotonated at (close to) neutral pH values making the channel negatively charged. The positively aquated complex of the drug might have a stronger electrostatic interactions than they find on the exterior protein tube of TMV. Pt(II) of these drugs is reported to have a rather weak interaction with threonine [182, 183]. TMV has threonine in the channel as well as on the outer parts of the coat protein (figure 5.4.8b). This weak interaction may be responsible for the slow wash out of the drugs of the exterior protein tubes and even slower for effusion of the channel as the channel provides a lining of acidic amino acids and threonines in a confined space, providing more stronger interaction than on the exterior protein tube of the virus. Therefore it is confirmed that TMV could prove a good tubular nanoscaffold drug carrier for targeted drug delivery against cancers.

5.4.4 Drug Encapsulation of PEGylated TMV Particles

PEGylation (coating with $[-CH_2-CH_2-O-]_n$) is a well-known method of passivizing protein molecules so that they cannot be attacked and destroyed by the immune cells inside the body [192]. Pegylation actually gives a brushy appearance to protein molecules and physically avoids the access of immune cells (and/or proteins) to reach the antigenic determinants of foreign protein recognized by the immune system [192]. Our model drug delivery platform (TMV) is a protein tube. It is also highly immunogenic [2] and therefore has been used extensively in the synthesis of sub-unit

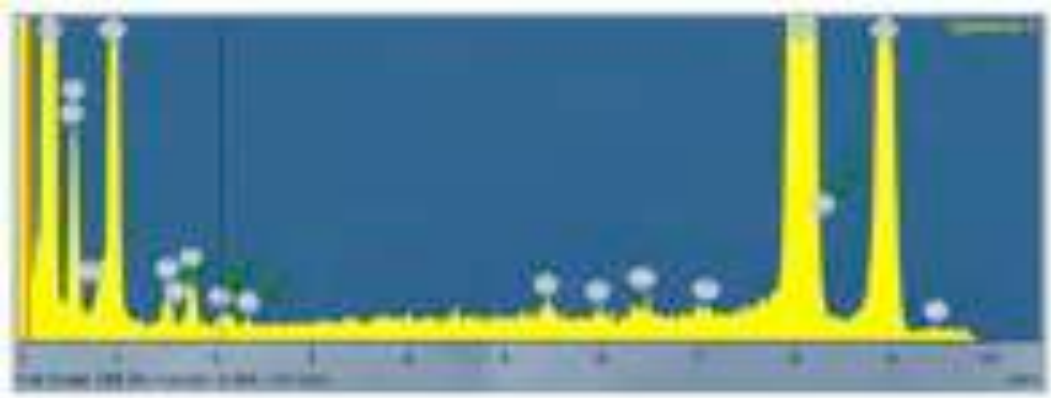

Figure 5.4.5. EDX spectra of oxaliplatin encapsulated TMV particles. Pt peaks are shown with green arrows. No Cl peaks were seen unlike cisplatin since oxaliplatin does not have Cl ligands. Cu and C peaks are coming from the TEM grids. Fe, Cr, Si and Al peaks originate from the sample holder of the microscope.

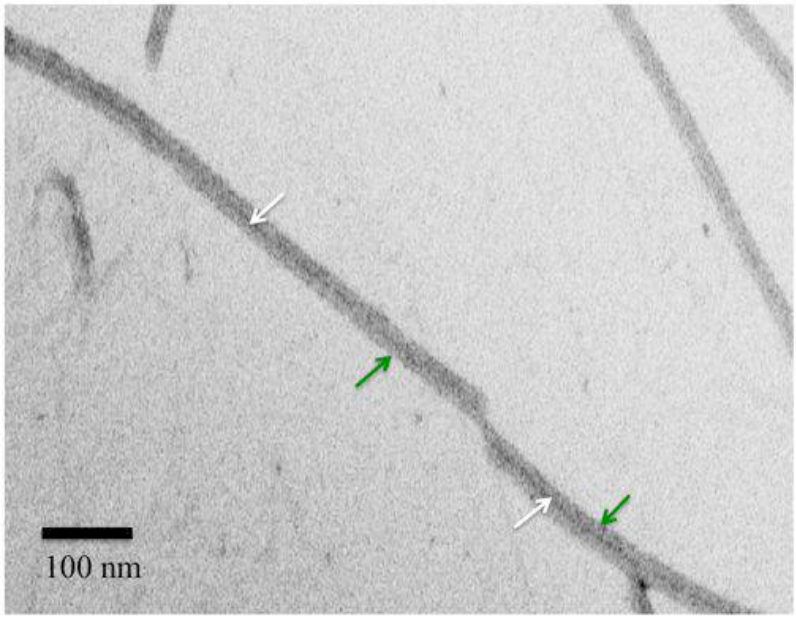

Figure 5.4.6. Inverted STEM Image of oxaliplatin-encapsulated TMV particles after extensive dialysis. TMV loses the drug bound to the exterior coat proteins (green arrows show that no drug is bound to the exterior). It still contains drug in the channel though, shown by a dark black line inside a grey-coloured TMV particle (shown by red arrows).

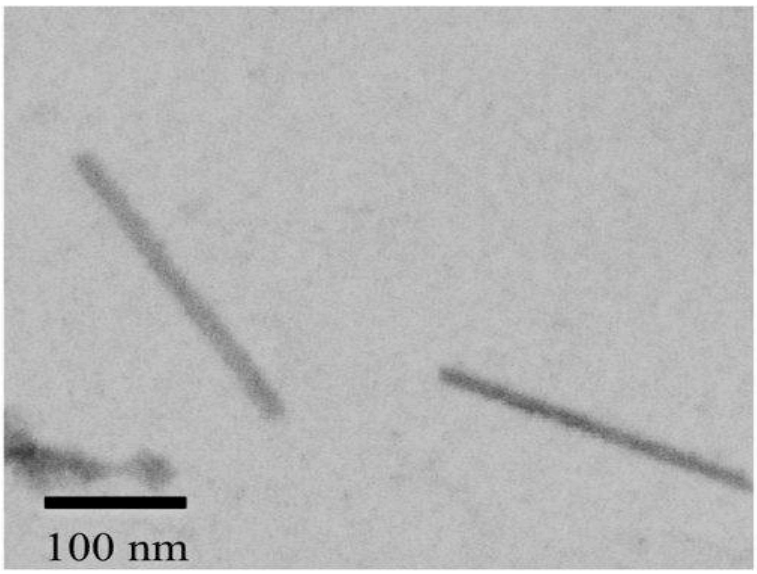

Figure 5.4.7. Inverted STEM image: Longer dialysis of oxaliplatin-encapsulated TMV lost the entire drug bound inside the channel and on the exterior coat proteins. TMV particles (grey rods) lost contrast during imaging and did not appear sharp in comparison to when they contain bound Pt(II)-containing drugs.

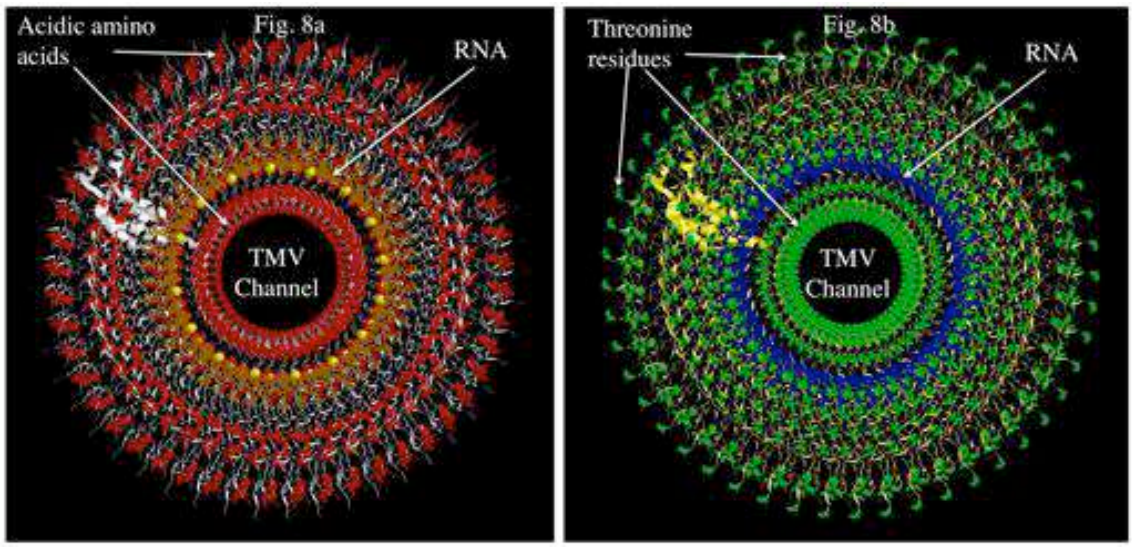

Figure 5.4.8. Graphics generated from the crystal coordinates of (PDB Id: 2TMV) [19] by RasMol visualization software. (a) The protein backbone is shown in white ribbons, and the RNA in orange sticks. Acidic amino acids inside and outside TMV are shown as red-coloured ball and stick display. The TMV channel is densely lined by acidic amino acids. (b) The protein backbone is shown in yellow ribbons, and RNA in navy blue sticks. Threonine residues inside the channel and on the outer protein tube are shown in green-coloured ball and stick display. The model does not contain the last four amino acids, 154-158.

vaccines [193-196]. Hence, it is essential to pegylate it if it is to be used as a drug delivery carrier for targeting cancer cells. In our case, TMV had been pegylated using EDC-NHS chemistry using a bifunctional PEG molecule. For pegylation we used a Lys mutant of TMV, i.e. it exposed an extra lysine on the exterior coat proteins. Pegylation of TMV mutants has been achieved (by Sven Degenhard, Ph.D Thesis, *in preparation*, University of Stuttgart) and will be discussed in detail in his Ph.D thesis. The pegylated samples of TMV_{Lys} were encapsulated with oxaliplatin to check if pegylation would interfere with encapsulation of the drug inside the TMV channels.

Since all of the previous drug encapsulation experiments were performed with wild type TMV particles, encapsulation of both TMV_{Lys} mutants, pegylated and non-pegylated was performed. Electron microscopy images showed that (non-pegylated) TMV_{Lys} mutants behave similar to wild type TMV particles and were encapsulated with Pt(II)-containing drug in the channel. The drug was also bound to the exterior coat proteins like in all other cases (figure 5.4.9). In case of pegylated TMV_{Lys} particles, we obtained mixed results and could not reproduce them. Pegylated TMV_{Lys} particles were at times found with drug encapsulated only in the central channels (figure 5.4.10) while other times the same phenomenon of drug binding inside the channel as well as on the exterior was seen (figure 5.4.11). It might be possible that this in turn was affected by the degree of pegylation, i.e. the more the viral particles were pegylated, the less interaction was found by drug molecules on the exterior, and vice versa.

5.4.5 Capping of Drug Encapsulated TMV Particles

In case of exploiting TMV as a nanoscaffold for drug delivery, it is essential to cap the viral protein tube at both ends so that the encapsulated drug stays inside in the confined cage. Drug-encapsulated TMV particles were attempted to be blocked at the ends by citrate-coated Au nanoparticles in two different strategies.

a. In this strategy TMV particles were incubated overnight in concentrated solutions of the drug and Au-sol (citrate-coated 6 nm Au nanoparticles) together. Since the Au nanoparticles were of 6 nm (in diameter), they were expected to block the 4 nm TMV channels and keep the drug in the confinement. Electron microscopy showed that very few Au nanoparticles could bind to both ends of the drug-encapsulated plant virus, unlike reported by Balci *et.al.* [9]. Figure

5.4.12 shows that in majority of the viral particles (with filled channels), Au particles are bound to only one end, but not to both ends. This could be explained by the fact that the citrate-coated Au nanoparticles bind to the RNA that dangles out at both ends of the TMV [9] but in this case either the TMV RNA was not exposed at both ends, or the drug bound to the RNA. Since we had mixed the drug as well as citrate-coated Au nanoparticles with TMV, it might be possible that the process of removing protein coats from both ends would be affected, resulting in exposing RNA mostly at one end of the virus. Yet another possibility is the known fact that both, cisplatin, can bind to RNA [197, 198] and hence the Au nanoparticles were not able to bind (as the drug would have already occupied its sites of interaction on the TMV).

b. The second strategy was designed based on the TMV decoration by citrate-coated Au nanoparticles in the presence of concentrated citric acid (see section 5.3.2.2 "*High Yield Binding of Au-Citrate Nanoparticle to TMV rods"* in chapter 5.3). TMV particles were encapsulated with the drug and purified via dialysis. The purified drug-encapsulated particles were then incubated with citrate-coated Au nanoparticles in the presence of concentrated aqueous citric acid. The aim was to encapsulate the drug inside the channels, followed by the decoration with Au nanoparticles on the exterior. In this way the channel would be blocked, too, and the drug might be kept inside the confinement. Figure 5.4.13 shows that drug-encapsulated TMV particles could not be decorated by the citrate-coated Au nanoparticles, and that most of them were washed out during purification. The TMV channels were clearly filled with Pt(II)-containing drug, but decorating them with Au nanoparticles did not occur. The drug binding to the exterior has somehow resulted in the loss of interaction between citrate-coated Au nanoparticles and the acidic amino acids residues on the exterior of TMV.

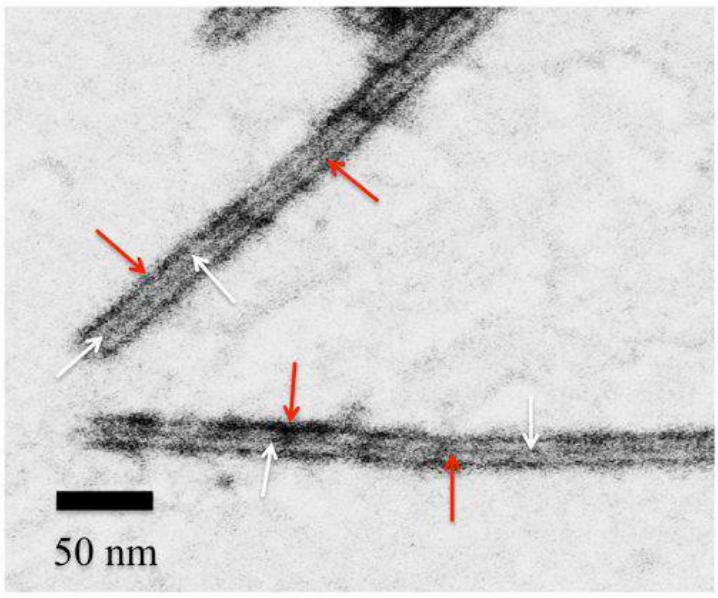

Figure 5.4.9. Inverted STEM image of TMV_{Lys} mutants encapsulated with oxaliplatin. TMV_{Lys} mutants did not show any difference to wild type particles and were encapsulated by the Pt(II)-containing drug. The dark appearing channel confirmed the presence of oxaliplatin in the TMV channel (shown by white arrows). The drug also binds to the exterior coat proteins of TMV (as shown by red arrows).

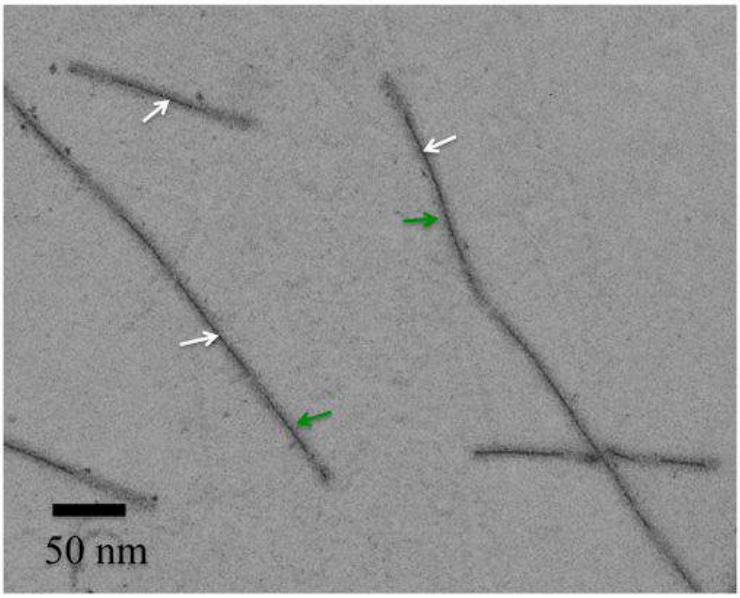

Figure 5.4.10. Inverted STEM image of pegylated TMV_{Lys} particles encapsulated with oxaliplatin. Oxaliplatin could only bind inside the channel (shown by white arrows) as confirmed by the dark appearance in the middle of (grey) TMV rods and no drug was bound on the exterior of TMV (shown by green arrows). This result was however not reproducible.

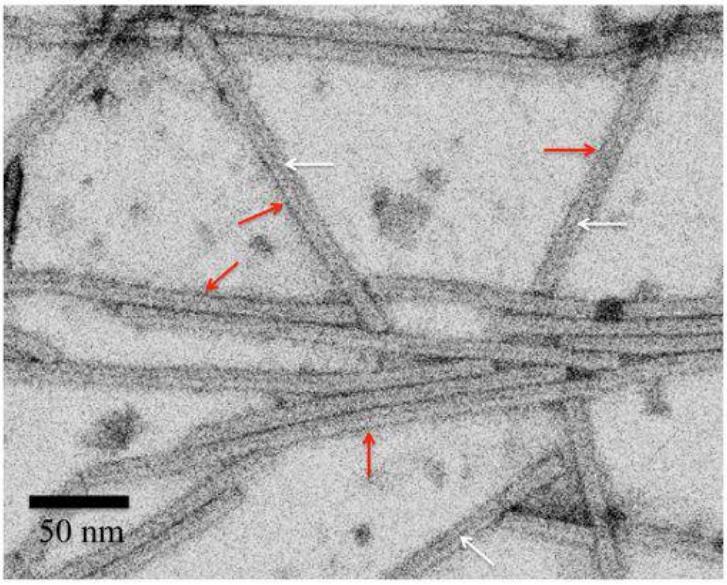

Figure 5.4.11. Inverted STEM image of pegylated TMV_{Lys} particles. Oxaliplatin did not only bind inside the channels (shown by white arrows) but also on the exterior coat proteins (shown by red arrows) like non-pegylated TMV particles.

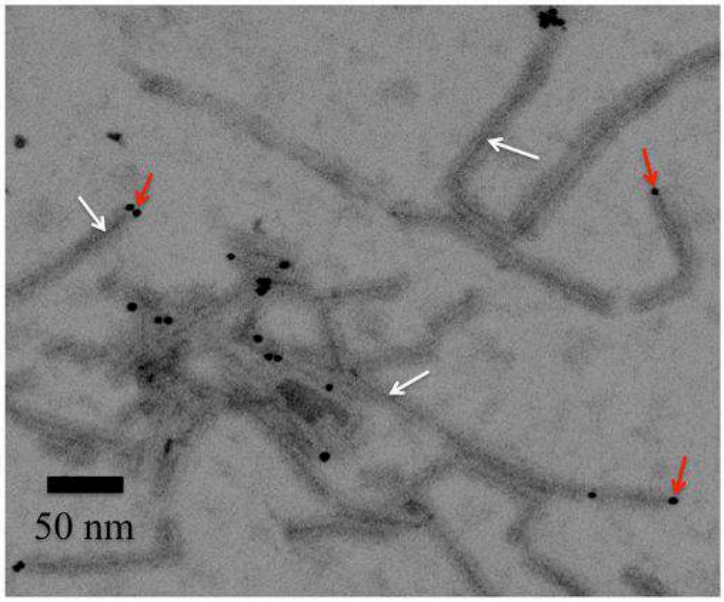

Figure 5.4.12. Inverted STEM image of cisplatin-encapsulated TMV particles with 6 nm citrate-coated Au nanoparticles. The drug filling inside the channel (shown by white arrows) and binding on the exterior coat proteins somehow did not allow the Au nanoparticle (black spheres shown by red arrows) to bind to both TMV (grey rods) ends.

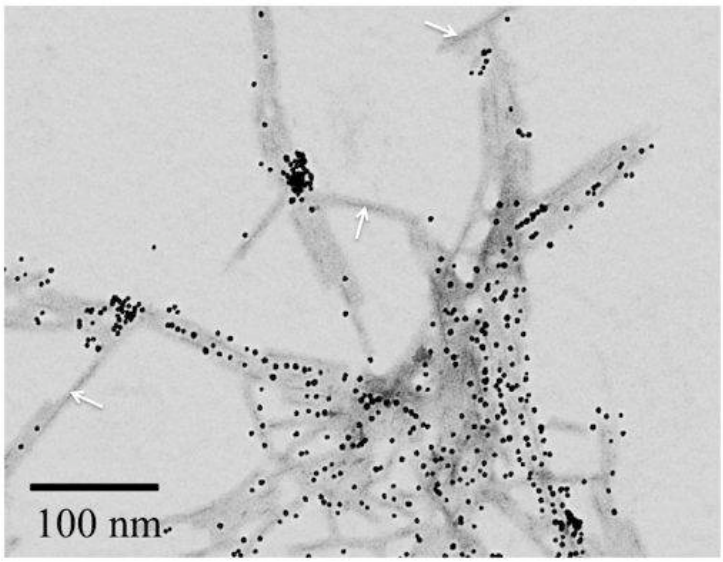

Figure 5.4.13. Inverted STEM image of oxaliplatin-encapsulated TMV particles (grey rods) could not be decorated by citrate-coated Au nanoparticles (black spheres) in the presence of aqueous citric acid. The TMV channels could still be seen filled with the Pt(II)-containing drugs (shown by white arrows).

5.4.6 Conclusion

The central 4 nm channel of TMV can be filled with a number of materials, e.g. metals and alloys. We took a step forward in this direction and filled TMV channels with cytostatic Pt(II)-containing drugs. The presence of the Pt(II)-containing drugs has been confirmed by electron microscopy and EDX spectroscopy. TMV particles with filled channels were identified and confirmed by their bright/dark contrast in electron microscopy imaging. So far it has been shown that deposition or confinement of materials/solutions in the channels is possible but we also prove the complete removal of the drugs after encapsulating them. It has also been proved that TMV can be modified and covalently functionalized, and then filled with Pt-complexes. The removal rate of substances (Pt drugs) of the exterior coat proteins and from inside of the channels varies and depends on the local interactions with the amino acids residues.

Summary and Future Outlook

Tobacco Mosaic Virus (TMV) is a rod-shaped RNA-containing virus that causes diseases in tobacco and other plants. TMV is basically a protein tube with a length of 300 nm, a diameter of 18 nm, and with an inner channel of 4 nm in diameter. The surfaces are highly polar and contain OH and COOH groups. TMV is stable in a wide range of pH values (<3 to >8.5). In this thesis TMV has been successfully exploited as a biological nanoscaffold for assemblies of inorganic materials in solution, i.e. metal (Ni, Au), metal oxide (iron oxide) and Pt(II)-containing drugs (cisplatin, oxaliplatin). Any deposition on the exterior coat proteins would attain a tube shaped morphology. For example, magnetic viral tubes synthesized during this thesis.

Ni metal is deposited on the exterior coat proteins of TMV through electroless deposition (ELD). The coating process is based on the adsorption of noble metal cations followed by autocatalytic electroless deposition. The magnetic properties and reproducibility of Ni deposition on TMV have been investigated along with the effect of the addition of surfactants during the process of ELD. The ELD is based on Pd nucleation sites in the presence of phosphate buffer bound to the exterior of virions. The ELD process has also been investigated in real time by Dynamic Light Scattering (DLS) that proves the rapid reduction of Ni^{2+} ions to the metallic state on TMV. In future, more emphasis can be put on controlling the (rate of the) ELD reaction (i.e. slowing it down or poisoning it), for achieving different morphological features. Moreover, the stability of metallized viruses can also improved by wrapping the viral particles in a (polymer) sheath. Depending on the type and properties of the polymer, it can also find applications in spin-transport and memory recording nanodevices as nanoscale magnetic wires. Finally, the severe degree of aggregation of TMVs during metallization should be studied and strategies devised to avoid it during metallization.

TMV tubes have been mineralized with iron oxide using a wet chemical method at ambient temperature. Mineralized TMV tubes have been characterized in a great detail in terms of morphology, crystallinity, magnetic properties, and chemical nature (of the iron oxide). TMV iron oxide nanotubes are successfully synthesized by mineralizing the

deprotonated viral coat proteins at neutral pH values. The synthesized iron oxide is found to be amorphous, but it can be annealed and transformed to crystalline phase by thermal treatment, which does not destroy its tubular shape and also improves the magnetic moment of the iron oxide nanotubes significantly. The crisscross arrangement of TMVs is based on interlinking during the synthesis. It could be avoided by different chemical agents such as surfactants etc. It is also desirable to produce mineralized viruses with higher magnetic moment, and to analyse them for their hyperthermia and ferrofluidic abilities. (Hyperthermia is the heat generation by magnetic nanoparticles to kill cancer cells when an external alternating magnetic field is applied). Ferrofluids are suspensions of magnetic nanoparticles in a fluid; they combine magnetic properties of the nanoparticles and fluid properties of the liquid carrier.

Metallic and metal oxide nanoparticles can also be attached to the exterior protein surface of TMV. Citrate-coated Au and iron oxide nanoparticles have been bound to TMV resulting in the decoration of viral rods. The assembly of these nanoparticles depends on the electrostatic and van der Waals (vdW) interaction between the negatively charged nanoparticles and the protonated positively charged acidic amino acids. Exchanging citrate to neutral 2-mercaptoethanol, or attempting Au or iron oxide binding at pH 5-8 has not resulted in nanoparticle binding to TMVs. Future works may include the synthesis of highly magnetic iron oxide nanoparticles and their binding to TMV, which can find applications in ferrofluids, hyperthermia and magnetic drug delivery (the selective delivery of drug containing nanoscaffolds, tagged with magnetic nanoparticles, to tumors by an application of a magnetic field gradient). Similarly the Au-decorated TMV particles can be a useful addition to the already existing biosensing nanodevices for molecular recognition, chemical sensing and imaging. Further investigation can show what other types of nanoparticles can be attached to TMV. It is concluded from our results that all nanoparticles with citrate shells will qualify.

It is well-known that the 4 nm wide channel can be filled with metals. In this work the viral channel has been successfully filled with Pt(II)-containing anticancer drugs without producing metallic Pt. The work aims for exploiting non-pathogenic nanotubes as a nanocarrier for drug delivery against cancers. The confined drugs also effuse from the channels by dialysis against water. Different from the well-known deposition of materials inside the channels, here the effusion after confinement of the Pt(II)-

containing drugs is also shown. The extension of these studies may open new roads into biomedical science in the therapy of cancers. Most important questions to be answered remain the quantification of the encapsulated drug, and if the drug is still potent after being released from the protein cage of TMV. *In vitro* cell cultures followed by toxicity assays and fluorescent microscopy can give answers to some of these important questions. Moreover, the combination of drug confinement with magnetic nanoparticle decoration will open the possibilities of magnetically induced selective drug delivery.

TMV's versatile chemical nature, tough physical properties, non-pathogenic nature and ease of handling and storage make it an ideal nanoscale biotemplate for the synthesis of a variety of nanoarchitectures. Future research works will uncover better implementation of TMV as a bionanoscaffold for nanofabrication in nanoscale science and technology.

Bibliography

1. Stubbs, G. *Semin. Virol.* **1990,** 1, 405-412.

2. Van Regenmortel, M. H. *Phil. Trans. Royal Soc. London B, Biol. Sci.* **1999,** 354, 559-568.

3. Schlick, T. L., Ding, Z., Kovacs, E. W., Francis, M. B. *J. Am. Chem. Soc.* **2005,** 127(11), 3718-3723.

4. Wu, Z., Mueller, A., Degenhard, S., Ruff, S. E., Geiger, F., Bittner, A. M., Wege, C., Krill, C. E. *ACS Nano* **2010,** 4(8), 4531-4538.

5. Lim, J.-S., Kim, S.-M., Lee, S.-Y., Stach, E. A., Culver, J. N., Harris, M. T. *J. Nanomat.* **2010,** Article ID 620505, 6 pages.

6. Knez, M., Sumser, M., Bittner, A. M., Wege, C., Jeske, H., Martin, T. P., Kern, K. *Adv. Func. Mater.* **2004,** 14, 116-124.

7. Knez, M., Bittner, A. M., Boes, F., Wege, C., Jeske, H., Mai, E., Kern, K. *Nanolett.* **2003,** 3(8), 1079-1082.

8. Tsukamoto, R., Muraoka, M., Seki, M., Tabata, H., Yamashita, I. *Chem. Mater.* **2007,** 19, 2389-2391.

9. Balci, S., Noda, K., Bittner, A. M., Kadri, A., Wege, C., Jeske, H., Kern, K. *Ange. Chem. (Int. Ed.)* **2007,** 46, 3149-3151.

10. Wu, Z., Zierold, R., Mueller, A., Ruff, S. E., Ma, C., Khan, A. A., Geiger, F., Sommer, B. A., Knez, M., Nielsch, K., Bittner, A. M., Wege, C., Krill, C. E. *Phys. Stat. Solid. (B)* **2010,** 247, 2412-2423.

11. Nishiguchi, M., Motoyoshi, F., Oshima, N. *J. Gen. Virol.* **1978,** 39, 53-61.

12. Bittner, A.M., Alonso, J.M., Wege, C., *Physical Virology (in preparation)*. Springer, 2012.

13. Hull, R., *Matthew's Plant Virology*. Elesvier Publications, (San Diego, California), 2011.

14. Klug, A. *Phil. Trans. Royal Soc. London B, Biol. Sci.* **1999,** 354, 531-535.

15. Zaitlin, M. *Phil. Trans. Royal Soc. London B, Biol. Sci.* **1999,** 354, 587-591.

16. Butler, P. *J. Gen. Virol.* **1984**, 65, 253-279.

17. Stubbs, G. *Phil. Trans. Royal Soc. London B, Biol. Sci.* **1999,** 354, 551-557.

18. Gallagher, W. H., Lauffer, M. A. *J. Mol. Biol.* **1983,** 170(4), 905-919.

19. Namba, K., Pattanayek, R., Stubbs, G. *J. Mol. Biol.* **1989,** 208(2), 307-325.

20. Kausche, G. *Biol. Zbl.* **1940,** 60, 179-199.

21. Shenton, B. W., Douglas, T., Young, M., Stubbs, G., Mann, S. *Adv. Mater.* **1999,** 11, 253-256.

22. Fraenkel-Conrat, H., Wilhelm, C. *Proc. Nat. Acad. Sci. USA* **1955,** 41, 690-698.

23. Lee, S.-Y., Royston, E., Culver, J. N., Harris, M. T. *Nanotech.* **2005,** 16, S435-S441.

24. Dujardin, E., Peet, C., Stubbs, G., Culver, J. N., Mann, S. *Nanolett.* **2003,** 3, 413-417.

25. Kobayashi, M., Seki, M., Tabata, H., Watanabe, Y., Yamashita, I. *Nanolett.* **2010,** 10, 773-776.

26. Atanasova, P., Rothenstein, D., Schneider, J. J., Hoffmann, R. C., Dilfer, S., Eiben, S., Wege, C., Jeske, H., Bill, J. *Adv. Mater.* **2011,** 23, 4918-4922.

27. Chen, X., Gerasopoulos, K., Guo, J., Brown, A., Wang, C., Ghodssi, R., Culver, J. N. *ACS Nano* **2010,** 4, 5366-5372.

28. Niu, Z., Liu, J., Lee, L. A., Bruckman, M. A., Zhao, D., Koley, G., Wang, Q. *Nanolett.* **2007,** 7, 3729-3733.

29. Reedijk, J. *Eur. J. Inorg. Chem.* **2009,** 10, 1303-1312.

30. Desoize, B., Madoulet, C. *Crit. Rev. Oncology/Hemat.* **2002,** 42, 317-325.

31. Esteban-Fernández, D., Moreno-Gordaliza, E., Cañas, B., Palacios, M. A., Gómez-Gómez, M. M. *Metallomics:Integ. Biomet. Sci.* **2010,** 2, 19-38.

32. Alberts, D. S., Robert, T. *Oncologist* **1998,** 3, 15-34.

33. Graham, M. A., Lockwood, G. F., Greenslade, D., Graham, M. A., Greenslade, D., Brienza, S., Bayssas, M., Gamelin, E. *Clin. Canc. Res.* **2000,** 6, 1205-1218.

34. Rebecca, A., Mattew, D., Trevor, W. *J. Chem. Edu.* **2006,** 83(5), 728-734.

35. Kostova, I. *Rec. Pat. Anti-canc. Drug Discov.* **2006,** 1, 1-22.

36. Raymond, E., Faivre, S., Wovnarowski, J., Chaney, S. *Seminal. Oncol.* **1998,** 25(2), 4-12.

37. Shereen, M., Michael, L. A. *Analyt. Bioanalyt. Chem.* **2008,** 392(5), 819-830.

38. Alama, A., Tasso, B., Novelli, F., Sparatore, F. *Drug Discov. Today* **2009,** 14(9-10), 500-508.

39. Fuertes, M. A., Alonso, C., Perez, J. M. *Chem. Rev.* **2003,** 103(3), 645-662.

40. Sanz Miguel, P. J., Roitzsch, M., Yin, L., Lax, P. M., Holland, L., Krizanovic, O., Lutterbeck, M., Schurmann, M., Fusch, E. C., Lippert, B. *Dalt. Trans.* **2009**, (48), 10774-10786.

41. Kelland, L. R. *Drugs* **2000,** 59(Suppl 4), 1-8.

42. Wilkinson, J. *Device Technol.* **2003,** 14(5), 29-31.

43. Kumar, A., Gupta, M. *Bioinorg. Chem. Appl.* **2005,** 26, 3995-4021.

44. Grau-Crespo, R., Al-Baitai, A. Y., Saadoune, I., De Leeuw, N. H. *J. Phys. Cond. Mat.* **2010,** 22, 255401 (7 pages).

45. William, D. C. J., David, G. R., *Fundamentals of Materials Science and Engineering. An Integrated Approach.* John Wiley & Sons, Inc. (Asian Edition) 2008.

46. Sanjay, S., Richard, B. F., David, D. S., Joseph, D. F. J. *Am. J. Roent.* **1987,** 150, 735-743.

47. Gilchrist, R. K., Medal, R., Shorey, W.D., Hanselan, R.C., Parrot, J.C., Taylor, C.B. *Ann. Surg.* **1957,** 146, 596-606.

48. Schwertmann, U., Cornell, R. M., *The iron oxides: structure, properties, reactions, occurrences and uses*. Wiley-Vch GmbH & Co. KGaA: Darmstadt, Germany, 2006.

49. Pankhurst, Q., Conolly, J., Jones, S., Dobson, J. *J. Phys. D: Appl. Phys.* **2003,** 167(36), R167-R181.

50. Mosbach, K., Schroder, U. *FEBS Lett.* **1979,** 102, 112-116.

51. Alexiou, C., Arnold, W., Klein, R.J., Parak, F.G., Hulin, P., Beregeman, C., Erhardt, W., Wagenpfeil, S., Lubb, A.S. *Canc. Res.* **2000,** 60, 6641-6648.

52. Scherer, F., Anton, M., Schillinger, U., Henke, J., Beregemann, C., Kruger, A., Gansbacher, B. Planck C. *Gen. Ther.* **2002,** 9, 102-109.

53. Johnson, G.A., Benveniste, H., Black, R.D., Hedlund, L.W., Maronpot, R.R., Smith, B.R. *Mag. Reson.* **1993,** Q9, 1–30.

54. Lewin, M., Carlesso, N., Tung, C-H., Tang, X-W., Cory, D., Scadden, T., Weissleder, R. *Nat. Biotechnol.* **2000,** 18, 410-414.

55. Weissleder, R., Moore, A., Mahmood, U., Bhorade, R., Benveniste, H., Chiocca, E., Basilion, J.B. *Nat. Med.* **2000,** 6, 351-355.

56. Zhao, M., Beauregard, D.A., Loizou, L., Davletov, B., Brindle, K.M. *Nat. Med.* **2001,** 7, 1241-1244.

57. Phillips, J. L. *JOSHUA* **2005,** 3, 14-18.

58. Hergt, R., Andr, W., Ambly, C. G., Hilger, I., Kaiser, W. A., Richter, U., Schmidt, H.-G. *IEEE Trans. Magnet.* **1998,** 34, 3745-3754.

59. Heider, F., Dunlop, D.J., Suguira, N. *Science* **1987,** 236, 1287-1290.

60. Shliomis, M. *Sov. Phys.–Usp.* **1963,** 17, 153-184.

61. Maier-Hauff, K., Ulrich, F., Nestler, D., Niehoff, H., Wust, P., Thiesen, B., Orawa, H., Budach, V., Jordan, A. *J. Neurooncol.* **2011,** 103, 317-24.

62. Nguyen, H.N., Hervy, E.A., Janicek, M. *Cancer* **1994,** 74(2), 545-555.

63. Bovicelli, A., Giuseppina, D.A., Giordano, A. *J. Cellul. Phys.* **2011,** 226, 2500-2504.

64. Cannistra, S.A., McGuire, W.P. *J. Clin. Oncol.* **2007,** 25(20), 2865-2866.

65. Duncan, T.J., Al-Attar, A., Rolland, P., Harper, S., Spendlove, I., Durrant, L.G. *Int. J. Gynecol. Pathol.* **2010,** 29, 8-18.

66. Wang, Y., Cheng, C., Ji, Y., Zhao, Y., Zou, L., Shen, A. *J. Canc. Res C.lin. Oncol.* **2009,** 135, 951-959.

67. De Meyer, T., Bijismans, I.T., Van der Vijver, K.K., Bakaert, S., Oosting, J., Van, C.W., van Engeland, W., Sieben, N.L. *J. Pathol.* **2009,** 217, 14-20.

68. Imam, J.S., Buddavararpu, K., Lee-Chang, J.S., Ganapathy, S., Camosy, C., Chen, Y., Rao, M.K. *Oncogen.* **2010,** 29, 4971-4979.

69. Kothandaraman, N., Bajic, V. B., Brendan, P. N., Huak, C. Y., Keow, P. B., Razvi, K., Salto-Tellez, M., Choolani, M. *BMC Canc.* **2010,** 10, 64 (13 pages).

70. Moore, R. G., MacLaughlan, S., Bast, R. C., Jr. *Gynec. Oncol.* **2010,** 116(2), 240-245.

71. Moore, R. G., McMeekin, D. S., Brown, A. K., DiSilvestro, P., Miller, M. C., Allard, W. J., Gajewski, W., Kurman, R., Bast, R. C., Jr. Skates, S. J. *Gynec. Oncol.* **2009,** 112(1), 40-46.

72. Yang, N., Kaur, S., Volinia, S., Greshock, J., Lassus, H., Hasegawa, K., Liang, S., Leminen, A., Deng, S., Smith, L., Johnstone, C. N., Chen, X. M., Liu, C. G., Huang, Q., Katsaros, D., Calin, G. A., Weber, B. L., Butzow, R., Croce, C. M., Coukos, G., Zhang, L. *Canc. Res.* **2008,** 68(24), 10307-10314.

73. Rose, P. G. *Oncologist* **2005,** 10(3), 205-214.

74. Bittner, A.M. in Advanced nanoscale ULSI interconnects: fundamentals and application, Y. S., Tetsuya O, Madhav D, Takayuki O (eds). *"Electroless deposition approaching the molecular scale"*. Springer Science (New York, Dordrecht, Heidelberg, London), **2009**.

75. Paunovic, M., Mordechay, S. *Fundamentals of electrochemical deposition.* Wiley Interscience (New York, Chicester, Weinheim, Brisbane, Singapore, Toronto), **1996.**

76. Mordechay, S., Paunovic, M. *Modern electroplating.* Wiley Interscience (New York, Chicester, Weinheim, Brisbane, Singapore, Toronto), **2001.**

77. Paunovic, M., Mordechay, S., *Fundamentals of Electrochemical Deposition.* Wiley Interscience (USA), Vol. 88, **2006.**

78. Hadju, G.M. *Electroless plating: Fundamentals and applications.* American Electroplaters and Surface Finishers Society Orland, FL.: USA, **1990.**

79. Molenaar, A. *J. Electrochem. Soc.* **1982,** 129, 1917-1921.

80. Weber, C., *In-situ scanning tunneling microscopy study of morphological and mechanistic aspects of electroless copper deposition.* The Pennsylvania State University, University Park, PA. : USA, **1998.**

81. Porter, M. D., Bright, T. B., Allara, D. L., Chidsey, C. E. D. *J. Am.Chem. Soc.* **1987,** 109, 3559–3568.

82. Whitesides, G. M., Laibinis, P. E. *Langmuir* **1990,** 6(1), 87–96.

83. Meerakker, J. E. A. M. *J.Appl. Electrochem.* **1981,** 11(3), 395-400.

84. Kind., H. Patterning of surfaces by locally analyzed chemical reactions. Ph.D Thesis. University of Laussane, Lausanne, **2000.**

85. Andricacos, P. C. C.-C. T. E. S. I., Spring, 32, **1999.**

86. Pohl, K., Stierhof, Y. D. *Microsc. Res. Tech.* **1998,** 42(1), 59-65.

87. Baschong, W., Stierhof, Y. D. *Microsc. Res. Tech.* **1998,** 42(1), 66-79.

88. Mertig, M., Kirsch, R., Pompe, W., Engelhardt, H. *Eur. Phys. J. D-Atom. Mol. Opt. Plasm. Phys.* **1999,** 9(1-4), 45-48.

89. Edelstein, A.S., Cammarata, R.C. (eds.), *Nanomaterials: Synthesis, properties and applications,*. Institute of physics phblishing: Bristol, Philadelphia.: USA, **1996.**

90. Van der Putten, A., de Bakker, J.W. *J. Electrochem. Soc.* **1993,** 140, 2229-2235.

91. Yong, L., Shengtao, Z., Robert, D. *Particuology* **2012,** *Article in press.*

92. Kulyk, N., Cherevko, S., Chung, C.-H. *Electrochim. Acta* **2012,** 59, 179-185.

93. Graham, C. D. *J. Mater. Sci. Tech.* **2000,** 16, 97-101.

94. Rao, B.P.C., Jayakumar, T., Baldev, R., Arnold, W. *J. Nondes. Evaluat.* **2001,** 21(1), 38-43.

95. Gallop., J. C., *SQUIDs, The Josephson Effects and Superconducting Electronics.* Taylor & Francis Group, **1991.**

96. Donaldson, G.B., Clarke, J., McFarlane, J.C. in Conise Encyc. Of Magn. And Supercond. Materials, (ed.) J. Evetts. *"SQUID design, fabrication and application"*. Pergamon Press, Oxford, UK, **1992.**

97. Rohlf, J. W., *Modern Physics from alpha to Z0*. John Wiley & Sons, **1994.**

98. Clarke, J. *Sci. Amer.* **1994,** 271(2), 46-53.

99. MPMS SQUID-VSM. User Manual. *Quantum Design*.

100. Plaster., B. R. Dynamic light scattering and diffusing wave spectroscopy studies of the microscopic dynamics of polystyrene latex spheres suspended in glycerol. Ph.D Thesis. Massachussets Institute of Technology, **1999.**

101. Nobbmann, U., Connah, M., Fish, B., Varley, P., Gee, C., Mulot, S., Chen, J., Zhou, L., Lu, Y., Shen, F., Yi, J., Harding, S. E. *Biotech. Gen. Eng .Rev.* **2007,** 24, 117-128.

102. Berne, B., Pecora, R., *Dynamic Light Scattering with Applications to Biology, Chemistry and Physics.* Wiley Interscience: Mineola, New York, **1976.**

103. Pirie., A. D. A light scattering study of colloid-plyer mixtures. Ph.D Thesis. University of Edinburgh, **1995.**

104. Technical Note. Dynamic Light Scattering. *www.malevern.com*.

105. Kirby, B. J., Hasselbrink, E. F., Jr. *Electrophoresis* **2004,** 25(2), 187-202.

106. Zeta Potential. Technical Note. Zeta Meter Inc., USA. *http://www.zeta-meter.com/*.

107. Technical Note. Zeta Potential in 30 minutes. *www.malevern.com*.

108. Yeh, Y., Cummins, H.Z. *Appl. Phys. Lett.* **1964**, 176-178.

109. Durst, F., Melling, A., Whitelaw, J. H., *Principles and Practice of Laser Doppler Anemometry*. Academic Press: London, **1976.**

110. Williams, D. B., Carter., C. B., *Transmission Electron Microscopy. A Textbook for Materials Science.* Springer Science+Business Media, Inc., **1996.**

111. Haguenau, F., Hawkes, P. W., Hutchison, J. L., Satiat-Jeunemaitre, B., Simon, G. T., Williams, D. B. *Microsc. Microanal.:Off. J. Microsc. Soc. Am., Microbeam Analy. Soc., Microsc. Soc. Canada* **2003,** 9(2), 96-138.

112. Wu, Z. Preparataion and characterization of nanotube ferrofluids by template-directed methods. Ph.D Thesis. Ulm University, **2011.**

113. Egerton., R. F., *Physical principles of electron microscopy: an introduction to TEM, SEM, and AEM.*. Springer Science+Business Media, LLC, **2008.**

114. Vernon-Parry, K. D. *III-Vs Review* **2000,** 13(4), 40-44.

115. Pennycook, S., Lupini, A., Varela, M., Borisevich, A., Pen, Y., Oxley, M., Benthem, K. V., Chisholm, M., Scanning Transmission Electron Microscopy for Nanostructure Characterization. In *Scanning microscopy for Nanotechnology: techniques and applications*, Zhou, W., Wang, Z. L., Eds. Springer, b

116. Goldstein, J., Newbury, D. E., Joy, D. C., Lyman, C. E., Patrick, E., Eric, L., Linda, S., Joseph, M., *Scanning Electron Microscopy and X-Ray Microanalysis.* . Springer, 2**003.**

117. Devash, Y., Hauschner, A., Sela, I., Chakraburtty, K. *Virology* **1981,** 11(1), 103-112.

118. Lin, S., Li, M., Dujardin, E., Girard, C., Mann, S. *Adv. Mater.* **2005,** 17, 2553-2559.

119. Geiger, F.C. Tabakmosaikvirus-Hüllproteinvarianten als Bausteine für die Nano- und Arraytechnologie. Ph.D Thesis. Institute of Biology, Stuttgart University, **2009.**

120. Hiergeist, R., Andra, W., Buske, N., Hergt, R., Hilger, I., Richter, U., Kaiser, W. *J. Mag. Magn. Mater.* **1999,** 201, 420-422.

121. Moroz, P., Jones, S. K., Winter, J., Gray, B. N. *J. Sur. Oncol.* **2001,** 78, 22-9, discussion 30-1.

122. Kind, H., Bittner, A. M., Cavalleri, O., Klaus Kern, Greber, T. *J. Phys. Chem. B* **1998,** 102, (39), 7582-7589.

123. Demir, M., Stowell, M. H. B. *Nanotechnology* **2002,** 13, 541-544.

124. Balci, S. Metal and Metaloxide Nanostructures on and in Plant Viruses. Laussane University, Switzerland, **2006.**

125. Santos, N. C., Castanho, M. A. *Biophy. J.* **1996,** 71, 1641-50.

126. Sinn, I., Kinnunen, P., Pei, S. N., Clarke, R., McNaughton, B. H., Kopelman, R. *Appl. Phys. Lett.* **2011,** 98, 024101.

127. Singamaneni, S., Bliznyuk, V. *Appl. Phys. Lett.* **2005,** 87, 162511.

128. Sun, X.-C., Dong, X.-L. *Mater. Res. Bullet.* **2002,** 37(5), 991-1004.

129. Johnston-Peck, A. C., Wang, J., Tracy, J. B. *ACS Nano* **2009,** 3(5), 1077–1084.

130. Wang, Y., Yang, H. *Chem. Eng. J.* **2009,** 147, 71-78.

131. Almeida, T. P., Fay, M. W., Zhu, Y., Brown, P. D. *Nanoscale* **2010,** 2, 2390.

132. Merchan-Merchan, W., Saveliev, a. V., Taylor, a. M. *Nanotechnology* **2008,** 19, 125605.

133. Morber, J. R., Ding, Y., Haluska, M. S., Li, Y., Liu, J. P., Wang, Z. L., Snyder, R. L. *J. Phys. Chem. B* **2006,** 110, 21672-21679.

134. Wu, P.-C., Wang, W.-S., Huang, Y.-T., Sheu, H.-S., Lo, Y.-W., Tsai, T.-L., Shieh, D.-B., Yeh, C.-S. *Chemistry* **2007,** 13, 3878-3885.

135. Wu, M.-S., Ou, Y.-H., Lin, Y.-P. *Electrochim. Acta* **2010,** 55, 3240-3244.

136. Kumar, R. V., Koltypin, Y. *J. Appl. Phys.* **2001,** 89, 6324-6328.

137. Bødker, F., Hansen, M. F. *Phys. Rev. B* **2000,** 61, 6826–6838.

138. Kim, C. H., Chun, H. J., Kim, D. S., Kim, S. Y., Park, J., Moon, J. Y., Lee, G., Yoon, J., Jo, Y., Jung, M.-H., Jung, S. I., Lee, C. J. *Appl. Phys. Lett.* **2006,** 89, 223103 (3 pages).

139. Meng Lin, M., Kim, H.-H., Kim, H., Muhammed, M., Kyung Kim, D. *Nano Rev.* **2010,** 1, 1-20.

140. Tai, Y., Wang, L., Yan, G., Gao, J.-m., Yu, H., Zhang, L. *Pol. Inter.* **2011,** 60(7), 976-994.

141. Górzny, M. Ł., Walton, A. S., Evans, S. D. *Adv. Fun. Mater.* **2010,** 20(8), 1295-1300.

142. Bromley, K. M., Patil, A. J., Perriman, A. W., Stubbs, G., Mann, S. *J. Mater. Chem.* **2008,** 18, 4796-4801.

143. Royston, E., Ghosh, A., Kofinas, P., Harris, M. T., Culver, J. N. *Langmuir* **2008,** 24(3), 906–912.

144. Balci, S., Bittner, A. M., Schirra, M., Thonke, K., Sauer, R., Hahn, K., Kadri, A., Wege, C., Jeske, H., Kern, K. *Electrochim. Acta* **2009,** 54, 5149-5154.

145. Fujikawa, S., Kunitake, T. *Langmuir* **2003,** 19(16), 6545–6552.

146. Balci, S., Leinberger, D. M., Knez, M., Bittner, A. M., Boes, F., Kadri, A., Wege, C., Jeske, H., Kern, K. *Adv. Mat.* **2008,** 20, 2195–2200.

147. Manceau, A., Gates, W. P. *Clays and Clay Min.* **1997,** 45, 448-460.

148. Zhang, Y. C., Tang, J. Y., Hu, X. Y. *J. Alloys Comp.* **2008,** 462, (1-2), 24-28.

149. Lu, H.M., Zheng, W.T., Jiang, Q. *J. Phys. D: Appl. Phys.* **2007,** 40(2), 320-325.

150. Qu, X., Kobayashi, N., Komatsu, T. *ACS nano* **2010,** 4(4), 1732-1738.

151. Bachmann, J., Escrig, J., Pitzschel, K., Moreno, J. M. M., Jing, J., Görlitz, D., Altbir, D., Nielsch, K. *J Appl. Phys.* **2009,** 105, 07B521-1 - 07B521-3.

152. Suber, L., Imperatori, P., Ausanio, G., Fabbri, F., Hofmeister, H. *J. Phys. Chem. B* **2005,** 109, 7103-7109.

153. Geng, B., Zhan, F., Jiang, H., Guo, Y., Xing, Z. *Chem. Comm.* **2008**, 5773-5775.

154. Zhou, S.-M., Zhang, X.-T., Gong, H.-C., Zhang, B., Wu, Z.-S., Du, Z.-L., Wu, S.-X. *J. Phys.: Cond. Mat.* **2008,** 20, 075217.

155. Han, Q., Liu, Z., Xu, Y., Chen, Z., Wang, T., Zhang, H. *J. Phys. Chem. C* **2007,** 111(13), 5034-5038.

156. B. Y. Geng1, J. Z. M., X. W. Liu1, Q. B. Du1, M. G. Kong2, and L. D. Zhang. *Appl. Phys. Lett.* **2007,** 90(4), 043120 (3 pages).

157. Wan, J., Yao, Y., Tang, G. *Appl. Phys. A: Mater. Sci. Proc.* **2007,** 89, (2), 529-532.

158. Park, S.-J., Kim, S., Lee, S., Khim, Z. G., Char, K., Hyeon, T. *J. Am. Chem. Soc.* **2000,** 122(35), 8581-8582.

159. Palchik, O., Felner, I., Kataby, G., Gedanken, A. *J. Mater. Res.* **2011,** 15, 2176-2181.

160. X. Cao, R. P., Yu. Koltypin, G. Kataby, I. Felner and A. Gedanken. *J. Mater. Res.* **1997,** 12, 402-406.

161. Liao, X., Zhu, J., Zhong, W., Chen, H.-Y. *Mater. Lett.* **2001,** 50, 341-346.

162. P Ayyub, M. M., M Barma, V R Palkar and R Vijayaraghavan. *J. Phys. C: Solid Stat. Phys.* **1988,** 21(11), 2229-2246.

163. Trudel, S., Crozier, E. D., Gordon, R. A., Budnik, P. S., Hill, R. H. *J. Sol. Stat. Chem.* **2011,** 184(5), 1025-1035.

164. Kanngießera, B., Hahnb, O., Wilkec, M., Nekatc, B., Malzera, W., Erkod, A. *Spect. Acta B: Atom. Spectro.* **2004,** 59(10-11), 1511–1516.

165. Ballirano, P., Belardi, G. *Acta Cryst.* **2006,** E62, i58-i60.

166. Braun, E., Eichen, Y., Sivan, U., Ben-Yoseph, G. *Nature* **1998,** 391, 775-778.

167. Behrens, S., Rahn, K., Habicht, W., Böhm, K.-J., Rösner, H., Dinjus, E., Unger, E. *Adv. Mater.* **2002,** 14(22), 1621-1625.

168. Seddon, A. M., Patel, H. M., Burkett, S. L., Mann, S. *Ang. Chem. (Int. Ed.)* **2002,** 41(16), 2988–2991.

169. Hall, S. R. *Adv. Mater.* **2006,** 18(4), 487–490.

170. Jans, H., Huo, Q. *Chem. Soc. Rev.* **2012,** 41, 2849-2866.

171. Turkevich, J., Stevenson, P. C., Hillier, J. *Discuss. Faraday. Soc.* **1951,** 11, 55-75.

172. Giljohann, D. a., Seferos, D. S., Daniel, W. L., Massich, M. D., Patel, P. C., Mirkin, C. a. *Ang. Chem. (Int. Ed.)* **2010,** 49, 3280-94.

173. Bittner, A. M., Heber, F., Hamaekers, J. *Surf. Sci.* **2009,** 603(10-12), 1922-1925.

174. Mudunkotuwa, I. A., Grassian, V. H. *J. Am. Chem. Soc.* **2010,** 132, 14986-94.

175. Gabizon, A., Tzemach, D., Gorin, J., Mak, L., Amitay, Y., Shmeeda, H., Zalipsky, S. *Canc. Chem. Pharm.* **2010,** 66, 43-52.

176. Strassert, C. A., Otter, M., Albuquerque, R. Q., Hone, A., Vida, Y., Maier, B., De Cola, L. *Ang. Chem. (Int. Ed.)* **2009,** 48, (42), 7928-31.

177. Tobias, G., Ballesteros, B., Green, M. L. H. *Phy. Stat. Sol. C* **2010,** 7, 2739-2742.

178. Tan, S., Brisson, Â. A., Dupuis, Â. V., Sandre, O. O., Miraux, S., Thiaudi, E., Al, S. E. T. *ACS Nano* **2011,** 5, 1122-1140.

179. Luciani, N., Wilhelm, C., Gazeau, F. *Biomater.* **2010,** 31, 7061-7069.

180. Lockney, D. M., Guenther, R. N., Loo, L., Overton, W., Antonelli, R., Clark, J., Hu, M., Luft, C., Lommel, S. A., Franzen, S. *Bioconj. Chem.* **2011,** 22(1), 67-73.

181. Cvitkovic, E., Bekradda, M. *Semin. Oncol.* **1999,** 26(6), 647-62.

182. Zhao, Y.-Y., Mandal, R., Li, X.-F. *Rap.Comm. Mass Spect.* **2005,** 19, 1956-1962.

183. Arnesano, F., Natile, G. *Pure Appl. Chem.* **2008,** 80, 2715-2725.

184. Li, H., Zhao, Y., Phillips, H. I. a., Qi, Y., Lin, T.-Y., Sadler, P. J., O'Connor, P. B. *Anal. Chem.* **2011,** 83, 5369-5376.

185. Ivanov, a. I., Christodoulou, J., Parkinson, J. a., Barnham, K. J., Tucker, A., Woodrow, J., Sadler, P. J. *J. Biol. Chem.* **1998,** 273, 14721-14730.

186. Neault, J. F., Tajmir-Riahi, H. A. *Biochim. Biophys. Acta* **1998,** 1384, 153-159.

187. Robins, A. B. *Chem. Biol. Inter.* **1982,** 38, 349-356.

188. Heudi, O., Cailleux, A., Allain, P. *J. Inorg. Biochem.* **1998,** 71, 61-69.

189. Lemma, T., Pawliszyn, J. *J. Pharm. Biomed. Anal.* **2009,** 50, 570-575.

190. Mandal, R., Kalke, R., Li, X.-F. *Chem. Res. Toxicol.* **2004,** 17, 1391-1397.

191. Hahn, M., Kleine, M., Sheldrick, W. *J. Biol. Inorg. Chem.* **2001,** 6, 556-566.

192. Molineux, G. *Canc. Treat. Rev.* **2002,** 28, 13-16.

193. Fujiyama, K., Saejung, W., Yanagihara, I., Nakado, J., Misaki, R., Honda, T., Watanabe, Y., Seki, T. *J. Biosci. Bioeng.* **2006,** 101, 398-402.

194. McCormick, A. a., Corbo, T. a., Wykoff-Clary, S., Nguyen, L. V., Smith, M. L., Palmer, K. E., Pogue, G. P. *Vaccine* **2006,** 24, 6414-6423.

195. Palmer, K. E., Benko, A., Doucette, S. a., Cameron, T. I., Foster, T., Hanley, K. M., McCormick, A. a., McCulloch, M., Pogue, G. P., Smith, M. L., Christensen, N. D. *Vaccine* **2006,** 24, 5516-5525.

196. Strobel, G. *Eur. J. Immu.* **1974,** 4, (9), 621-626.

197. Hostetter, A. A., Osborn, M. F., DeRose, V. J. *ACS Chem. Biol.* **2012,** 7, 218-225.

198. Boer, J., Blount, K. F., Luedtke, N. W., Elson-Schwab, L., Tor, Y. *Ang. Chem. (Int. Ed.)* **2005,** 44, 927-32.